Title
Extending the Limits of Optical Metamaterials

Author
Wong, Zi Jing

Publication Date
2015

Peer reviewed|Thesis/dissertation

Extending the Limits of Optical Metamaterials

By

Zi Jing Wong

A dissertation submitted in partial satisfaction of the

requirements for the degree of

Doctor of Philosophy

in

Engineering – Mechanical Engineering

in the

Graduate Division

of the

University of California, Berkeley

Committee in charge:

Professor Xiang Zhang, Chair
Professor Costas Grigoropoulos
Professor Jie Yao

Summer 2015

Extending the Limits of Optical Metamaterials

by Zi Jing Wong

Abstract

Extending the Limits of Optical Metamaterials

by

Zi Jing Wong

Doctor of Philosophy in Mechanical Engineering

University of California, Berkeley

Professor Xiang Zhang, Chair

For centuries, the ability to control light is bounded by the limited range of materials' refractive index available in nature. This limit is finally broken with the advent of artificially-engineered optical metamaterials. Not only have metamaterials significantly extended the boundaries of refractive index, they have led to many novel properties and applications never thought to be possible. In optics, some of the most fascinating promises of metamaterials include the negative refractive index materials, superlenses and invisibility cloaks. However, optical metamaterials typically suffer enormous loss, which hinders their practical applications. This dissertation not only serves to tackle the optical loss problem, but also offers unique strategies to build practical optical devices with unprecedented functionalities.

The first part of the dissertation shows how the real part of the refractive index can be engineered to cover the entire range from positive to negative. Low-loss bulk three-dimensional optical metamaterials are experimentally demonstrated in both the near-infrared and visible wavelengths, with a maximum transmission exceeding 40%. As metamaterials are typically anisotropic, we can further engineer the components of the permittivity and permeability tensors to attain unique isofrequency contours in the Fourier space. Through rigorous measurement of the transmission and reflection, both amplitude and phase for a range of wavevectors, a novel magnetic hyperbolic dispersion metamaterial is demonstrated, enabling a new path to enhance photon density of states and light-matter interaction. In addition, I will discuss the realization of a zero index metamaterial (ZIM), and its huge potential for nonlinear light generation owing to the uniform phase distribution within the bulk medium. In particular, a phase-mismatch free nonlinear propagation is achieved for the very first time using the ZIM, opening new opportunities for efficient multi-directional nonlinear light generation. The second part of the dissertation details the engineering of the imaginary part of refractive index, taking advantage of the usually undesirable loss, to attain novel device functionalities. The interplay between loss and gain based on the parity-time (PT) symmetry concept can lead to complex conjugate eigenmodes, where the electric fields can be confined either in the gain or loss region at the same (degenerate) frequency. Here I present two novel on-chip PT metamaterial devices: A single-

mode microring laser with unique mode manipulation capability is achieved by careful positioning of the loss and gain nanostructures, where all the unwanted resonant modes are spatially overlapping with the loss regions and hence suppressed. Similarly, by introducing the loss and gain modulation in a straight waveguide configuration, a unique coherent optical amplifier-absorber (COAA) device is demonstrated. Importantly, COAA synergizes both the lasing and anti-lasing (i.e. time-reversed lasing) modes, meaning the device can either amplify or absorb coherent signals at the same frequency depending on the relative input phase, thus potentially approaching the ultimate limit of signal modulation depth in optical communications. The third section of the dissertation presents a subwavelength local phase engineering approach to realize novel optical properties. Using spatially varying plasmonic nanoantennas with strong light confinement to locally modify the phase of the electromagnetic waves, I show how a metasurface optical cloak working in the visible wavelength is carefully designed and built. Unlike previous cloaks, our cloak is ultra-thin and conformal, with the unique ability to restore both the wavefront and phase of the reflected light, rendering a 3D object of arbitrary shape invisible.

To my loving parents and family members

TABLE OF CONTENTS

Acknowledgement

The journey through graduate school is a truly special chapter of my life. There were no doubt plenty of hardships and frustrations, but the exciting and rewarding moments were always there to charge me up. More importantly, it was the kind support from my family, advisors, colleagues and friends that made this dissertation possible.

Firstly, I would like to thank my advisor Prof. Xiang Zhang for his trust in me, an aerospace engineer, to solve some of the most challenging problems in nanophotonics and physics. His broad knowledge, sharp scientific insights and ability to pinpoint the crux of a problem have not only left a huge mark in many of the projects in this dissertation, but also gradually transformed me into a true experimentalist. I always feel blessed to be part of this amazing XLab team that he assembled, where I could easily interact with experts from various fields to discuss ideas and problems, and even engage in heated scientific debate! Prof. Zhang also showed me how to manage multiple projects, write good papers, and communicate efficiently, which are all extremely beneficial for my future scientific career. I also thank Prof. Costas Grigoropoulos, Prof. Liwei Lin, Prof. David Attwood, Prof. Zi Qiang Qiu, and Prof. Jie Yao for serving in either my qualifying exam committee or my dissertation committee.

My sincere gratitude also goes to my XLab comrades! I was first introduced to the metamaterial world by Dr. Boubacar Kante, who is always ready for my questions and discussion, besides instilling the greatest faith in me to excel in research. I also would like to thank Dr. Yuan Wang for his continuous guidance on almost every front: project discussion, paper writing, instrument troubleshoot/repair, etc. No less important are Dr. Haim Suchowski, Dr. Liang Feng, Dr. Ren-Min Ma, Dr. Yu Ye, Dr. Xingjie Ni, Dr. Tongcang Li, Kevin O'Brien, Ye-Long Xu, Jeongmin Kim and Michael Mrejen for the exciting collaboration and endless discussion that we had grinding through different projects. Dr. Junsuk Rho, Dr. Sadao Ota, Dr. Ziliang Ye, Dr. Kar Wei Ng, Dr. Weijian Yang, Dr. Thai Tran, Mervin Zhao, Taiki Hatakeyama and David Barth especially deserve my great appreciation for the many interesting discussion and wonderful friendship over the years.

Finally, I would like to dedicate my greatest thanks to my parents for their unconditional love and support, and to both my brothers who always have my back.

Chapter 1

Introduction

1.1 Permittivity, Permeability and Refractive Index

The control of light is governed by the interaction between the electromagnetic (EM) fields and the optical properties of the matters/materials. Classical electrodynamics is best described using the well-known Maxwell's equations [1],

$$\begin{aligned} \nabla \cdot \boldsymbol{D} &= \rho_f, \quad \nabla \times \boldsymbol{E} = -\frac{\partial \boldsymbol{B}}{\partial t} \\ \nabla \cdot \boldsymbol{B} &= 0, \quad \nabla \times \boldsymbol{H} = \boldsymbol{J}_f + \frac{\partial \boldsymbol{D}}{\partial t} \end{aligned} \tag{1.1}$$

where $\boldsymbol{E}$ is the electric field, $\boldsymbol{H}$ is the magnetic field, $\boldsymbol{D}$ is electric displacement field, $\boldsymbol{B}$ is the magnetic flux density, ρ_f is the free charge density, $\boldsymbol{J}_f$ is the free current density, and t is time. Constitutive relations relate some of the parameters based on the material properties of permittivity ε and permeability μ,

$$\boldsymbol{D} = \varepsilon \boldsymbol{E}, \qquad \boldsymbol{B} = \mu \boldsymbol{H}. \tag{1.2}$$

For a region where there is no free charge and current, Maxwell's equations can be simplified to

$$\begin{aligned} \nabla^2 \boldsymbol{E} &= \mu_0 \varepsilon_0 \frac{\partial^2 \boldsymbol{E}}{dt^2} \\ \nabla^2 \boldsymbol{B} &= \mu_0 \varepsilon_0 \frac{\partial^2 \boldsymbol{B}}{dt^2} \end{aligned} \tag{1.3}$$

where μ_0 and ε_0 are the free space permeability and permittivity, respectively. This is essentially the standard form of a wave equation, elucidating the important fact that light is an electromagnetic wave, and can be described by the general transmission and reflection. One solution to the wave equation is based on the complex wave function

$$\begin{aligned} \boldsymbol{E}(\boldsymbol{r}, \omega, t) &= \boldsymbol{E}_0 e^{i(\boldsymbol{k}\cdot\boldsymbol{r} - \omega t)} \\ \boldsymbol{B}(\boldsymbol{r}, \omega, t) &= \boldsymbol{B}_0 e^{i(\boldsymbol{k}\cdot\boldsymbol{r} - \omega t)} \end{aligned} \tag{1.4}$$

where $\boldsymbol{r}$ is the spatial coordinate and ω is the frequency. $\boldsymbol{k}$ is the wavevector, which governs the wave propagation behavior in terms of both the phase direction and accumulation. One of the simplest forms to describe the wavevector is

$$k = \frac{\omega}{c} n \tag{1.5}$$

where c is the speed of light. Refractive index n is essentially a macroscopic effective material parameter directly linked to the permittivity ε and permeability μ, and is commonly used to describe light refraction and reflection. For conventional materials, we can deduce the refractive index n and impedance Z simply as

$$n = \sqrt{\varepsilon\mu}, \qquad Z = \sqrt{\mu/\varepsilon}. \tag{1.6}$$

The ability to independently design the permittivity ε and the permeability μ of a material is thus extremely important for full control of the electromagnetic wave propagation direction and intensity. Fig. 1.1 shows the EM material parameter space for ε and μ.

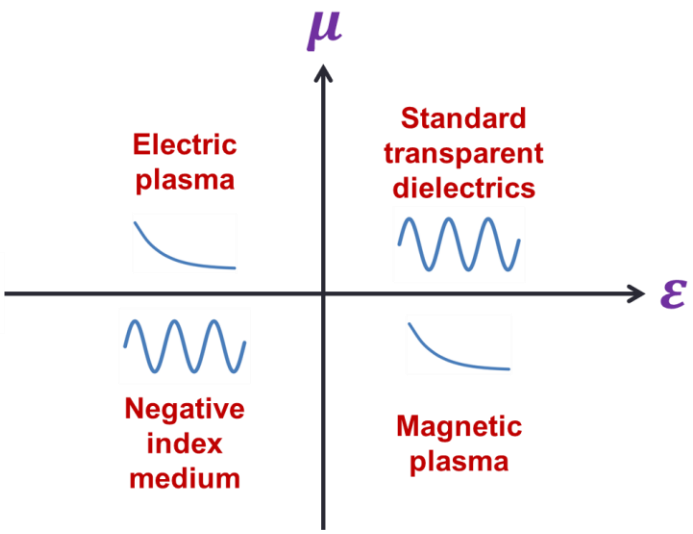

Figure 1.1 Electromagnetic materials categorized by permittivity ε and permeability μ (for real part only). The sinusoidal waveforms represent propagating waves, while the exponential decay waveforms denote evanescent waves.

For most of the dielectric materials, both ε and μ have positive values. From Eqs. (1.6), this directly leads to a real solution of refractive index n, and correspondingly a real wavevector k, as indicated in Eq. (1.5). For a complex wave representation of the electric and magnetic fields (Eqs. (1.4)), a real k means the fields will oscillate in a sinusoidal form, thereby constituting the propagating waves behavior, as illustrated in the top-right region of Fig. 1.1. However, when either one of the ε and μ is negative, the refractive index n will no longer be real, giving rise to an imaginary wavevector k. The former material group is known as electric plasma, which is typical for metals and highly-doped semiconductors; while the latter is called magnetic plasma, much less common in natural materials except for certain ferrites. Eqs. (1.4) indicate that such an imaginary k will cause the electromagnetic fields to evanescently decay in space. This also explains why metals are typically reflective at optical frequencies.

The most intriguing material group falls in the bottom-left region of Fig. 1.1, where both the ε and μ are negative. At first sight, one might naively conclude from Eqs. (1.6) that a positive refractive index n is still preserved. However, a positive square root is already assumed in that equation (which is valid for conventional materials). The more general and rigorous relation between n with ε and μ should be

$$n^2 = \varepsilon\mu. \tag{1.7}$$

To obtain the correct sign convention for n, we can first write out each term in its complex form

$$(n' + in'')^2 = (\varepsilon' + i\varepsilon'')(\mu' + i\mu'') \tag{1.8}$$

and then multiply each term,

$$n'^2 - n''^2 + i(2n'n'') = \varepsilon'\mu' - \varepsilon''\mu'' + i(\varepsilon'\mu'' + \varepsilon''\mu'). \tag{1.9}$$

The positive imaginary part represents the loss, while the negative imaginary part represents the gain. Equating the imaginary terms leads to

$$2n'n'' = \varepsilon'\mu'' + \varepsilon''\mu'. \tag{1.10}$$

For a passive material where no gain is supplied, i.e. $\varepsilon'' > 0$ and $\mu'' > 0$, causality requires that $n'' > 0$. Therefore, for a material with both $\varepsilon' < 0$ and $\mu' < 0$, the only way to satisfy Eq. (1.10) is to have the real part of refractive index

$$n' < 0. \tag{1.11}$$

Therefore, when both the real parts of permittivity ε and permeability μ are negative, a so-called negative refractive index material (NIM) can be obtained. Similar to the case of common transparent dielectrics, NIM results in a real wavevector k, and results in a propagating wave behavior. However, interestingly, the direction of the wavevector (and thus the phase velocity) is now opposite, as first pointed out in the seminal paper by Veselago back in 1968 [2].

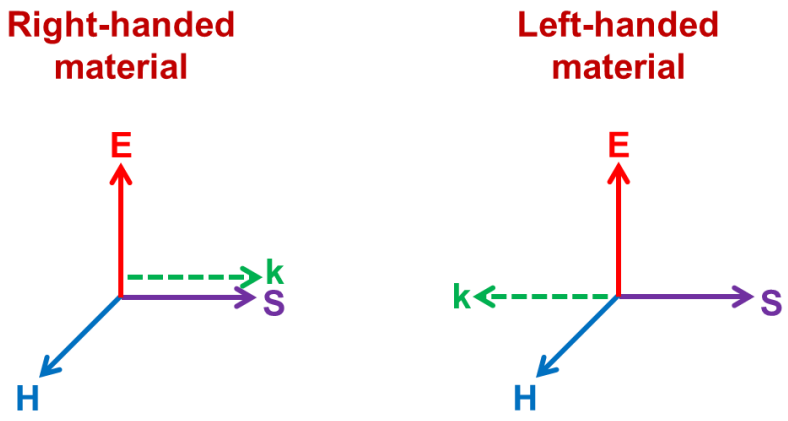

Figure 1.2 Orientation of the electric (E), magnetic (H), phase (k) and Poynting (S) vectors for the right-handed and left-handed materials.

As shown in Fig. 1.2, materials existing in nature are mostly categorized as right-handed materials, where the wavevector $\vec{k}$ is parallel to the Poynting vector $\vec{S}$, which dictates the energy flow direction ($\vec{S} = \vec{E} \times \vec{H}$). On the contrary, NIMs give rise to negative $\vec{k}$ which is antiparallel with the energy propagation (or group velocity) direction. Therefore, NIMs are generally known also as left-handed materials with backward wave/phase propagation. Unfortunately, NIM does not seem to exist in nature, as it entails complex engineering efforts to build. The strategy to construct artificial NIMs is discussed in details in the subsequent section.

From physics point of view, NIMs are extremely unique and interesting. From basic Snell's Law, negative refractive index will directly result in light bending in the 'wrong direction', which opens a new direction of wave propagation control based on negative refraction. The biggest driving force behind the NIM research is no doubt the invention of a superlens that can beat the diffraction limit in imaging. In 2000, Pendry [3] theoretically showed the possibility of using $n = -1$ medium to amplify the evanescent waves to build a superlens that can resolve deep subwavelength information of an imaged object. Till today, such an ideal far-field perfect lens has not been experimentally demonstrated yet, but it has inspired several successful experiments along the line in realizing the so-called 'poor man's superlens' [4,5] and other near-field and far-field imaging systems [6-11] that can surpass the diffraction limit. While the superlens remains the holy grail of NIM research, many remarkable works, either theoretically or experimentally, were carried out to realize the full potentials of NIMs, including invisibility cloaks [12], negative Doppler effects [13], negative Cherenkov radiation [2], reversed Goos-Hänchen shift [14], and trapped rainbow [15].

1.2 Optical Metamaterials

As the control of permittivity ε, permeability μ and refractive index n is extremely critical to manipulate the light propagation, the key question is: can one freely build a material having any combination of ε, μ and n that he/she desires?

In the past, optical elements/devices are mainly made by transparent dielectric materials. While dielectric mediums have the advantage of being almost lossless (i.e. little absorption), their range of ε, μ and n values are quite limited. At optical wavelengths, the permeability μ is always 1, since natural materials cease to have any magnetic response at such high frequencies. Similarly, the permittivity ε is usually rather small for dielectrics in optics, ranging from 1 (air) to 16 (Germanium). Metals allow the access of negative permittivity, but they only occur at frequencies below the fixed plasma frequency, so there's not much room for property tuning and control. In addition, the standard bulk thick metal films are too lossy, and their negative ε values can be too large for certain applications. Not to mention there are only a handful of practical metals available for use in optics. Therefore, the effort to extend the functionality of optical devices based on standard dielectrics is extremely challenging.

In the late 1990s, researchers started to implement a new design strategy relying on the subwavelength structuring of plasmonic materials (i.e. metals or highly-doped semiconductors with negative ε) [16]. The concept of metamaterial is thus born. The word 'metamaterial' literally means beyond conventional materials [17], i.e. the possibility to artificially create a

material which has properties not attainable in nature. Metamaterials are essentially about the artificial engineering of the unit cell property at a scale much smaller than the wavelength of interest, as illustrated in Fig. 1.3. This collective behavior of the unit cells is strong enough to give rise to a macroscopic effective property of the entire medium. In optics, a new mechanism to design and realize exotic EM property is thus possible with the advent of optical metamaterials, where the unit cell is composed of nanostructures much smaller than the optical wavelengths.

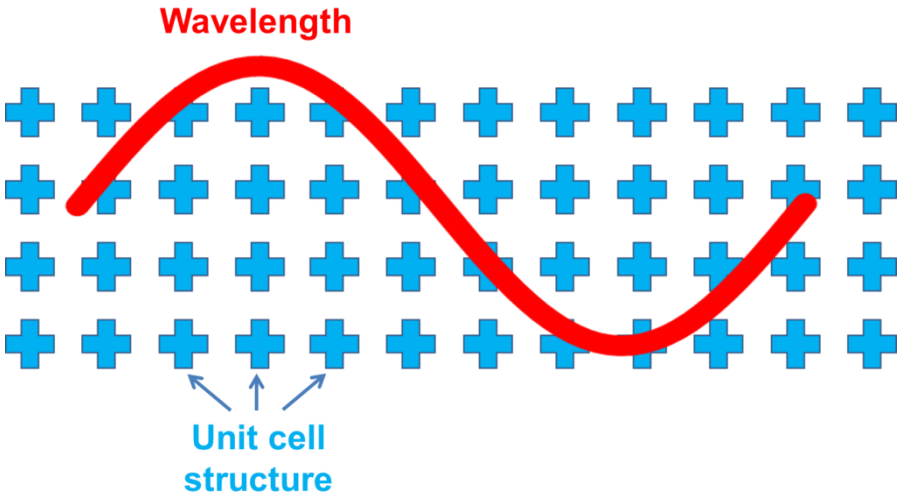

Figure 1.3 Concept of metamaterials: Engineering of the unit cell structure at deep subwavelength scale can lead to macroscopic effective properties not attainable in nature.

The first goal is to arbitrarily control the permittivity ε value. Pendry [18] proposed in 1996 a metallic wire grid structure (Fig. 1.4a) which could easily tune the plasma frequency ω_p, i.e. the frequency where ε crosses the axis from positive to negative, by changing on the period and radius of the wires. The working principle is based on the triggering of self-inductance in the metallic wires, thereby increasing the effective electron mass, which is inversely proportional to the plasma frequency ω_p. Such a structure can be thought of as a diluted metal, where the filling fraction of the metal is reduced, thus providing a broadband negative permittivity background at the frequency range of interest. An alternative way to attain negative ε is via a resonant structure. When a plasmonic material is structured, it can support resonant surface plasmon modes that rearrange the local charge densities and field distributions. A direct consequence to the ε spectrum is a Lorentzian resonance feature, where the real part of permittivity ε' will increase (decrease) significantly right below (above) the plasmonic resonant frequency. When the resonance is strong enough, even a negative ε' value can be attained. Recent work [19] also showed the possibility of achieving extremely large permittivity values (and thus index) using similar principles. However, such resonance-based structures are usually accompanied by an increase in the imaginary part of permittivity ε'' at the resonant frequency, signifying it comes at the expense of loss.

The second aim is to control the permeability μ value at will. This is actually much more challenging, particularly at optical frequencies, as no natural materials are known to exhibit

magnetic response above a terahertz frequency. The constraint is finally broken in year 1999 when Pendry [20] invented a metallic split ring structure to form an alternating current running in a loop corresponding to the incident electromagnetic wave frequency. As illustrated in Fig. 1.4b, by introducing a gap to the otherwise complete ring structure, a strong magnetic resonance can be realized for a plane wave with H-field oriented along the z-direction. This would then significantly enhance the usually weak magnetic moment, even at optical frequencies, and again lead to a Lorentzian feature in the permeability spectrum. The first experimental demonstration of magnetic response at terahertz frequencies is done in 2004 using an oblique incidence on a planar array of SRR structures, where an effective μ from -1 to 4 is obtained at 1 THz [21]. Subsequently, another group fabricated standing SRRs to allow normal incidence excitation (H-field along the normal direction of the SRR) and pushed the magnetic response to the mid-infrared wavelengths [22].

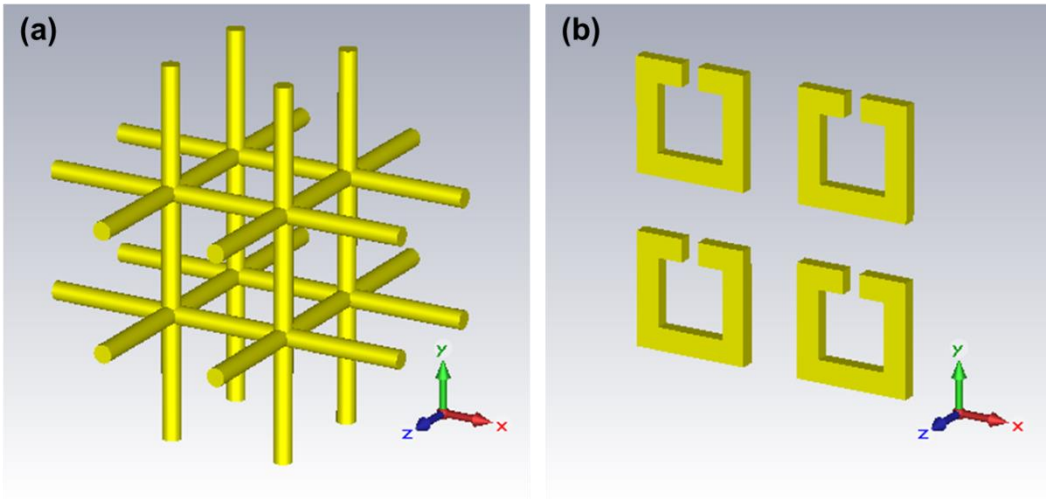

Figure 1.4 (a) Engineering of permittivity ε with metallic wire grid structures. (b) Engineering of permeability μ with split ring resonators.

However, the relatively weak oblique H-field excitation and the tedious fabrication steps of standing SRRs pose quite a challenge to obtaining magnetic response at optical frequencies. Therefore, a slightly different way to excite the magnetic response of a SRR is explored. Instead of exciting with the H-field directly, an E-field polarized along the gap direction (i.e. x-direction in Fig. 1.4b) is used [23] to drive the current loop and hence the magnetic resonance. In analogy, the split ring resonator (SRR) can be modeled as an equivalent LC oscillator circuit in electronics, where the gap is represented by the capacitor, and the metallic ring is similar to an inductor. Therefore it is no surprise that an oscillator resonance can be excited either by having a magnetic field normal to the circuit loop, or by having an electric field across the capacitor plates. Many researchers thus started to fabricate planar SRRs and excite them using normal plane waves. Owing to the simpler structure and easier excitation, magnetic response is realized from mid-infrared wavelengths [24] down to near-infrared wavelengths [25], with the size of SRRs further reduced.

Despite the success in making $\mu \neq 1$ at optical wavelengths, the metamaterial community soon realizes that SRR structure has an intrinsic frequency saturation limit [26-28]. For a realistic

metal, there is always a kinetic inductance L_k term which is inversely proportional to the geometrical scaling factor a. Therefore, the frequency of magnetic resonance ω_m should be written as follows:

$$\omega_m \propto \frac{1}{\sqrt{a^2 + a_k}} \tag{1.12}$$

where a_k is a constant proportional to CL_k (capacitance of the equivalent lumped circuit model is denoted as C). For low frequencies range such as microwaves, $a^2 \gg a_k$ and thus $\omega_m \propto \frac{1}{a}$, so the magnetic resonant frequency continues to scale with the size without any issue. However, at higher frequencies, the a_k term is no longer negligible. This leads to the saturation effect and prevents the magnetic response in the visible wavelengths, as shown also in experiments [28]. A clever approach to bypass this limitation is by using the higher order magnetic resonance of SRRs, where experimentally a magnetic response is observed even at 800 nm [25]. However, the oscillator strength of higher order resonance is typically much weaker, and thus a large change of permeability μ can be challenging.

All these motivate the search of a new structure that can attain a strong magnetic resonance up to the visible wavelengths with negligible saturation effect. Two structures gradually gained popularity: One is the paired metallic nanorods, also known as 'cut-wire pairs' [29,30]. The other is the paired metal stripes, or sometimes called as 'coupled nanostripes' [31,32]. Despite the difference in geometry, these two structures essentially rely on the same principle, differing only in the excitation polarization. As there are two rods/stripes involved, two resonant modes are supported. The first (symmetric) mode has currents flowing in phase in both the rods/stripes and forms an electric dipole moment, hence it is called the electric resonance. The second mode is antisymmetric, where the currents are oscillating out of phase, and the loop-like electric displacement results in a magnetic dipole moment. It is this latter resonance that enables magnetic response in the visible wavelength range. The details of the scaling of such structures can be found in [33], but a more simple way to understand it is through the LC circuit analogy. The paired nanorods/stripes structure is fundamentally similar to a SRR with an extra gap. Therefore, an additional parallel capacitance term should be incorporated, meaning the total capacitance will be reduced, and thus leads to a larger magnetic resonance frequency and saturation limit. The paired nanostripes structure is realized experimentally in 2007 [33], showing strong magnetic resonances across the entire visible spectrum. In addition, these structures are relatively straightforward to fabricate, which is particularly crucial in optics where the wavelength is already very small to begin with. These explain why the paired metallic rods/stripes are heavily used until today to attain not only the magnetic response, but also the negative permeability at optical frequencies.

1.3 Refractive Index Engineering

With the advent of optical metamaterials to control both the permittivity ε and permeability μ, we now have all the necessary tools to engineer the material's refractive index n. Fig. 1.5 shows an example how this is done in optics. A paired silver nanobar structure (200 nm length, 50 nm width, 30 nm gap, 400 nm period) supports two resonant modes, as shown in Fig. 1.5a. The

electric resonant mode occurs at lower wavelength, while the magnetic resonant mode occurs at higher wavelength. Both resonances lead to a dip in transmission, respectively, and the depth and width of each dip depends on its oscillator strength and the associated loss. Using the standard retrieval process [34] based on Fresnel equations, ε and μ can be extracted from the numerically simulated transmission and reflection spectrum (both real and imaginary parts are needed). Both the modes show a Lorentzian feature close to the respective resonance frequency, allowing the access to small (large) ε and μ below (above) the resonant wavelength, including a range of wavelengths with either negative permittivity or negative permeability. Despite its ability to create effective refractive index smaller than air, n' remains positive throughout the wavelength range.

To realize negative refractive index, however, both these resonances should overlap in wavelength, such that $\varepsilon' < 0$ and $\mu' < 0$ together give rise to $n' < 0$, as evidenced in the derivation in Section 1.1. One way to achieve that is by introducing a relative shift [35] to the paired nanobar structure as illustrated in Fig. 1.5b. This shift reverses the coupling of the plasmon hybridization, bringing the electric modes to higher wavelength and the magnetic modes to lower wavelength, as shown by the transmission spectrum. More importantly, due to the stronger nature of the electric resonance, negative permittivity can be attained over a broad range of wavelengths (700-950 nm) below the resonance peak. Therefore, from design point of view, it's much easier to have the modes overlap when the magnetic resonance is engineered to be lower wavelength than the electric resonance. The standard retrieval result displays a small range of wavelengths (740-800 nm) having negative refractive index. Experimental realization of NIMs using such plasmon hybridization coupling control is first realized in microwave frequencies [35,36], and later in the optical regime [37]. It is important to note that an NIM can be obtained even without introducing any relative shift to the paired nanorods, provided that $\varepsilon'\mu'' + \varepsilon''\mu' < 0$ (from Eq. (1.10)) is satisfied. For instance, when ε' is highly negative (or when μ'' is large with a somewhat negative ε'), even a positive μ' with a considerable μ'' value can lead to negative index. Such structures are called single-negative NIMs, in contrast to the double-negative NIMs where both $\varepsilon' < 0$ and $\mu' < 0$ are required. The single-negative NIMs typically exhibit much higher losses n'' with a smaller real part n', yielding a lower figure of merit

$$FOM = -\frac{n'}{n''} \tag{1.13}$$

and a worse impedance matching compare to double-negative NIMs.

A serious drawback of the NIM based on plasmon hybridization coupling is that the electric and magnetic resonances cannot be independently controlled. This reduces the design flexibility and makes the impedance matching harder to attain. A more direct approach is to use the diluted metal principle discussed in Section 1.2, where a periodic array of metallic wires will shift the plasma frequency and provide a broadband background of negative ε' values. A magnetic resonant structure can then be added (or rather squeezed) into each subwavelength unit cell to supply the negative μ'.

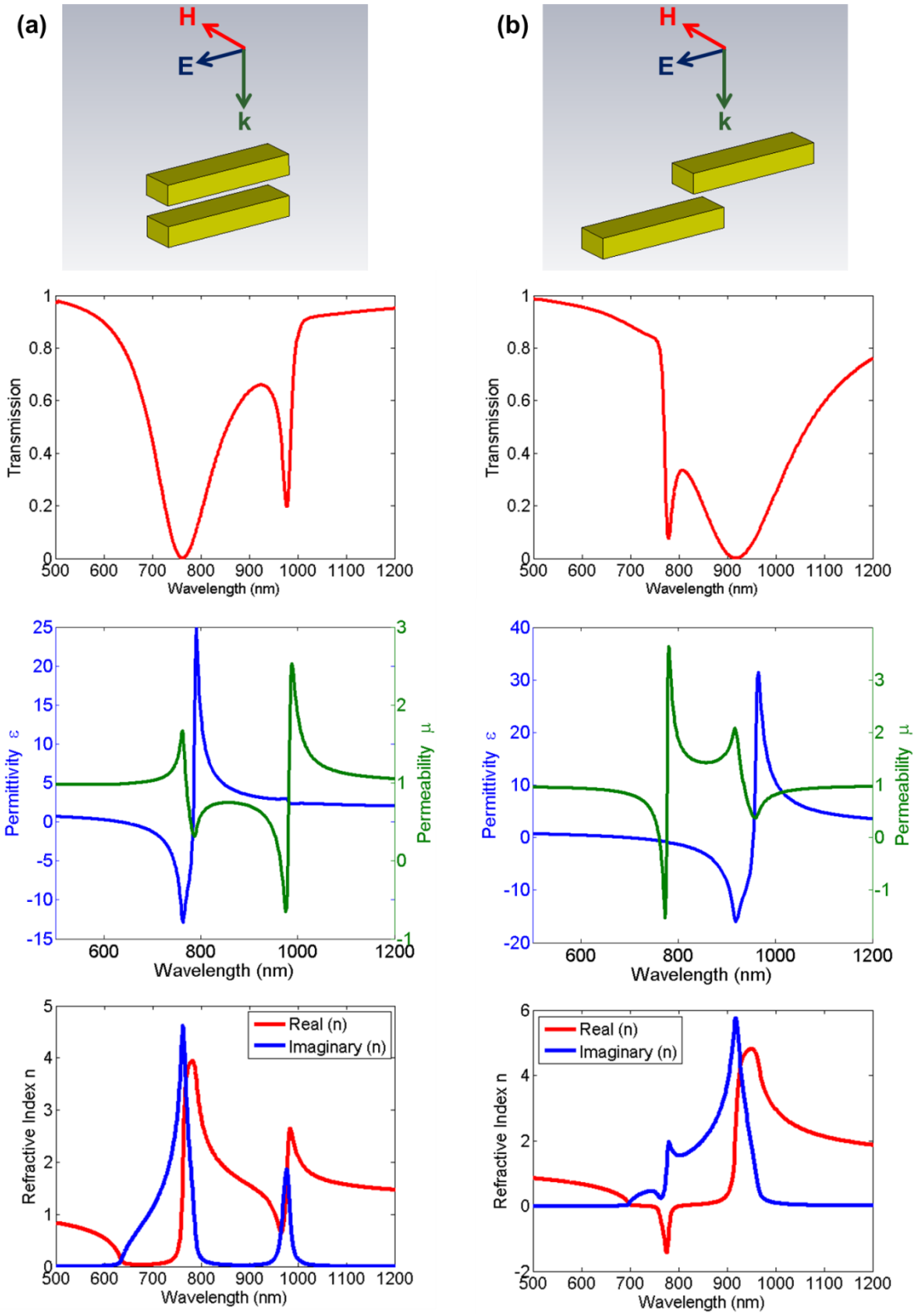

Figure 1.5 (a) Paired nanobar giving distinct electric and magnetic resonances. (b) Shifted paired nanobar reverses the energy of the two resonances, such that negative permittivity and negative permeability can overlap in wavelength, leading to negative refractive index.

In fact, the first experiment on NIM used such a combination of two discrete structures, i.e. periodic metal wires and split ring resonators [38]. A negative refractive index as low as -3 and a negative refraction behavior were successfully measured at the microwave frequency around 10 GHz. However, brute-force inserting two structures within a unit cell is much harder in optics, due to the much smaller period size and the possibility of undesired near-field coupling. In 2006, Zhang [39] demonstrated a novel fishnet structure that brilliantly integrates the non-resonant periodic electric wires and the resonant paired nanorods within a compact unit cell size. While they are electrically connected, these two resonances can be separately excited by the electric and magnetic field correspondingly. Not only that such structure is relatively easier to fabricate, the design of both the electric permittivity background and the antisymmetric magnetic resonance can be more straightforward as well. All these result in NIMs with higher FOM from near-infrared (NIR) wavelengths all the way to the visible wavelengths [40-47]. Until today, the fishnet structure remains the prevalent route to realize NIM in the optical frequency region.

While the pursuit of high FOM optical NIM is extremely exciting and rewarding, we should not limit ourselves to merely engineering the real part of the refractive index to be negative. Many other interesting works based on the metamaterial concept have emerged in recent years. These include epsilon-near-zero (ENZ) materials and zero index metamaterials (ZIMs) where the phase can be uniform throughout the structure [48-50], chiral metamaterials which display extremely large optical activity and circular dichroism [51-53], metamaterial sensors that show high sensitivity due to the plasmonic field confinement [54], metamaterial absorbers exhibiting close to perfect absorption [55,56], plasmon-induced transparency based on the coupling of meta-atoms [57,58], transformation optics devices using spatial refractive index distribution to transform the space [12,59-63], and hyperbolic metamaterials which rely on anisotropic effective parameters to access extremely large *k* vectors and enhance light-matter interaction [6,64-66]. However, most of the works are still related to the engineering of the real part of refractive index.

In Fig. 1.6, I illustrate the big picture of refractive index engineering in optics using the more general complex plane. Standard optical devices, categorized by their functionality, are plotted together for comparison. With the advent of metamaterials, not only that the real part of the refractive index n' can be increased beyond the conventional material limit, but more importantly, it is no longer limited to the positive region. Equally significant is the imaginary part of the refractive index n''. For an amplifier or laser to operate, one needs to engineer the n'' to be negative to supply the gain to compensate the loss. On the contrary, absorbers are artificially built to have a highly positive n'' to maximize the absorption. For efficient transmission of signals in optical circuits, passive waveguides having very small n'' are indispensable. Similarly, for a metamaterial to be useful in practical applications, it is extremely important to demonstrate high transmission (and hence low loss) results. Unfortunately most of the metamaterials to date suffer a significant amount of loss due to the inherent noble metal loss, plus design and fabrication imperfection. Researchers in the field of plasmonics and metamaterials are now actively trying to solve this challenging loss issue. The first approach is on the theory side, for instance by improving the structural design to push the electric field away from the lossy metals [67,68]. The second approach is on the fabrication side, where high quality single-crystal thin film noble metals and low-loss transparent conductive oxides can now be grown [69,70].

In Chapter 2 of this dissertation, I will show how we experimentally attained high transmission (or low-loss) NIM and ZIM, as highlighted in Fig. 1.6. Along the line, I will also demonstrate how a fishnet metamaterial can lead to magnetic hyperbolic dispersion for the first time. The other boundary of metamaterials that can be extended is the nonlinearity. Most of the metamaterials assume a low power excitation, thus all the optical phenomena are predicted within the linear regime. However, due to the possibility of refractive index engineering, metamaterials actually contain rich and unique physics in nonlinear optics. An experiment realizing nonlinear propagation in NIM and ZIM will be shown in Chapter 2 as well.

A careful look at the refractive index map reveals the common design strategy of engineering the index parameter only at a specific region (typically either the gain or the loss). The big question is: Can one realize a new device by engineering the index parameters from two regions simultaneously? More specifically, can a device combining carefully-engineered gain and loss segments attain new unique functionality? This motivates the research on parity-time (PT) metamaterials as will be discussed in more details in Chapter 3 of this dissertation.

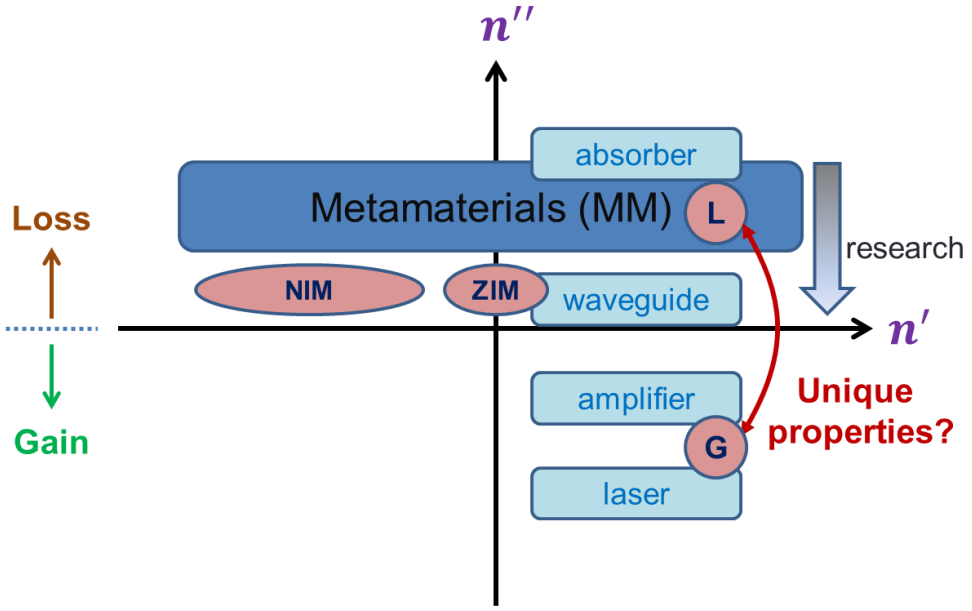

Figure 1.6 The complex refractive index map showing different index parameters which need to be engineered to realize various optical structures and devices.

In 2011, a new field called metasurface is born [71]. Similar to metamaterials, plasmonic nanostructures are used to engineer to electromagnetic properties. However, metasurface only requires a single layer of nanostructures, and they are arranged in a spatial varying configuration (unlike the typical metamaterials which have a periodic unit cell) to engineer the local phase response. In Chapter 4 of this dissertation, I will show how we utilize this phase engineering approach to devise an ultra-thin skin cloak that can hide three-dimensional arbitrarily-shaped objects in the visible wavelength. Finally, I will summarize all the key findings in this dissertation and discuss the future direction of optical metamaterials in Chapter 5.

References

[1] J. D. Jackson, "Classical electrodynamics," Third Edition, John Wiley & Sons, New York (1999).

[2] V. G. Veselago, "The electromagnetics of substances with simultaneously negative ε and μ," *Soviet Physics Uspekhi* **10**, 509 (1968).

[3] J. B. Pendry, "Negative refraction makes a perfect lens," *Physical Review Letters* **85**, 3966 (2000).

[4] N. Fang, H. Lee, C. Sun, and X. Zhang, "Sub-diffraction-limited optical imaging with a silver superlens," *Science* **308**, 534 (2005).

[5] T. Taubner, D. Korobkin, Y. Urzhumov, G. Shvets, and R. Hillenbrand, "Near-field microscopy through a SiC superlens," *Science* **313**, 1595 (2006).

[6] Z. Liu, H. Lee, Y. Xiong, C. Sun, and X. Zhang, "Far-field optical hyperlens magnifying sub-diffraction-limited objects," *Science* **315**, 1686 (2007).

[7] X. Zhang and Z. Liu, "Superlenses to overcome the diffraction limit," *Nature Materials* **7**, 435 (2008).

[8] S. Kawata, Y. Inouye, and P. Verma, "Plasmonics for near-field nano-imaging and superlensing," *Nature Photonics* **3**, 388 (2009).

[9] K. G. Lee, H. W. Kihm, J. E. Kihm, W. J. Choi, H. Kim, C. Ropers, D. J. Park, Y. C. Yoon, S. B. Choi, D. H. Woo, J. Kim, B. Lee, Q. H. Park, C. Lienau, and D. S. Kim, "Vector field microscopic imaging of light," *Nature Photonics* **1**, 53 (2007).

[10] K. Aydin, I. Bulu, and E. Ozbay, "Subwavelength resolution with a negative-index metamaterial superlens," *Applied Physics Letters* **90**, 254102 (2007).

[11] G. Lerosey, J. de Rosny, A. Tourin, and M. Fink, "Focusing beyond the diffraction limit with far-field time reversal," *Science* **315**, 1120 (2007).

[12] D. Schurig, J. J. Mock, B. J. Justice, S. A. Cummer, J. B. Pendry, A. F. Starr, and D. R. Smith, "Metamaterial electromagnetic cloak at microwave frequencies," *Science* **314**, 5801 (2006).

[13] J. Chen, Y. Wang, B. Jia, T. Geng, X. Li, L. Feng, W. Qian, B. Liang, X. Zhang, M. Gu, and S. Zhuang, "Observation of the inverse Doppler effect in negative-index materials at optical frequencies," *Nature Photonics* **5**, 239 (2011).

[14] P. R. Berman, "Goos-Hänchen shift in negatively refractive media," *Physical Review E* **66**, 067603 (2002).

[15] K. L. Tsakmakidis, A. D. Boardman, and O. Hess, "'Trapped rainbow' storate of light in metamaterials," *Nature* **450**, 397 (2007).

[16] S. A. Maier, "Plasmonics: fundamentals and applications," Springer, New York (2007).

[17] W. Cai and V. Shalaev, "Optical metamaterials," Springer, New York (2010).

[18] J. B. Pendry, A. J. Holden, W. J. Stewart, and I. Youngs, "Extremely low frequency plasmoncs in metallic mesostructures," *Physical Review Letters* **76**, 4773 (1996).

[19] M. Choi, S. H. Lee, Y. Kim, S. B. Kang, J. Shin, M. H. Kwak, K.-Y. Kang, Y.-H. Lee, N. Park, and B. Min, "A terahertz metamaterial with unnaturally high refractive index," *Nature* **470**, 369 (2011).

[20] J. B. Pendry, A. J. Holden, D. J. Robbins, and W. J. Stewart, "Magnetism from conductors and enhanced nonlinear phenomena," *IEEE Transactions on Microwave Theory and Techniques* **47**, 2075 (1999).

[21] T. J. Yen, W. J. Padilla, N. Fang, D. C. Vier, D. R. Smith, J. B. Pendry, D. N. Basov, and X. Zhang, "Terahertz magnetic response from artificial materials," *Science* **303**, 1494 (2004).
[22] S. Zhang, W. J. Wan, B. K. Minhas, A. Frauenglass, K. J. Malloy, and S. R. J. Brueck, "Midinfrared resonant magnetic nanostructures exhibiting a negative permeability," *Physical Review Letters* **94**, 037402 (2005).
[23] N. Katsarakis, T. Koschny, M. Kafesaki, E. N. Economou, and C. M. Soukoulis, "Electrical coupling to the magnetic resonance of split ring resonators," *Applied Physics Letters* **84**, 2943 (2004).
[24] S. Linden, C. Enkrich, M. Wegener, J. F. Zhou, T. Koschny,and C. M. Soukoulis, "Magnetic response of metamaterials at 100 terahertz, *Science* **306**, 1351 (2004).
[25] C. Enkrich, M. Wegener, S. Linden, S. Burger, L. Zschiedrich, F. Schmidt, J. F. Zhou, T. Koschny,and C. M. Soukoulis, Magnetic metamaterials at telecommunication and visible frequencies," *Physical Review Letters* **95**, 203901 (2005).
[26] J. Zhou, T. Koschny, M. Kafesaki, E. N. Economou, J. B. Pendry, and C. M. Soukoulis, "Saturation of the magnetic response of split-ring resonators at optical frequencies," *Physical Review Letters* **95**, 223902 (2005).
[27] S. Tretyakov, "On geometrical scaling of split-ring and double-bar resonators at optical frequencies," *Metamaterials* **1**, 40 (2007).
[28] M. W. Klein, C. Enkrich, M. Wegener, C. M. Soukoulis, and S. Linden, "Single-slit split-ring resonators at optical frequencies: limits of size scaling," *Optics Letters* **31**, 1259 (2006).
[29] V. A. Podolskiy, A. K. Sarychev, and V. M. Shalaev, "Plasmon modes in metal nanowires and left-handed materials," *Journal of Nonlinear Optical Physics & Materials* **11**, 65 (2002).
[30] G. Dolling, C. Enkrich, M. Wegener, J. F. Zhou, and C. M. Soukoulis, "Cut-wire pairs and plate pairs as magnetic atoms for optical metamaterials," *Optics Letters* **30**, 3198 (2005).
[31] A. V. Kildishev, W. S. Cai, U. K. Chettiar, J. K. Yuan, A. K. Sarychev, V. P. Drachev, V. M. Shalaev, "Negative refractive index in optics of metal-dielectric composites," *Journal of the Optical Society of America B* **23**, 423 (2006).
[32] G. Shvets and Y. A. Urzhumov, "Negative index meta-materials based on two-dimensional metallic structures," *Journal of Optics A: Pure and Applied Optics* **8**, S122 (2006).
[33] W. S. Cai, U. K. Chettiar, H. K. Yuan, V. C. de Silva, A. V. Kildishev, V. P. Drachev, and V. M. Shalaev, "Metamagnetics with rainbow colors," *Optics Express* **15**, 3333 (2007).
[34] D. R. Smith, S. Schultz, P. Markoš, and C. M. Soukoulis, "Determination of effective permittivity and permeability of metamaterials from reflection and transmission coefficients," *Physical Review B* **65**, 195104 (2002).
[35] B. Kanté, S. N. Burokur, A. Sellier, A. de Lustrac, and J.-M. Lourtioz, "Controlling plasmon hybridization for negative refraction metamaterials," *Physical Review B* **79**, 075121 (2009).
[36] S. N. Burokur, A. Sellier, B. Kanté, and A. de Lustrac, "Symmetry breaking in metallic cut wire pairs metamaterials for negative refractive index," *Applied Physics Letters* **94**, 201111 (2009).
[37] B. Kanté, Y.-S. Park, K. O'Brien, D. Shuldman, N. D. Lanzillotti-Kimura, Z. J. Wong, X. Yin, and X. Zhang, "Symmetry breaking and optical negative index of closed nanorings," *Nature Communications* **3**, 1180 (2012).
[38] R. A. Shelby, D. R. Smith, and S. Schultz, "Experimental verification of a negative index of refraction," *Science* **292**, 77 (2001).

[39] S. Zhang, W. Fan, K. J. Malloy, S. R.J. Brueck, N. C. Panoiu, and R. M. Osgood, "Demonstration of metal–dielectric negative-index metamaterials with improved performance at optical frequencies," *Journal of the Optical Society of America B* **23**, 434 (2006).
[40] G. Dolling, C. Enkrich, M. Wegener, C. M. Soukoulis, and S. Linden, "Low-loss negative-index metamaterial at telecommunication wavelengths," *Optics Letters* **31**, 1800 (2006).
[41] G. Dolling, M. Wegener, C. M. Soukoulis, and S. Linden, "Negative-index metamaterial at 780 nm wavelength," *Optics Letters* **32**, 53 (2007).
[42] G. Dolling, M. Wegener, and S. Linden, "Realization of a three-functional layer negative-index photonic metamaterial," *Optics Letters* **32**, 551 (2007).
[43] U.K. Chettiar, A. V. Kildishev, H. K. Yuan, W. S. Cai, S. M. Xiao, V. P. Drachev, and V. M. Shalaev, "Dual-band negative index metamaterial: double negative at 813 nm and single negative at 772 nm," *Optics Letters* **32**, 1671 (2007).
[44] U. K. Chettiar, S. Xiao, A. V. Kildishev, W. Cai, H. K. Yuan, V. P. Drachev, and V. M. Shalaev, "Optical metamagnetism and negative-index metamaterials," *MRS Bulletin* **33**, 921 (2008).
[45] S. Xiao, U. K. Chettiar, A. V. Kildishev, V. P. Drachev, and V. M. Shalaev, "Yellow-light negative-index metamaterials," *Optics Letters* **34**, 3478 (2009).
[46] J. Valentine, S. Zhang, T. Zentgraf, E. Ulin-Aliva, D. A. Genov, G. Bartal, and X. Zhang, "Three-dimensional optical metamaterial with a negative refractive index," *Nature* **455**, 376 (2008).
[47] C. García-Meca, J. Hurtado, J. Martí, and A. Martínez, "Low-loss multilayered metamaterial exhibiting a negative index of refraction at visible wavelengths," *Physical Review Letters* **106**, 067402 (2011).
[48] M. Silveirinha and N. Engheta, "Tunneling of electromagnetic energy through subwavelength channels and bends using ε-near-zero materials," *Physical Review Letters* **97**, 157403 (2006).
[49] R. Maas, J. Parsons, N. Engheta, and A. Polman, "Experimental realization of an epsilon-near-zero metamaterial at visible wavelengths," *Nature Photonics* **7**, 907 (2013).
[50] H. Suchowski, K. O'Brien, Z. J. Wong, A. Salandrino, X. Yin, and X. Zhang, "Phase mismatch-free nonlinear propagation in optical zero-index materials," *Science* **342**, 1223 (2013).
[51] A. Papakostas, A. Potts, D. M. Bagnall, S. L. Prosvirnin, H. J. Coles, and N. I. Zheludev, "Optical manifestations of planar chirality," *Physical Review Letters* **90**, 107404 (2003).
[52] E. Plum, V. A. Fedotov, and N. I. Zheludev, "Optical activity in extrinsically chiral metamaterial," *Applied Physics Letters* **93**, 191911 (2008).
[53] J. K. Gansel, M. Thiel, M. S. Rill, M. Decker, K. Bade, V. Saile, G. von Freymann, S. Linden, and M. Wegener, "Gold helix photonic metamaterial as broadband circular polarizer," *Science* **325**, 1513 (2009).
[54] T. Chen, S. Li and H. Sun, "Metamaterials application in sensing," Sensors **12**, 2742 (2012).
[55] N. I. Landy, S. Sajuyigbe, J. J. Mock, D. R. Smith, and W. J. Padilla, "Perfect metamaterial absorber," *Physical Review Letters* **100**, 207402 (2008).
[56] N. Liu, M. Mesch, T. Weiss, M. Hentschel, and H. Giessen, "Infrared perfect absorber and its application as plasmonic sensor," *Nano Letters* **10**, 2342 (2010).
[57] S. Zhang, D. A. Genov, Y. Wang, M. Liu, and X. Zhang, "Plasmon-induced transparency in metamaterials," *Physical Review Letters* **101**, 047401 (2008).

[58] N. Liu, L. Langguth, T. Weiss, J. Kästel, M. Fleischhauer, T. Pfau, and H. Giessen, "Plasmonic analogue of electromagnetically induced transparency at the Drude damping limit," *Nature Materials* **8**, 758 (2009).
[59] J. B. Pendry, D. Schurig, and D. R. Smith, "Controlling electromagnetic fields," *Science* **312**, 1780 (2006).
[60] J. Li, and J. B. Pendry, "Hiding under the carpet: A new strategy for cloaking," *Physical Review Letters* **101**, 203901 (2008).
[61] J. Valentine, J. Li, T. Zentgraf, G. Bartal, and X. Zhang, "An optical cloak made of dielectrics," *Nature Materials* **8**, 568 (2009).
[62] L. H. Garielli, J. Cardenas, C. B. Poitras, and M. Lipson, "Silicon nanostructure cloak operating at optical frequencies," *Nature Photonics* **3**, 461 (2009).
[63] T. Zentgraf, Y. Liu, M. H. Mikkelsen, J. Valentine, and X. Zhang, "Plasmonic Lunerberg and Eaton lenses," *Nature Nanotechnology* **6**, 151 (2011).
[64] A. Salandrino and N. Engheta, "Far-field subdiffraction optical microscopy using metamaterial crystals: Theory and simulations," *Physical Review B* **74**, 075103 (2006).
[65] Z. Jacob, L. V. Alekseyev, and E. Narimanov, "Optical hyperlens: Far-field imaging beyond the diffraction limit," *Optics Express* **14**, 8247 (2006).
[66] H. N. S. Krishnamoorthy, Z. Jacob, E. Narimanov, I. Kretzschmar, and V. M. Menon, "Topological transitions in metamaterials," *Science* **336**, 205 (2012).
[67] R. F. Outlon, V. J. Sorger, D. A. Genov, D. F. P. Pile, and X. Zhang, "A hybrid plasmonic waveguide for subwavelength confinement and long-range propagation," *Nature Photonics* **2**, 496 (2008).
[68] R. F. Outlon, V. J. Sorger, T. Zentgraf, R.-M. Ma, C. Gladden, L. Dai, G. Bartal, and X. Zhang, "Plasmon lasers at deep subwavelength scale," *Nature* **461**, 629 (2009).
[69] Y.-J. Lu, J. Kim, H.-Y. Chen, C.Wu, N. Dabidian, C. E. Sanders, C.-Y. Wang, M.-Y. Lu, B.-H. Li, X. Qiu, W.-H. Chang, L.-J. Chen, G. Shvets, C.-K. Shih, and S. Gwo, "Plasmonic nanolaser using epitaxially grown silver film," *Science* **337**, 450 (2012).
[70] P. R. West, S. Ishii, G. V. Naik, N. K. Emani, V. M. Shalaev, and A. Boltasseva, "Searching for better plasmonic materials," *Laser & Photonics Review* **4**, 795 (2010).
[71] N. Yu, P. Genevet, M. A. Kats, F. Aieta, J.-P. Tetienne, F. Capasso, Z. Gaburro, "Light propagation with phase discountinuities: Generalized laws for reflection and refraction," *Science* **334**, 333 (2011).

Chapter 2

Engineering the Real Part of Refractive Index

2.1 Bulk 3D Optical Metamaterials

Refractive index n is a macroscopic effective property conventionally defined for a bulk medium. If the electromagnetic property is changing considerably with the thickness of the material, it is more like a surface property instead. In this case, the standard way of describing refraction and phase advance will no longer be accurate and rigorous. Therefore, making a bulk three-dimensional metamaterials which shows convergence of the refractive index with increasing thickness is extremely essential. In addition, a thick 3D bulk metamaterial allows larger phase accumulation across the material, which is important for many applications. Similarly, in nonlinear optics, there will be more rooms for light propagation and nonlinear frequency mixing to take place with the thick 3D bulk medium, and reduces the contribution from surface nonlinearity.

Despite the strong motivation to realize bulk 3D metamaterials, experimental demonstration of the early optical NIMs and ZIMs are mainly limited to single-layer or few-layer structures [1-6] due to the difficulties in nanofabrication. It is not until 2008 that a clear convergence of the negative refractive index is observed using a multi-layered stacked fishnet structure [7]. Also, in the same work, a bulk fishnet NIM prism was made, showing the negative angle refraction at optical wavelength for the very first time. However, the transmission of the fabricated bulk 3D fishnet is rather low, with a maximum transmittance of only about 15 % at around 1.6 μm. This means that the structure is still rather lossy, thus preventing them from practical applications. To realize the ultimate superlens with resolution beyond the diffraction limit, one key requirement is to first build a 3D bulk isotropic low-loss NIM. While attaining isotropy NIM in optics is still an enormous challenge from both the design and fabrication point of views, the loss problem of optical NIM can potentially be addressed. More importantly, there is an urgent need to extend the operating frequency of the bulk 3D NIM towards the visible wavelength, where many fluorescence dyes and imaging technologies typically work at.

2.2 Bulk 3D NIM & ZIM in the Visible

To demonstrate low-loss bulk 3D optical NIMs and ZIMs, we use a multilayer stacked fishnet structure but with some improvements on the design and fabrication techniques. As previously shown in [7], stacking the fishnet repeatedly can lead to a NIM with potentially lower loss. This is for the antiparallel currents formed at each neighboring layer essentially cancel each other, and thus reduce the absorption loss around the metal regions. Equally important is the coupling of the modes between different layers enables a wide range of frequencies with negative refractive index, thus allowing broadband operation. I will discuss here the design, fabrication and

measurement of a bulk 3D metamaterial that can attain both negative and zero index in the visible wavelength range.

The structural configuration used is shown in Fig. 2.1, with 7 physical layers of silver (Ag, 40nm) and magnesium fluoride (MgF_2, 50nm), with a 15nm capping layer of MgF_2 to help prevent the oxidation of silver. As previously shown [7], three functional layers (i.e. each functional layer corresponds to a three physical layer of metal-dielectric-metal) are already sufficient to attain converged bulk NIM and ZIM properties. Importantly, we choose a 50 nm thin silicon nitride (Si_3N_4) as the substrate (instead of the usual mm thick transparent substrate) for two reasons: 1. Improved fabrication techniques leading to lower optical loss. 2. Remove substrate contribution such that the phase accumulation can be purely negative at negative index wavelength.

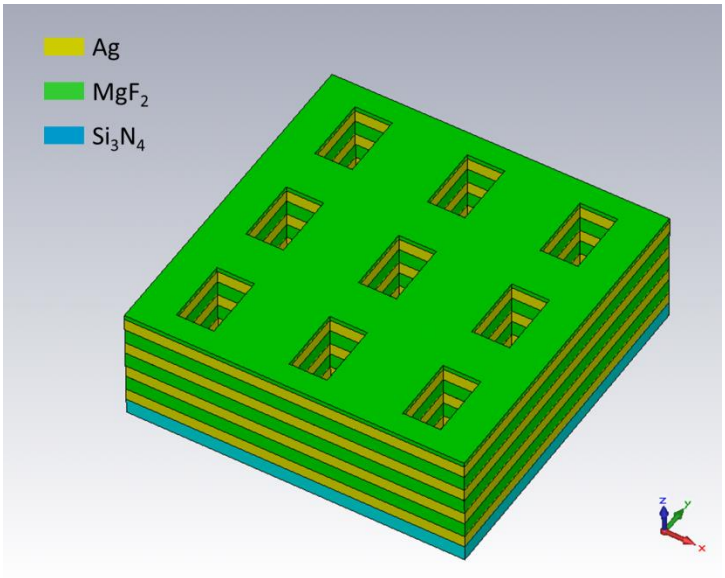

Figure 2.1 Schematic of the silver (Ag)/ magnesium fluoride (MgF2) multilayer fishnet metamaterials with a period of 360 nm, and a hole size of 120 nm × 210 nm. Negative refractive index is obtained via the coupling between the Drude-like negative permittivity background and the multiple magnetic resonances formed between each functional layer of metal/dielectric/metal nanostructures.

The design of the fishnet metamaterials is carried out using a three-dimensional full-wave finite-difference time-domain (FDTD) numerical software, taking into account the dissipative loss of the silver metal used. The polarization is chosen to be E_x (see Fig. 2.1), which allows excitation of the anti-symmetric magnetic resonance whereby negative permeability (thus negative index) can be attained. To illustrate the negative phase delay of the fishnet NIM, we show in Fig. 2.2 the time evolution of the propagating phase fronts inside the bulk metamaterial at 790 nm wavelength, with the cross section taken at the center of the fishnet holes. The color map represents the normalized electric field in the x-direction. *S* and *k* are the Poynting vector and the wave vector, respectively. Unlike conventional positive refractive index metamaterials, the Poynting vector and wave vector are essentially antiparallel inside the NIM, confirming the negative phase accumulation and backward wave propagation behaviors.

One of the biggest challenges to fabricate such a thick multilayer structure is to ensure the sidewall angle of the patterned nanostructures to be small (for better performance). Therefore

selective removal of the nanoholes either using plasma dry etching or focused ion beam (FIB) milling is typically preferred over the electron beam lithography with lift-off technique. As the fishnet structure composed of alternatively stacked silver and magnesium fluoride layers, it's hard to find the right gas that can etch both the metal and dielectric layers, while maintaining a good etching selectivity with the masking layer. On the other hand, FIB milling suffers from undesired ion deposition which increases the absorption loss, particularly at the substrate region beneath the sample. Here we fabricate the fishnet on a thin 50 nm low-stressed Si_3N_4 membrane so that most of the unwanted Gallium ions (Ga^+) can penetrate through the structure and membrane into the free space. This turns out to be extremely crucial in reducing the loss and thus lead to high-transmission NIMs and ZIMs.

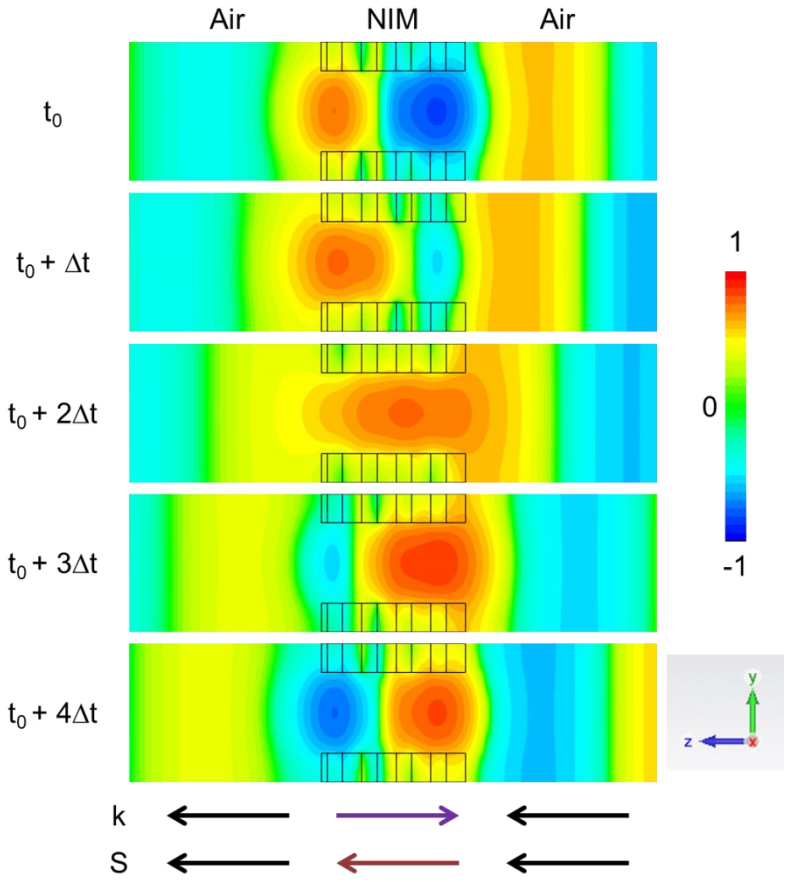

Figure 2.2 Time evolution of the phase front at 790 nm. While the Poynting vector S is always conserved, the wave vector k is shown to be antiparallel inside the negative index metamaterial. Such backward propagating wave behavior is unique for a material with negative refractive index and negative phase accumulation.

The key fabrication steps are illustrated in Fig. 2.3. The fabrication of the fishnet starts with a suspended 50 nm ultra-low-stress silicon nitride (Si_3N_4) membrane made from standard MEMS fabrication technologies. The metal-dielectric stack is then deposited onto the Si_3N_4 membrane using layer-by-layer electron beam evaporation technique at pressure ~1×10^{-6} Torr. Next, the sample is turned upside down and mounted on a special stage holder which has a matching trench at the center. The nanostructures are milled by using FIB from the membrane side. This is

essential not just for alignment purpose, but also to reduce the optical loss caused by Ga ion penetration into the metal layers.

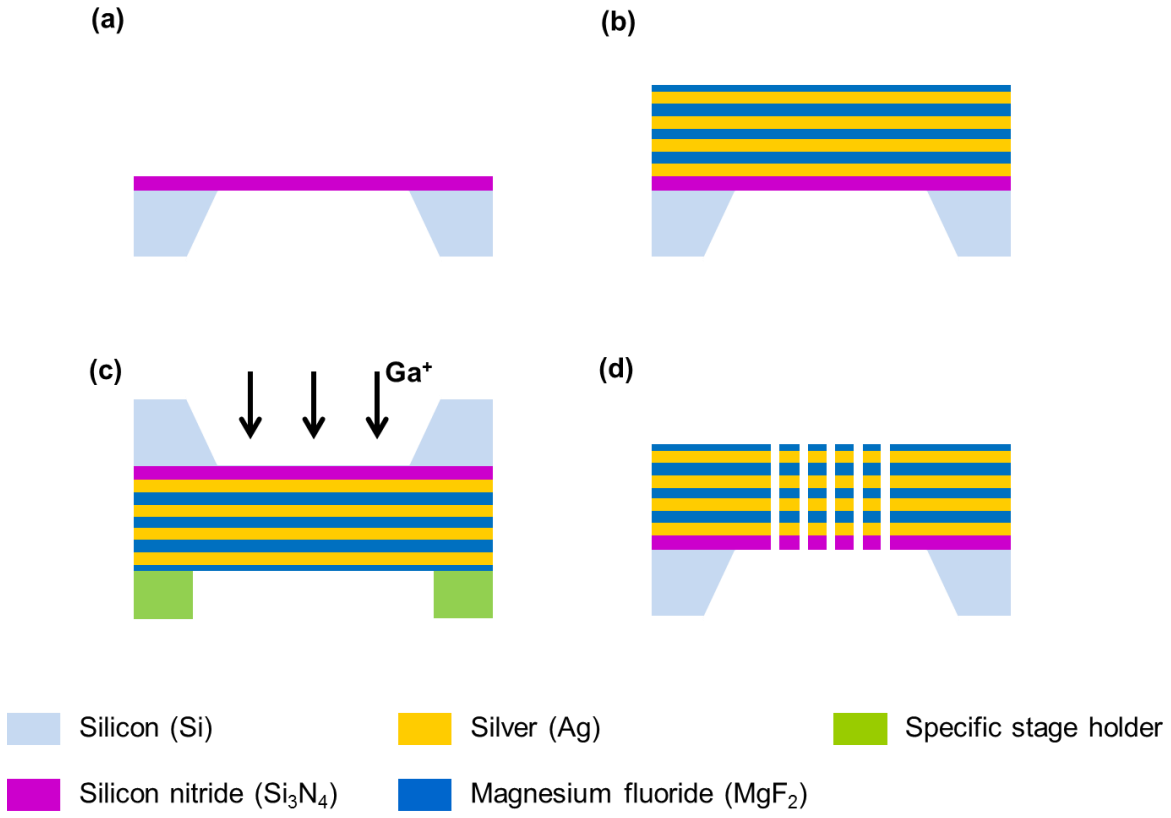

Figure 2.3 Schematic of the key steps in sample fabrication. (a) Fabrication of an ultra-low-stress Si_3N_4 suspended membrane. (b) Multilayer electron beam evaporation of Ag and MgF_2 layers without vacuum break. (c) Flip side mounting of sample followed by Ga^+ focused ion beam milling to pattern the nanostructures. (d) Final fishnet structure formed.

To verify the low-loss behavior of the fabricated suspended fishnet, transmission measurement is first performed. As shown in Fig. 2.4, several transmission peaks are observed. This multiple resonance feature arises due to the stacking of the metal/dielectric/metal layers, which lead to a low-loss broadband transmission feature at the desired wavelength range. Also shown is the numerical simulation result which matches well with the experimental data. In particular, the experimental transmission at 740 nm is measured to be 30%, which is among the highest reported in the visible wavelengths for bulk NIM.

For more rigorous determination of the bulk refractive index, phase measurement is needed. To measure the transmission phase change induced by the fishnet metamaterial across a broad frequency range, we built a spectrally and spatially resolved Mach-Zehnder interferometry setup similar to [8]. As illustrated in Fig. 2.5, essentially a broadband light source is split into two paths, one passing through the sample while the other serves as a reference beam, before recombining them at the input of an imaging spectrometer. The two beams interfere at different angles to produce interference fringes along the vertical axis of the imaging camera. A change in the optical path length of one of the beams will therefore cause the interference fringe to shift vertically on the image plane. By measuring the interferogram with and without the sample, and

comparing them using Fourier analysis, the metamaterial induced phase change can therefore be obtained. Importantly, the phase change at different wavelengths can be captured simultaneously along the horizontal axis of the camera in a single-shot measurement.

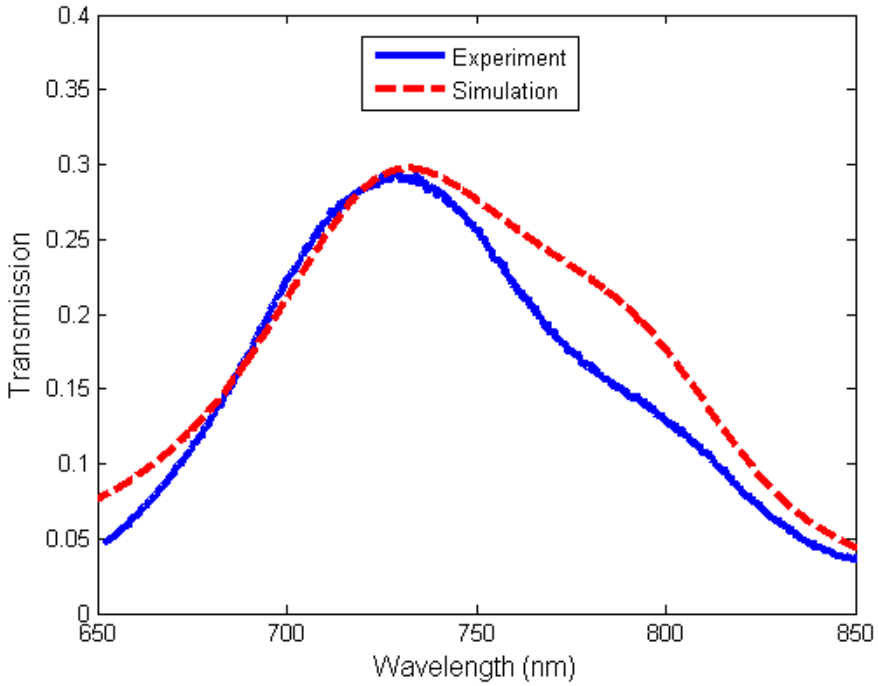

Figure 2.4 Transmission of the fishnet metamaterial. Both the measured and simulated results show a broad spectrum with relatively high transmission. Maximum transmission of 30% is observed at ~740 nm, while 15% transmission is measured at the desired 790 nm wavelength.

To extract the material's effective refractive index, we simulate the transmission and reflection (both amplitude and phase) of the designed fishnet metamaterial and then reconstruct the refractive index by using the Fresnel equation. We aim for the index zero-crossing at 750 nm, above which the index will become negative. Fig. 2.6 shows the simulated refractive index from 650 nm to 850 nm wavelength range, essentially a smooth transition from positive to negative index. Experimentally, using the phase shift values measured by the setup in Fig. 2.5, with the standard assumption of negligible multiple reflections within the structure, we can further extract its refractive index values across a broad frequency range, as depicted by the blue line in Fig. 2.6. The trend basically agrees with the simulated results, with the slight discrepancy most likely due to the small sidewall angle of the actual fishnet structures and other fabrication-induced errors. A broadband negative index property is thus obtained from 750 nm up to 850 nm.

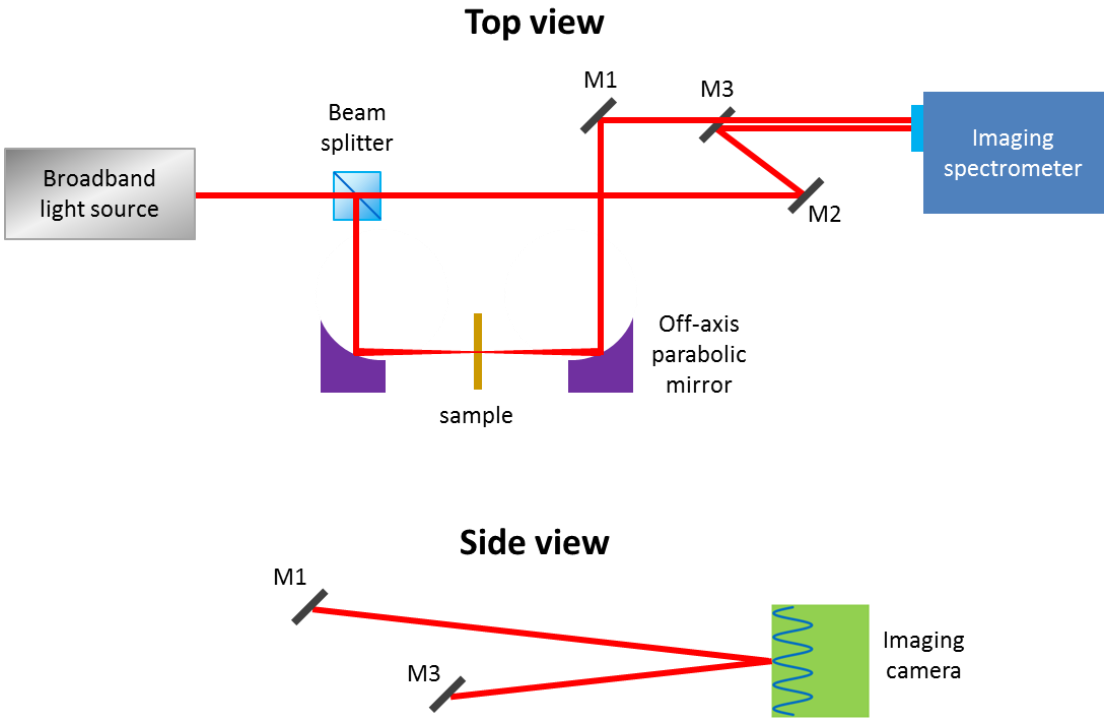

Figure 2.5 Phase measurement setup. Interference between a beam transmitted through the sample and a reference beam allow the fringes to be formed at the imaging camera. By comparing the interferogram measured with and without the sample, the phase shift induced by the metamaterial can be determined simultaneously across a broad spectrum, limited only by the operational wavelength range of the broadband light source and the detector sensitivity.

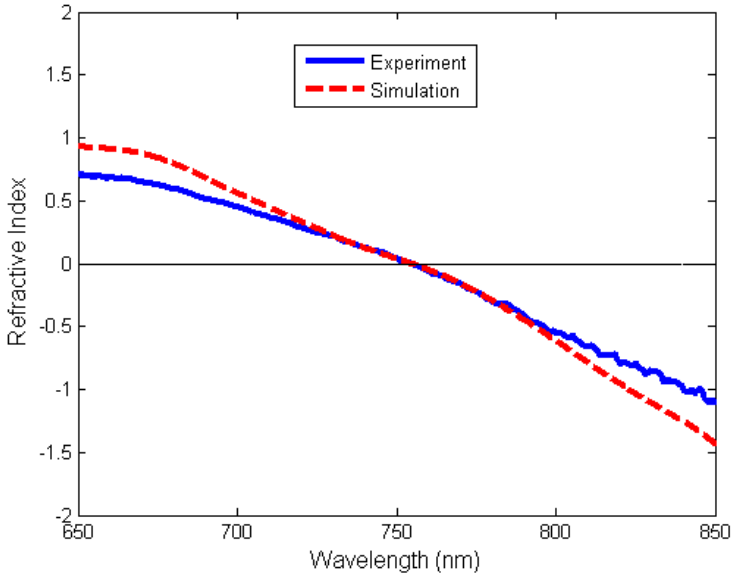

Figure 2.6 Refractive index of the bulk fishnet metamaterial. Both the measured and simulated refractive index values show a gradual transition from positive to negative index, with zero-crossing at around 750 nm wavelength.

2.3 Magnetic Hyperbolic Bulk 3D Optical Metamaterials

As most optical metamaterials realized to date are based on the engineering of resonances at different polarizations, it is essential to treat them as anisotropic materials and effectively describe them based on electric permittivity tensor $\hat{\varepsilon}$ and magnetic permeability tensor $\hat{\mu}$ as follows.

$$\hat{\varepsilon} = \begin{pmatrix} \varepsilon_x & 0 & 0 \\ 0 & \varepsilon_y & 0 \\ 0 & 0 & \varepsilon_z \end{pmatrix}; \qquad \hat{\mu} = \begin{pmatrix} \mu_x & 0 & 0 \\ 0 & \mu_y & 0 \\ 0 & 0 & \mu_z \end{pmatrix}. \tag{2.1}$$

In 2003, Smith and Schurig [9] first proposed a new class of indefinite material for strongly anisotropic media where the principal components of the electric permittivity tensor $\hat{\varepsilon}$ and/or magnetic permeability tensor $\hat{\mu}$ have opposite signs. Without loss of generality, we consider the case where electric field is polarized along x-direction for TE wave, and magnetic field is polarized along y-direction for TM-wave. The dispersion relations can then be simplified to

$$\begin{aligned} (TE) \qquad & \frac{k_y^2}{\varepsilon_x \mu_z} + \frac{k_z^2}{\varepsilon_x \mu_y} = \frac{\omega^2}{c^2} \\ (TM) \qquad & \frac{k_x^2}{\varepsilon_z \mu_y} + \frac{k_z^2}{\varepsilon_x \mu_y} = \frac{\omega^2}{c^2} \end{aligned} \tag{2.2}$$

From these equations, different types of isofrequency contours can be obtained depending on the relative signs of the components of $\hat{\varepsilon}$ and $\hat{\mu}$ tensors. When all of them are of the same sign, either an elliptic or a circular isofrequency contour is attained. In contrast, when either $\hat{\varepsilon}$ or $\hat{\mu}$ tensors have diagonal components of opposite signs, this will lead to hyperbolic isofrequency contour. The former case is known as electric hyperbolic dispersion (for TM-ploarization), while the latter is called magnetic hyperbolic dispersion (for TE-polarization) [10].

Interestingly, materials with hyperbolic dispersion can support propagating electromagnetic waves with extremely large wavevectors and exhibit very unique optical properties. These include beating the diffraction limit in imaging [9,11,12], enabling negative refraction [9,11,12], and realizing extremely large photon density of states which can enhance light matter interaction [9,11,12]. However the hyperbolic dispersion in all artificial [13-18] and natural [19-22] optical structures studied to date originates solely from their electric response. This fundamentally restricts the performance of these materials to only one polarization of light [23] and inhibits impedance matching with free space [24]. Such restrictions can be overcome in media having components of opposite signs in both electric and magnetic tensors [9].

Therefore, the ability to control both the electric permittivity and the magnetic permeability allows dispersion engineering for any arbitrary polarization and non-polarized light. This is of major importance for the efficient interaction with randomly positioned emitters or thermal radiation. Moreover, the control over both electric and magnetic responses allows one to engineer the dispersion and the impedance independently, and thus enables impedance matching between the hyperbolic material and free space. Impedance matching prevents any light

reflections at the interfaces and allows for efficient light coupling and extraction from the hyperbolic materials. Therefore, it is particularly interesting to experimentally realize a magnetic hyperbolic material with the effective magnetic permeability tensor having principal components of opposite signs [9,25]. Such development would open new opportunities for super-resolution imaging, nanoscale optical cavities or control over the density of photon states and, in particular, the magnetic density of states for enhancing the brightness of magnetic emitters [26,27].

As bulk fishnet metamaterials allow experimental access to negative permeability for a specific polarization, they are good candidates for realizing magnetic hyperbolic dispersion in optics [10,28]. However, a direct and rigorous measurement of such dispersion remains out of reach. Using the fabrication technique described in Section 2.2, we fabricated a bulk fishnet structure using 20 alternating layers of gold (Au) and magnesium fluoride (MgF_2) on a 50 nm thin silicon nitride (Si_3N_4) membrane, as shown in Fig. 2.7. As we are aiming to operate at near infrared wavelengths, the metallic loss is actually smaller (than in visible wavelengths), thus our fishnet can attain an even larger optical transmission up to 42% at ~1320 nm wavelength, as shown in Fig. 2.7b. We also measure the fishnet refractive index at normal incidence by using the spectrally and spatially resolved interferometry previously discussed (Fig. 2.5). The measured refractive index is shown in Fig. 1c, where negative index is observed from 1410 nm to 1700 nm.

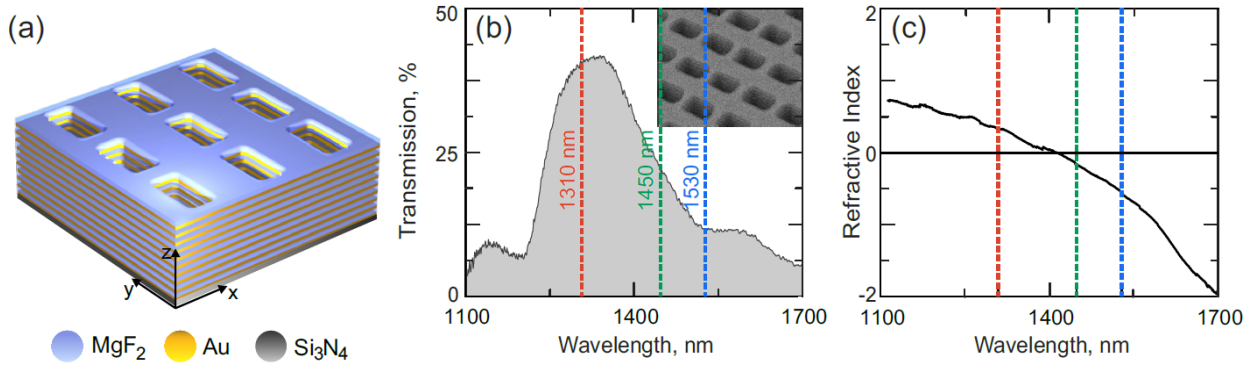

Figure 2.7 (a) Illustration of the 20-physical-layer fishnet metamaterial. Thicknesses of Au, MgF_2 and Si_3N_4 layers are 30 nm, 45 nm and 50 nm, respectively, with a period of 750 nm in both x- and y-directions. The hole size is 260×530 nm. (b) Measured transmission spectrum of the fishnet metamaterial. Inset shows the SEM image of the fabricated structure. (c) Effective refractive index of the fishnet metamaterial extracted at normal incidence. The dotted lines in (b) and (c) represent the wavelengths in the positive index regime (red), near zero index regime (green), and negative index regime (blue).

To obtain the dispersion isofrequency contours experimentally, we have to collect the light for a range of incidence angles. Both the amplitude and phase of the transmitted and reflected lights are measured. The normal component of k-vector k_z is reconstructed via the Fresnel equations [29], while the tangential components of k-vector k_x and k_y have to be continuous at the interface. For the phase measurements, we built a Mach-Zehnder interferometer [30] for the transmitted signals, and we used a Michelson-Morley interferometer [30] for the reflected signals, as illustrated in Fig. 2.8. To resolve transmission and reflection at different angles, we focus and collect the light using an objective lens with high numerical aperture and project the objective's back-focal plane image onto an infrared camera. The resulting image on a camera represents the k-space spectrum of the fishnet metamaterial with the center of the image corresponding to the k-

vectors normal to the sample, and the edge of the image corresponds to the k-vectors oblique to the fishnet at an angle ~58^{o}, limited by the numerical aperture (NA) of the objective. However, for the transmission measurements the NA is limited to 0.7 by the finite size of the silicon nitride membrane window etched in a bulk supporting silicon wafer. This also allows us to neglect any non-paraxial effects due to sharp focusing. We recombine the back-focal plane image with a reference beam to form the interference pattern, with which the phase information is reconstructed using an off-axis digital holography technique [31].

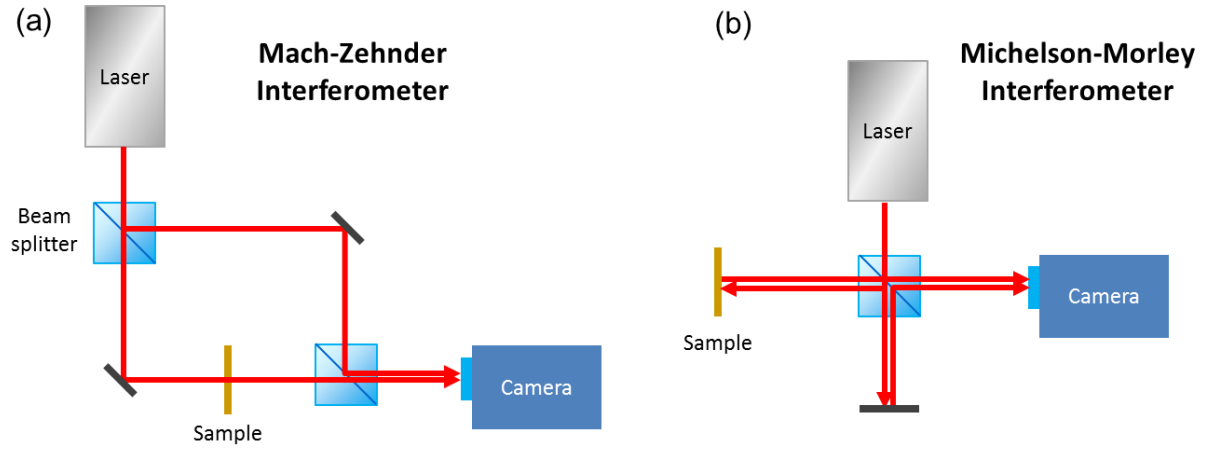

Figure 2.8 (a) Mach-Zehnder Interferometer for transmission mode phase measurement (b) Michelson-Morley Interferometer for reflection mode phase measurement

Three different wavelengths are selected for the complex transmission and reflection measurements, i.e. 1310 nm, 1450 nm, and 1530 nm. They represent the positive index regime, near-zero index regime, and negative index regime, respectively, as highlighted by the red, green, and blue lines in Fig. 2.7b and 2.7c. A linearly polarized light with electric field pointing in x-direction is used as the probing light source. After the objective lens the focused beam has TE-polarization along the k_y-axis and TM-polarization along the k_x-axis. Therefore, by collecting the back-focal plane images (Fig. 2.9), we can measure the magnetic dispersion behavior along the k_y-axis, and the electric dispersion behavior along the k_x-axis.

The interpretation of the transmitted phase results is particularly essential. At 1310 nm (Fig. 2.9g), the phase accumulation increases from the center (normal incidence) to edges (60◦ oblique incidence), similar to the response of a usual dielectric where phase accumulation increases with increased optical path inside the medium. At 1450 nm (Fig. 2.9h), the phase accumulation along the k_y-axis remains small and nearly unchanged for the entire range of incident angles, which is predicted for epsilon-near-zero (ENZ) [32] and mue-near-zero (MNZ) [33] materials. At 1530 nm (Fig. 2.9i), the phase accumulation is decreasing from center to edges along the k_y-axis, while it is increasing along the k_x-axis.

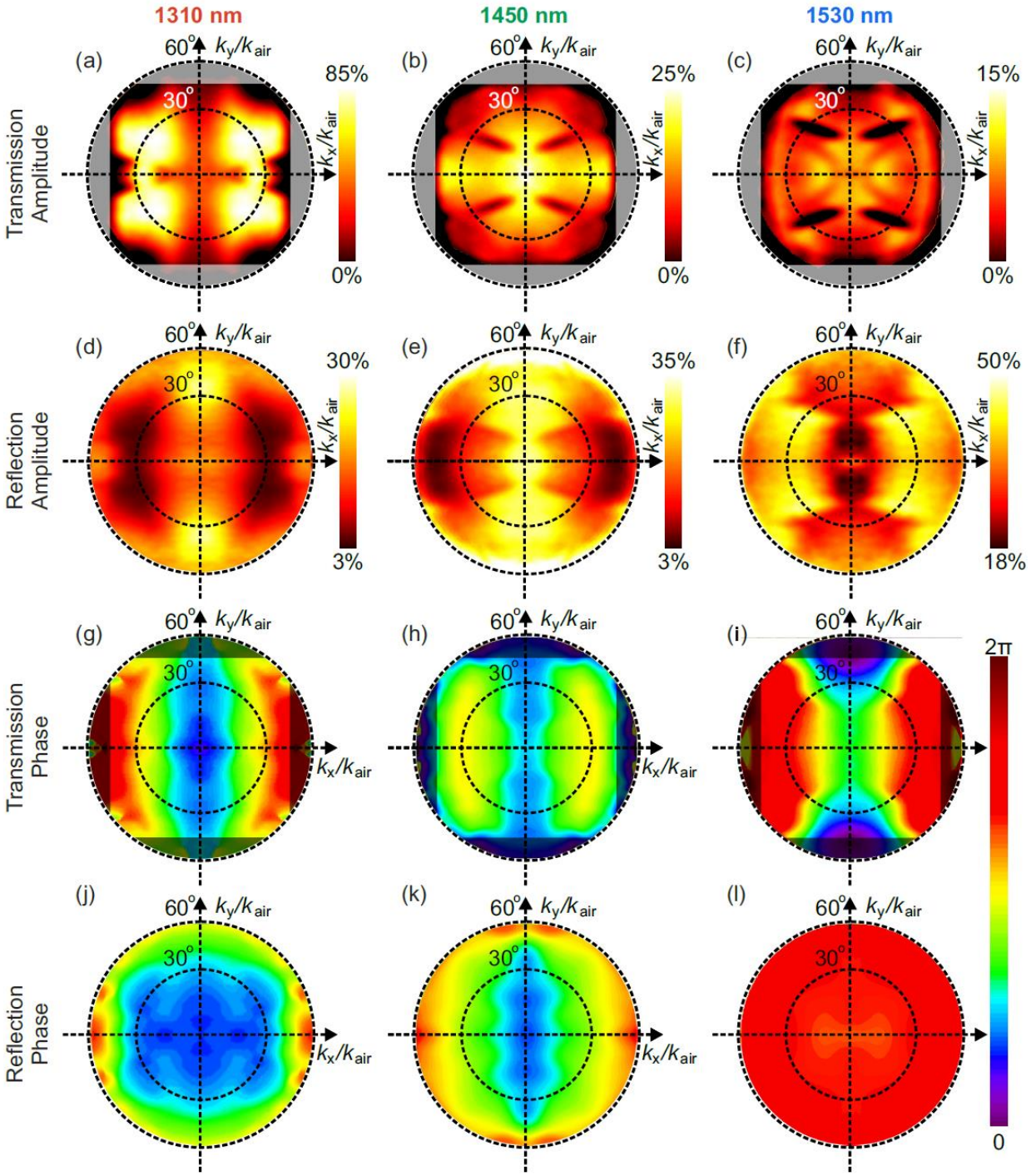

Figure 2.9 Measured (a-c) transmission and (d-f) reflection amplitudes, (g-i) transmission and (j-l) reflection phase for three different wavelengths: (a,d,g,j) 1310 nm, (b,e,h,k) 1450 nm, and (c,f,i,l) 1530 nm. The measurements are performed from incident angles of 0^o up to 60^o. Horizontal axes correspond to TM-polarized illumination, while vertical axes correspond to TE-polarized illumination. Square apertures for the transmission amplitude and phase measurements show the numerical aperture limited by the size of the windows in the supporting silicon wafer.

For the amplitude measurement, it is interesting that very low reflection <4% (lower than glass-air interface) is observed for certain incident angles at 1310 nm (Fig. 2.9d) and 1450 nm wavelengths (Fig. 2.9e). This low reflection is one of the manifestations of the magnetic response of the metamaterial, which together with its electric response allows one to achieve excellent impedance matching between the metamaterial and air. More importantly, using this complex transmission and reflection data in the k-space, we can then reconstruct the isofrequency contours for both the polarizations at the three measured wavelengths, as depicted in Fig. 2.10.

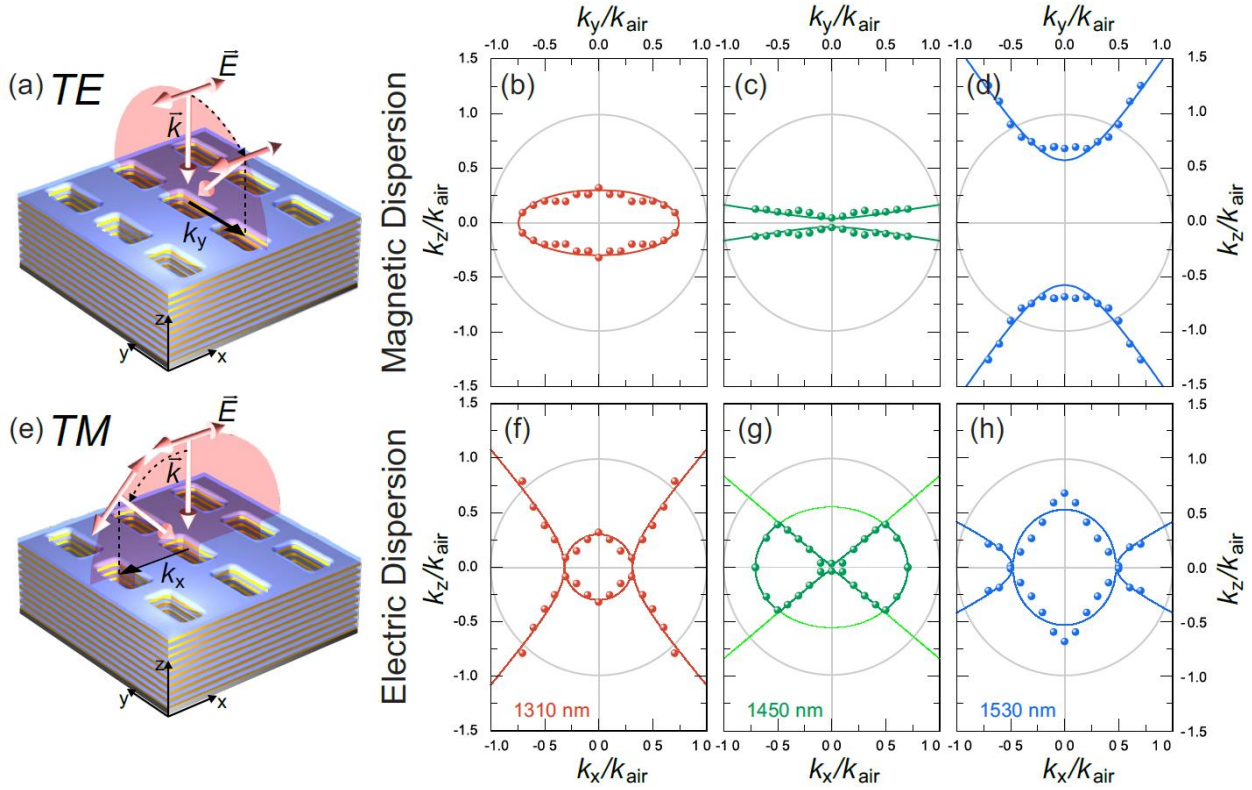

Figure 2.10 (a) Sketch of the TE-polarized illumination. (b-d) Isofrequency dispersion contours for TE-polarization at wavelengths 1310 nm, 1450 nm, and 1530 nm, respectively. (e) Sketch of the TM-polarized illumination. (f-h) Isofrequency dispersion contours for TM-polarization at wavelengths 1310 nm, 1450 nm, and 1530 nm, respectively. Dots mark the experimental data, while lines correspond to analytical results. Grey circles correspond to an isofrequency contour of light in air.

For TE-polarization at 1310 nm wavelength, the isofrequency contour is elliptical (Fig. 2.10b), and it lies within the circular contour of light in air. This is no doubt the standard dielectric case where both the components of magnetic permeability tensor μ_y and μ_z are positive. At 1450 nm for TE-polarization, we observe an extreme case of the material dispersion (Fig. 2.10c). In this regime, both the permittivity component ε_x and permeability component μ_y approach zero, resulting in an increase of the phase velocity of light towards infinity inside the bulk metamaterial, and the k_z component remains close to zero regardless of the k_y component. This extreme regime, where the isofrequency contours collapse into a straight line is also known as optical topological transition [12] between the closed elliptic contours on the short-wavelength side of the spectrum and open hyperbolic contours on the long-wavelength side. More interestingly, at 1530 nm wavelength, the TE-wave isofrequency contour becomes hyperbolic

(Fig. 2.10d) due to the opposite signs of the components of the magnetic permeability tensor, where μ_y component becomes negative, while μ_z component remains positive. As this hyperbolic dispersion is a result of effective magnetic response, this essentially constitutes the first experimental realization of magnetic hyperbolic dispersion in a bulk 3D optical metamaterial. Importantly, the branches of the hyperbola exceed the radius of the circular isofrequency contour of light in air, meaning our structure supports propagating waves with k-vectors larger that the k-vectors in air, thus it holds the potential for super-resolution imaging, nano-scale optical cavities and extremely large photon density of states.

To extract the anisotropic components of the permittivity and permeability, we developed an analytical theory of nonlocal material response to match the experimental data, as fishnet metamaterials are known to exhibit spatial dispersion [10]. This more generalized dispersion relation can be written as follows,

$$(TE) \qquad \frac{k_y^2}{\varepsilon_x} + \frac{k_z^2}{\varepsilon_x\left(1-\frac{\partial^2\varepsilon_x}{\partial k_z^2}\right)^{-1}} = \frac{\omega^2}{c^2} \qquad \mu_y = \left(1-\frac{\partial^2\varepsilon_x}{\partial k_z^2}\right)^{-1}$$

$$(TM) \qquad \frac{k_x^2}{\varepsilon_z + \frac{\partial^2\varepsilon_z}{\partial k_x^2}k_x^2 + \frac{\partial^2\varepsilon_z}{\partial k_z^2}k_z^2} + \frac{k_z^2}{\varepsilon_x + \frac{\partial^2\varepsilon_x}{\partial k_x^2}k_x^2 + \frac{\partial^2\varepsilon_x}{\partial k_z^2}k_z^2} = \frac{\omega^2}{c^2} \tag{2.3}$$

In addition, we also employ the Maxwell-Garnett approximation to calculate the effective permittivity of the fishnet in z-direction using realistic material parameters of gold, magnesium fluoride and silicon nitride [34-37]. The calculated ε_z component is close to 2.6 for all three measured wavelengths. For the bulk fishnet metamaterial, $\mu_z = 1$ for all three wavelengths as the structure is not magnetically polarizable in the z-direction. Thus, for TE-polarization we use two independent parameters ε_x and μ_y to match the analytical results with the experimental data. For TM-polarization three independent parameters are used: ($\frac{\partial^2\varepsilon_x}{\partial k_x^2}$, $\frac{\partial^2\varepsilon_z}{\partial k_x^2}$, $\frac{\partial^2\varepsilon_z}{\partial k_z^2}$), while two more parameters are transferred from the TE case and one parameter is calculated via the Maxwell-Garnett approximation. The retrieved parameters are summarized in Table 2.1.

Table 2.1 Retrieved effective parameters of the fishnet metamaterial

Parameter	1310 nm (positive-index)	1450 nm (near-zero-index)	1530 nm (negative-index)
ε_x	0.55	-0.05	-0.14
μ_y	0.16	-0.018	-2
$\frac{\partial^2\varepsilon_x}{\partial k_x^2}$	-5	-41	0.63
$\frac{\partial^2\varepsilon_z}{\partial k_x^2}$	-25	-4.2	-10
$\frac{\partial^2\varepsilon_z}{\partial k_z^2}$	20	-8.5	50

For TM-polarization, the isofrequency contours are more complicated in shape. This is due to the spatial dispersion effect, where the electric field has two components with respect to the principal axes of the metamaterial, namely E_x and E_z. As a result, a large number of quadrupole susceptibility terms significantly influence the dispersion. However, they can still be well-described by the analytical theory. Interestingly, certain k-vectors at 1310 nm wavelength are still larger than the circular isofrequency contour of air, therefore even at TM-polarization the metamaterial possesses optical properties that are distinctive for hyperbolic media, eg. high photon density of states. From geometrical perspective, the dispersion for the TM-polarization is described by fourth-order curves. This suggests that a wide range of nontrivial isofrequency dispersion contours can potentially be realized by proper tuning of the spatial dispersion [38].

In summary, we experimentally realized the first magnetic hyperbolic dispersion in three-dimensional metamaterials with principal components of the effective magnetic permeability tensor having opposite signs. The measurement techniques used here mark the most rigorous way to retrieve the effective parameters, as both the amplitude and phase of the transmitted and reflected lights are measured for different incident k-vectors. A clear topological transition from the elliptic isofrequency contour to hyperbolic dispersion is observed. Our magnetic hyperbolic metamaterial also allows the access of k-vectors larger than air, retaining the advantage of typical electrical hyperbolic media. Using an analytical theory of spatial dispersion, we have shown that, while magnetic dispersion of the metamaterial is fully described by the local permittivity and permeability tensors, the electric dispersion is largely shaped by nonlocal contributions [39]. Spatial nonlocalities therefore open-up new opportunities for extreme engineering of the materials' isofrequency contours beyond elliptic or hyperbolic shape, with non-trivial geometry and topology. Our results not only shows the possibility to engineer efficient hyperbolic media for unpolarized lights, but also paves the way for other three-dimensional magnetic hyperbolic metamaterials assembled from magnetically polarizable or chiral elements [40-42].

2.4 Nonlinear Propagation in Bulk 3D Optical Metamaterials

The metamaterials discussed thus far mainly operate within the linear regime, i.e. the output intensity is directly proportional to the input light intensity. However, with the advent of lasers, high intensity beams can actually result in nonlinear behavior of the output response. More interestingly, new lights at different frequency can be efficiently generated through the nonlinear frequency mixing process. This led to the birth of the nonlinear optics field. A general description of the material response can be obtained by taking the power series of the polarization P induced by the electric field E,

$$\tilde{P} = \varepsilon_o\left[\chi^{(1)}\tilde{E} + \chi^{(2)}\tilde{E}^2 + \chi^{(3)}\tilde{E}^3 + \cdots\right]. \tag{2.4}$$

$\chi^{(1)}$ is the linear susceptibility ($\chi^{(1)} = \varepsilon - 1$ for linear optics), while $\chi^{(2)}$ and $\chi^{(3)}$ are the second and third order nonlinear susceptibility. Typical second order nonlinear processes include second harmonic generation, sum- and difference-frequency generation, and optical parametric oscillation. Third order nonlinear processes involve an additional photon, examples include third harmonic generation, intensity-dependent refractive index, and four-wave mixing. From

Maxwell equations (Eqs. (1.1)), we can obtain the standard wave equations, except now with an additional term due to nonlinear polarization. For a dispersive medium, common for metamaterials, each frequency component of the electric fields should be treated separately. Hence the driven wave equation takes the form of

$$\nabla^2 \tilde{E}_n - \frac{\varepsilon^{(1)}(\omega_n)}{c^2}\frac{\partial^2 \tilde{E}_n}{\partial t^2} = \frac{1}{\varepsilon_o c^2}\frac{\partial^2 \tilde{P}_{n,NL}}{\partial t^2}, \tag{2.5}$$

where $\varepsilon^{(1)}$ is the linear permittivity which depends on frequency, and $\tilde{P}_{n,NL}$ is the nonlinear-induced polarization.

In nonlinear optics, phase-matching is the most important condition to satisfy for efficient nonlinear light generation. To explain this, a simple example of sum-frequency generation is shown in Fig. 2.11a below. Two frequency components of light ω_1 and ω_2 are incident on a nonlinear medium generating a new frequency ω_3, which is the sum of the incident frequencies. Using the slow-varying amplitude approximation, and through some mathematical simplifications [43], the amplitude of the newly-generated wave I_3 can be written as a function of wavevector mismatch Δk as follows.

$$I_3 \propto sinc^2\left(\frac{\Delta kL}{2}\right), \qquad \Delta k = k_1 + k_2 + k_3. \tag{2.6}$$

Fig. 2.11b shows that a $sinc^2$ function is maximized only when $\Delta k = 0$. At this perfect phase-matching condition, the nonlinear medium is most efficient in drawing energy from the incident beams and converts them to the new frequency component. The similar is true for other nonlinear $\chi^{(2)}$ and $\chi^{(3)}$ processes.

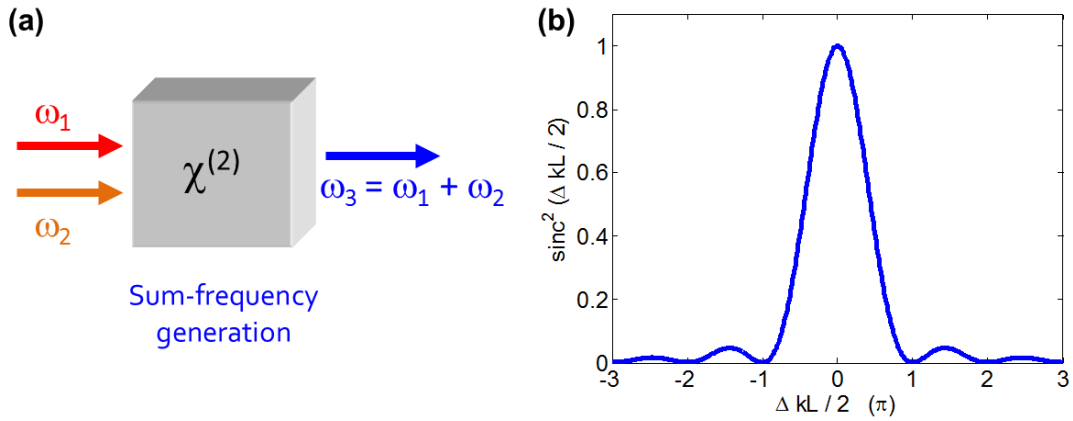

Figure 2.11 (a) Sum-frequency generation for a $\chi^{(2)}$ nonlinear medium. (b) When the phase-mismatch is at its minimum, $\Delta k = 0$, the largest response amplitude can be expected.

To increase the amounts of nonlinear light, a compensation technique must be used. The most widely used methods include birefringence phase-matching, angle phase matching and quasi phase matching (QPM) [44-47], as illustrated in Fig. 2.12. Implementing each of these techniques poses a number of challenges. The birefringence phase matching technique uses the

polarization dependent indices to match the phase velocities of the interacting waves, but is limited to birefringent materials [43,48]. Angle phase matching uses geometrical alignments of the interacting waves to compensate the phases, but the non-collinear optical arrangement limits the interaction length [43,48]. Quasi phase matching cancels out the inherent phase-mismatch using artificial momentum introduced by periodic and/or aperiodic poling of nonlinear crystals, which is however restricted to certain nonlinear crystals and provides limited range of mismatch that can be compensated. Moreover, all compensating schemes work only in a specific direction: either in the forward direction [44-47] or backward direction [49,50], but not both. This restriction arises because the phase matching process represents a balance between the momenta of the photons involved in the nonlinear interaction; a balance that is disturbed when the momentum of one photon changes sign due to a directional change.

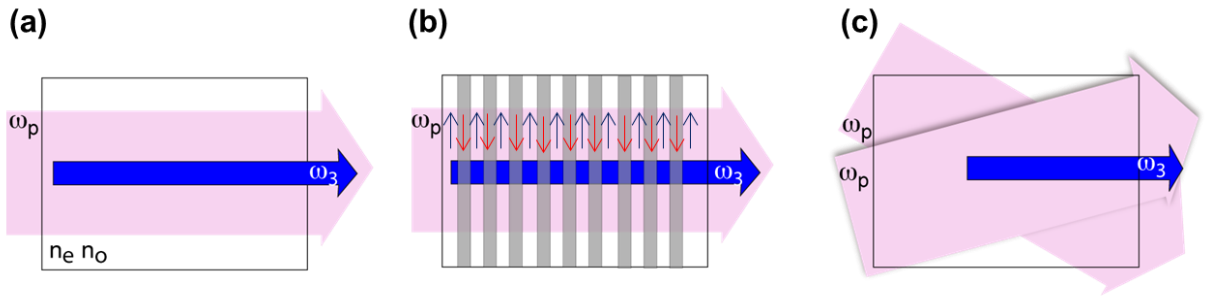

Figure 2.12 (a) Birefringence phase-matching, (b) quasi phase-matching and (c) angle phase-matching are the common techniques used to compensate the phase-mismatch in materials for efficient nonlinear generation of light.

In contrast, for a zero index metamaterial, a phase-mismatch free environment is intrinsically guaranteed for nonlinear propagation, since $k = \frac{w}{c} n = 0$, thus eliminating the requirement for phase matching. In addition, in a ZIM [7,51,52], the photons carry zero momentum and satisfy momentum conservation for any combination of photon directions, thereby allowing the nonlinearly generated waves to coherently build up in both forward and backward directions. In Chapter 1, we see how metamaterials allow us to tailor the linear electromagnetic response and introduce new regimes of interaction between radiation and matter. In fact, the nonlinear properties of negative index metamaterials have been explored both theoretically [53-56] and experimentally [57-61]. The rich nonlinear dynamical behavior in metamaterials promises the realization of novel effects such as backward mirrorless parametric amplification [53,54], novel quantum switches [55] and cavity-free microscopic optical parametric oscillators [56]. However, there is no reported experiment work on the nonlinear propagation within a bulk NIM or ZIM optical metamaterial thus far. This is due to the difficulty in fabricating high transmission multilayer bulk metamaterials in the optical regime.

Here we demonstrate the nonlinear dynamics in a bulk ZIM through a four-wave mixing (FWM) process (Fig. 2.13). Essentially two photons from the pump can mix with a signal photon to efficiently generate an idler photon, if both the energy and momentum are conserved. Importantly, FWM process is used instead of the more straightforward second and third harmonic generation to ensure that the medium can be treated as an effective medium for all the frequency components involved. Without loss of generality, we consider a degenerate FWM

process, in which the pump, signal, and idler photons have approximately the same wavelength $(\omega_{signal} \approx \omega_{pump} \approx \omega_{idler})$ to illustrate the phase-mismatch free nonlinear wave interactions in the ZIM. In this process, the phase (momentum) mismatch in the forward and backward propagation directions are $\Delta k_{\pm} = |2k_{pump} - k_{signal} \mp k_{idler}|$. The subscript "+" and "-" represent the forward and backward directions, respectively. In a conventional degenerate FWM system, when one of the propagation directions, say the forward direction, is perfectly phase-matched, *i.e.* $\Delta k_{+} \to 0$, the phase is then poorly matched in the backward propagation direction where $\Delta k_{-} \approx 2|k_{idler}|$.

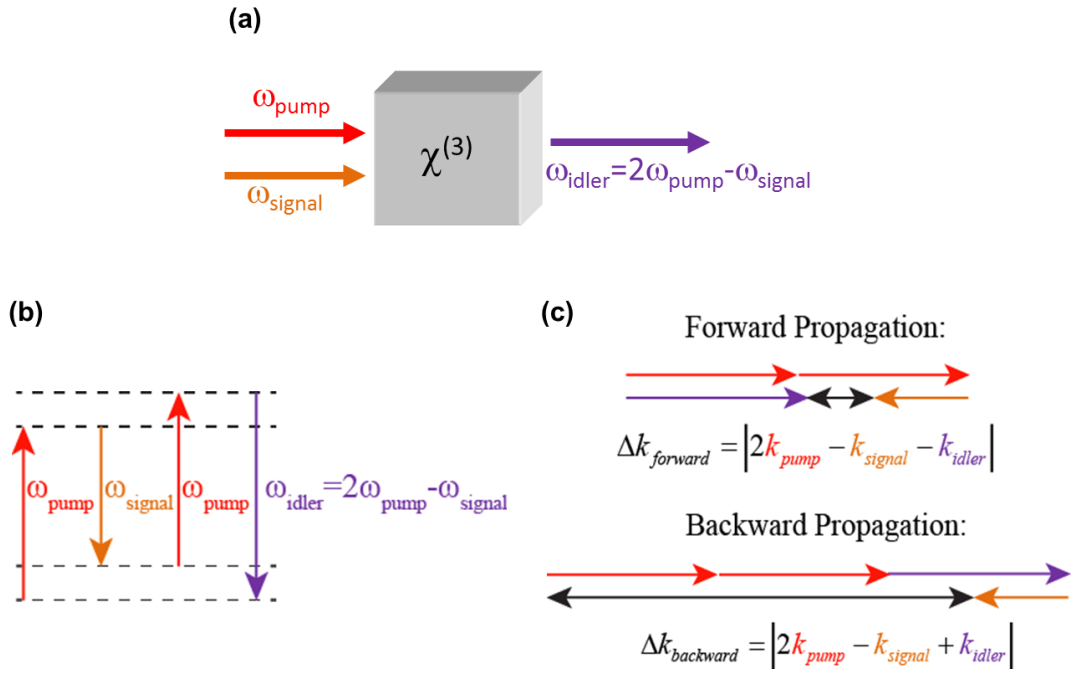

Figure 2.13 (a) Four-wave mixing (FWM) involving two photons from the pump, and a photon from the signal and idler beam. (b) Energy conversation and (c) momentum conversation $\Delta k_{\pm} = 0$ required for efficient nonlinear light generation.

For a ZIM at the idler frequency, however, both the phase-mismatch in the forward and backward directions are zero. This important distinction between forward and backward nonlinear propagation allows us to explore nonlinear generation for negative, positive and zero index regimes. We expect that in the case of negative or positive index, due to the fact that $\Delta k_{+} \to 0$, while $\Delta k_{-} \neq 0$, the generated forward light is accumulated in phase, while the generated backward light is not, thus causing the degenerated FWM intensity to grow monotonically for the forward direction and to oscillate for backward direction (Fig. 2.14a). On the contrary, in the zero index regime, $\Delta k_{+} \to 0$, and also $\Delta k_{-} \to 0$, making both the generated forward light and backward light accumulated in phase, having the same yield in the forward and backward directions are expected (Fig. 2.14b). This is in stark contrast to nonlinear generation in negative index materials, where the phase-mismatch parameter has a finite value [53-56]. Phase-mismatch free zero index material allows the nonlinear process to be efficient regardless of directionality, and the need to carefully balance between the momenta of the waves involved in the nonlinear interaction is eliminated. The pump pulse has a positive Poynting vector so the

direction of energy flux is the same as in free space. In contrast the nonlinear emission has an energy flux in both directions, with the relative amounts influenced by the phase matching. The refractive index controls the direction of the phase velocity and canonical momentum relative to the direction of the energy flux [53-62], which influences the direction of energy propagation through the phase matching. In a zero index medium, as seen, the energy flux in both directions is equal. Compared to the poorly phase-matched case, more energy will be extracted from the pump in a ZIM.

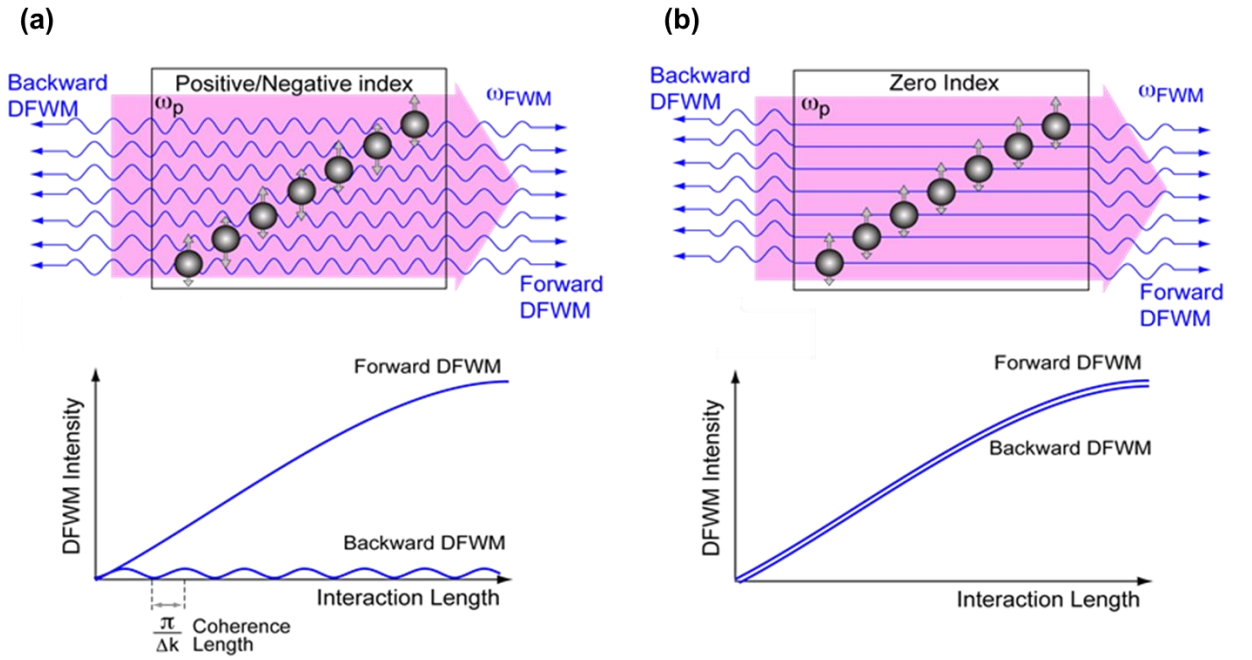

Figure 2.14 In the microscopic picture of nonlinear generation, each source coherently emits equally in both directions acquiring a phase proportional to the refractive index as it propagates. All of these sources add up coherently to generate the net nonlinear emission. (a) In a finite index medium, the emission acquires phase as it propagates, leading to destructive interference when the process is not phase matched. For example, in a degenerate four wave mixing process in which $\omega_{signal} \approx \omega_{pump} \approx \omega_{idler}$, the sources destructively interfere in the backward direction, resulting in weaker backward emission. (b) In a zero index medium, the radiation from all nonlinear sources acquires no phase as they propagate, guaranteeing a constructive interference and an increase of the signal in both directions with propagation length.

For the experimental realization, we fabricated a 20-layer fishnet metamaterial with alternating layers of 30 nm gold and 50 nm magnesium fluoride on a 50-nm-thick silicon nitride membrane. A cross fishnet structure is used instead of the regular rectangular fishnet structure so that it can operate for both polarizations in the near-infrared wavelengths. Also, gold is used instead of the less-lossy silver, for gold is more robust under high power excitation. The magnetic moments, created by the antiparallel currents in neighboring conductive layers, and the electric responses of the perforated metallic thin films provide either a positive, zero, or negative refractive index regime depending on the wavelength. The fabrication steps (Fig. 2.15) are similar to the case of visible fishnets described in Chapter 2.2, except it involves many more evaporation runs and higher aspect ratio in FIB milling. The fabricated sample with a period of 750 nm and cross lateral holes of dimensions 475 nm (H) and 175 nm (V) is shown in Fig. 2.16. Low transmission

loss is critical for observing the effects of phase matching. High losses can also strongly affect the ratio between the forward and backward nonlinear emission for positive, negative, and zero index regimes. It decreases the overall nonlinear emission, and due to the shorter propagation length of backward emission, increases the backward emission relative to the forward. The fabricated fishnet has a relatively low loss at the zero-index regime, allowing us to observe the effects of phase matching rather than absorption.

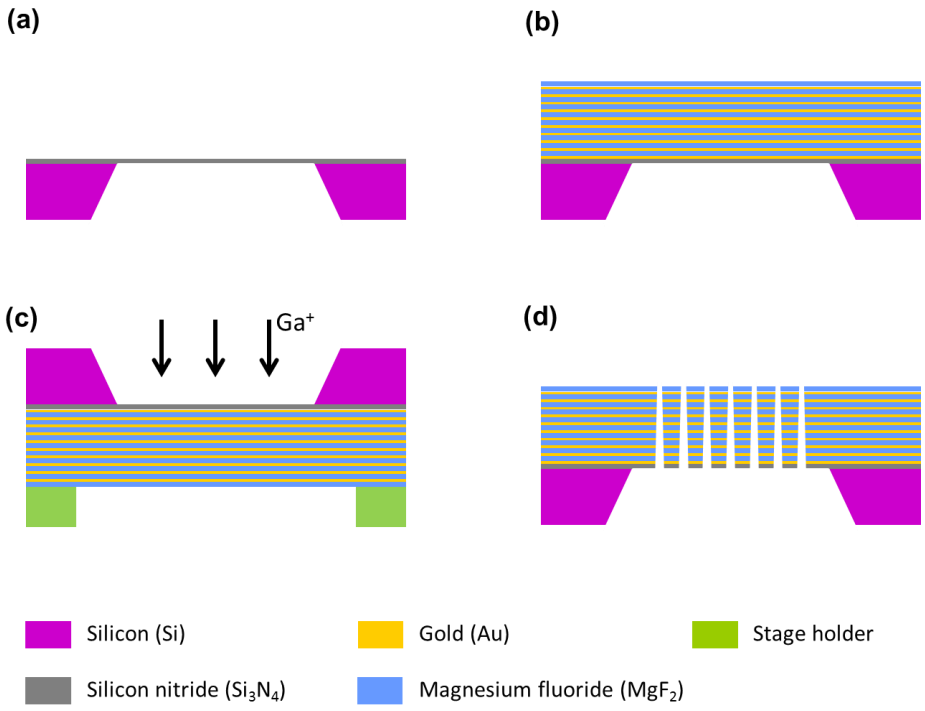

Figure 2.15 Schematic of the key fabrication steps for cross fishnet working in the near-infrared wavelengths. (a) Fabrication of a low-stress Si_3N_4 free-standing membrane. (b) Multilayer electron beam evaporation of Au and MgF_2 layers without vacuum break. (c) Flip side mounting of sample followed by Ga^+ focused ion beam milling to pattern the nanostructures. (d) Final suspended fishnet structure.

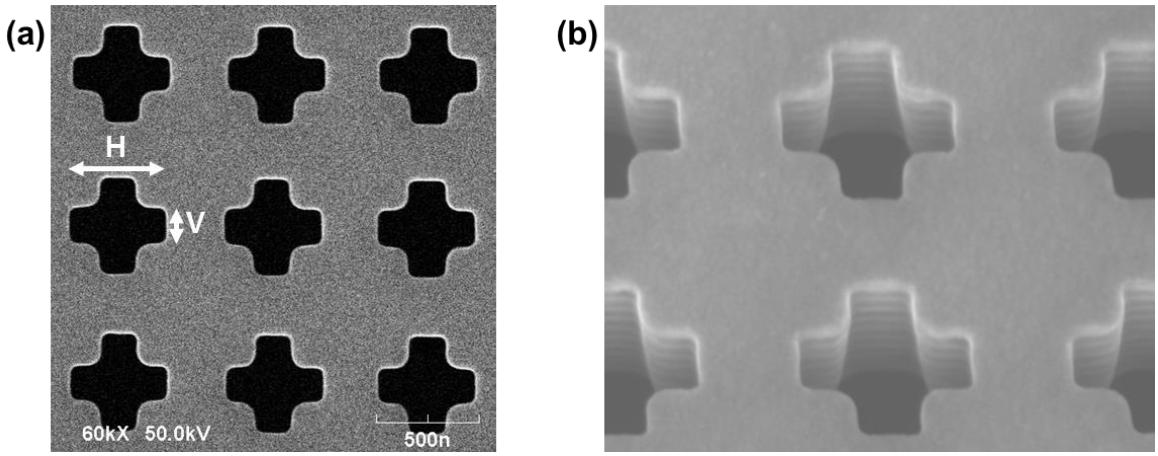

Figure 2.16 (a) SEM image of the fabricated bulk 3D cross fishnet. (b) A tilted view of the fishnet showing the 20 physical layers of Au/MgF_2.

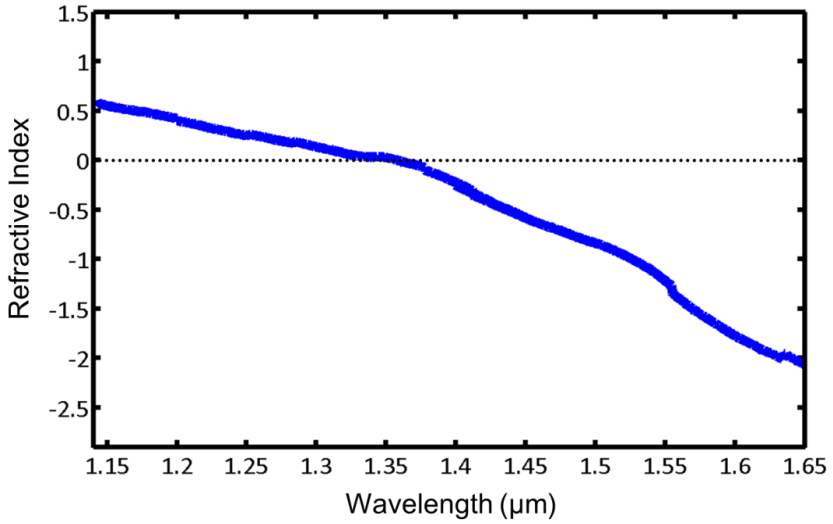

Figure 2.17 Refractive index of the bulk cross fishnet measured using a spectrally and spatially resolved interferometry. Zero refractive index happens at around 1325-1340 nm.

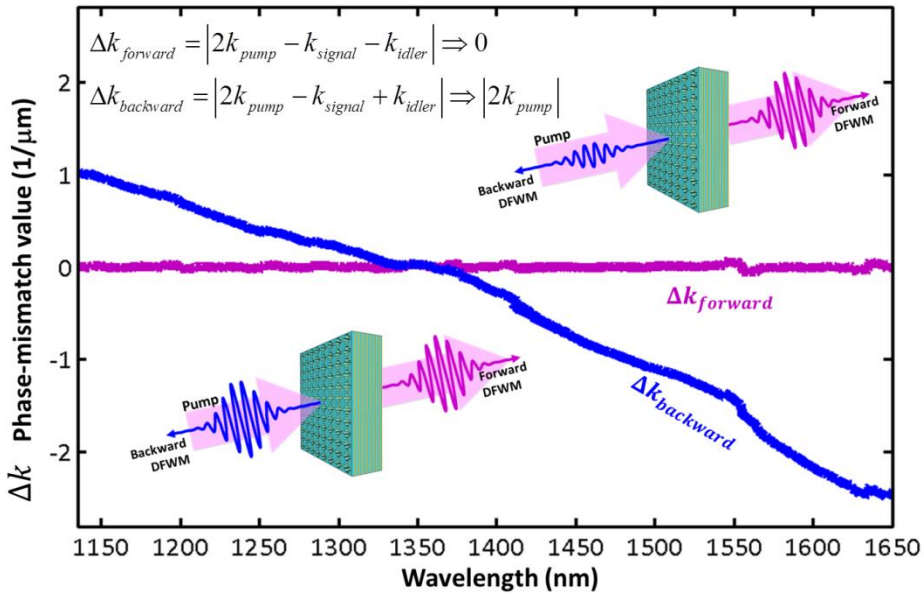

Figure 2.18 The phase-mismatch of the forward (purple) and backward (blue) four wave mixing as a function of wavelength, based on experimentally measured refractive indices. The forward phase-mismatch is near zero ($\Delta k_+ \to 0$) for all wavelengths, while the backward has a large phase mismatch ($\Delta k_- \neq 0$) except when the index is near zero.

We measured the transmission and refractive index using spectrally and spatially resolved interferometry [8], which measures simultaneously the phase for an ultra-broadband optical range to an accuracy of greater than $\lambda/300$. The zero crossing of the index is at approximately 1325-1340 nm, as shown in Fig. 2.17. Using the measured refractive index values of the fishnet structures, the phase-mismatch values can be calculated as a function of wavelength for forward and backward propagation (Fig. 2.18). The forward phase-mismatch is $\Delta k_+ \to 0$ for all

wavelengths, while Δk_{-} has different values across the zero index wavelength. However, in the wavelength regime of zero refractive index (~1330 nm), both the forward and backward directions are phase-mismatch free.

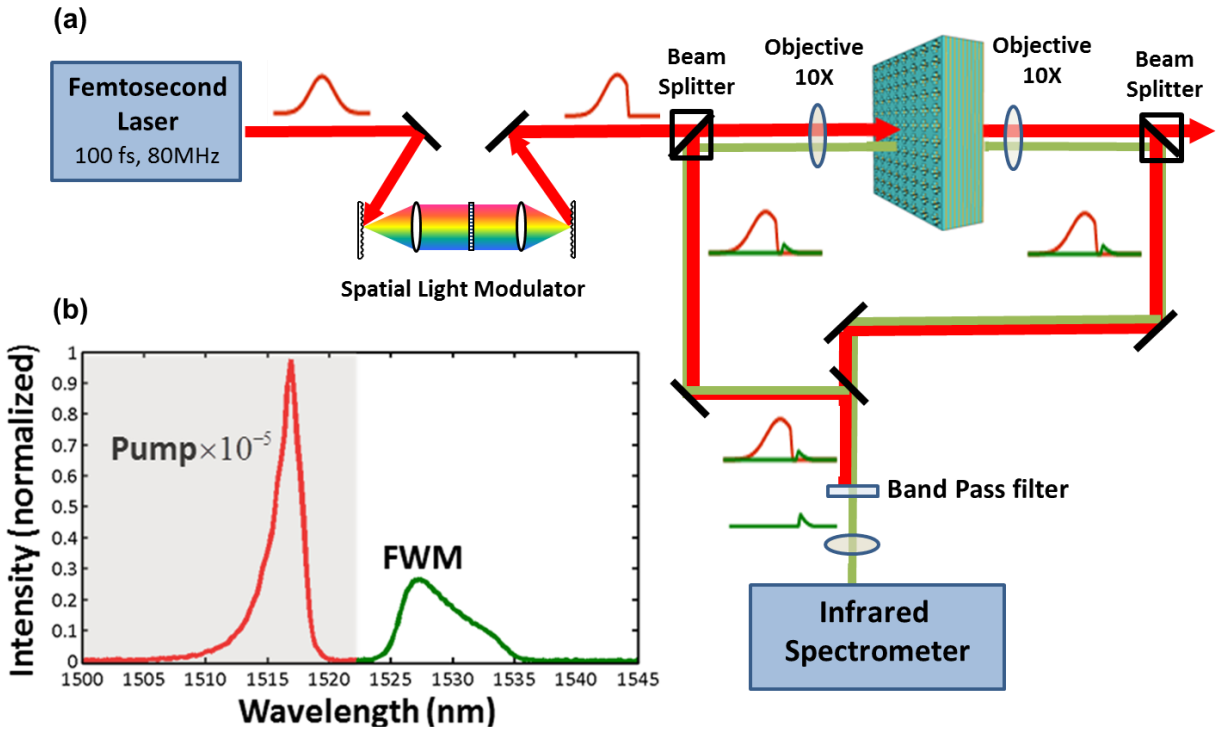

Figure 2.19 (a) Experimental apparatus for nonlinear measurements. A transform limited 100 fs laser pulse centered at 1315 nm or 1510 nm was amplitude shaped through a spatial light modulator (SLM) to remove the long wavelength tail of the pulse (red). The pulse was passed through a fishnet metamaterial, which generates a four wave mixing nonlinear signal (green) in the backward and forward directions due to a third order nonlinearity. The four wave mixing signals were measured in an infrared spectrometer after bandpass filtering the pump pulse. The forward emission was measured without the flip mirror. An analyzer was used before the spectrometer to control the detected polarization and a half wave plate (not shown) was used to control the pump polarization. (b) An example measurement of the emission spectrum, showing both the generated four wave mixing signal (green) and the filtered pump (red). The pump is undepleted by the nonlinear process as evident by the much weaker four wave mixing signal than that of the pump (the magnitude of the four wave mixing is ~10^{-5} times the pump intensity), justifying the use of the perturbative approach in our analysis.

To characterize the nonlinear response, we use a single-shot FWM technique which allows intrapulse wave mixing from the different spectral components of ultrashort (broadband) pump laser pulses [63]. The experimental apparatus is illustrated in Fig. 2.19a. Before impinging on the samples the transform limited pump pulse is first amplitude shaped to remove the long wavelength tail in the spectral domain. The generated intrapulse FWM can be measured in both forward and backward directions within this filtered spectral regime. This method eliminates the needs of overlapping two laser pulses temporally and spatially, and maximizes the nonlinear yield. An example of such a measurement spectra (Fig. 2.19b) shows both the generated FWM signals, with their relative strengths. Note that the pump is far from depleted by the nonlinear process as evident by the much weaker FWM signal than that of the pump. Operating in the

weak field regime (the generated intensity of the idler is on the order of $10^{-5}$of the pump intensity) allows us to analyze the experimental observations with a perturbative approach. We verify the nonlinear origin of the emission by measuring the cubic scaling with pump power, as shown in Fig. 2.20.

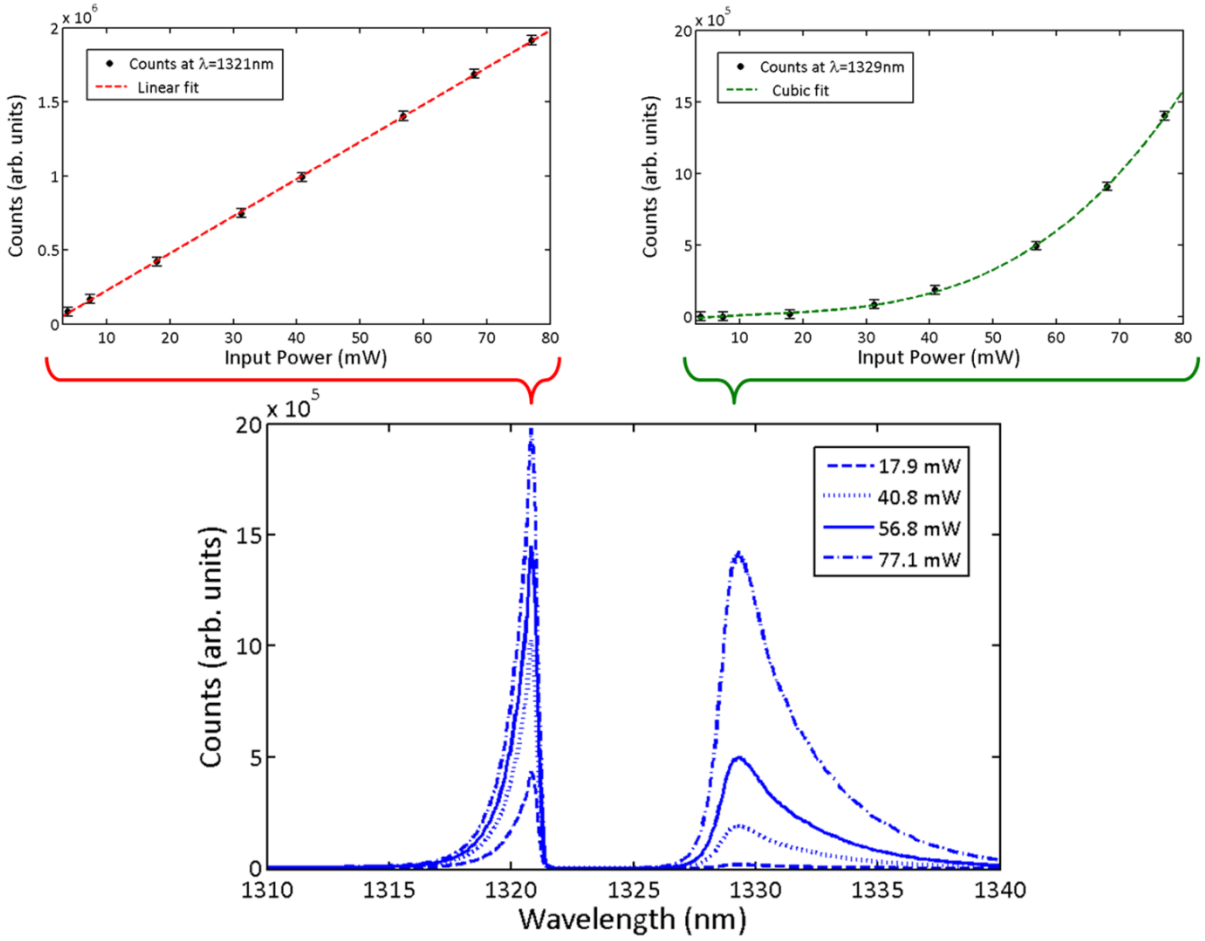

Figure 2.20 Power Scaling of the pump and four wave mixing in a single-shot FWM spectral measurement. Both the four wave mixing signal and remaining pump pulse are observed in the spectral measurements, and can be differentiated by their spectral location. At the bottom panel, several spectral measurements are plotted for different pump intensities. The remaining pump (at shorter wavelengths) is found to scale linearly with the pump power (upper left panel in red), while the four wave mixing signal is proportional to the third power of the pump power as expected for a third order nonlinear process (upper right panel in green).

The intrapulse FWM signal in the zero index regime (where the refractive index changes its sign) is shown for both the forward (solid purple) and the backward (dashed blue) directions (Fig. 2.21a). The observed nonlinear yields are about the same in both directions. In contrast, in the negative index regime, the intensity of the degenerate FWM signals in the opposite propagation directions are distinctively different (Fig. 2.22a). Due to the low transmission at 1530 nm, a different fishnet metamaterial with 800 nm period and a perforated hole size of 560 nm (H) and 250 nm (V) is used. The zero crossing of the refractive index is at ~1460 nm and the refractive index is $n' = -0.5$ at 1530 nm. The relative strength of the forward and backward FWM waves

correlates with the predicted phase matching difference for zero and negative indices, as illustrated in Fig 2.14. In particular, at the zero refractive index region, the observation of a forward/backward FWM ratio of unity indicates phase-mismatch free nonlinear interaction for both directions.

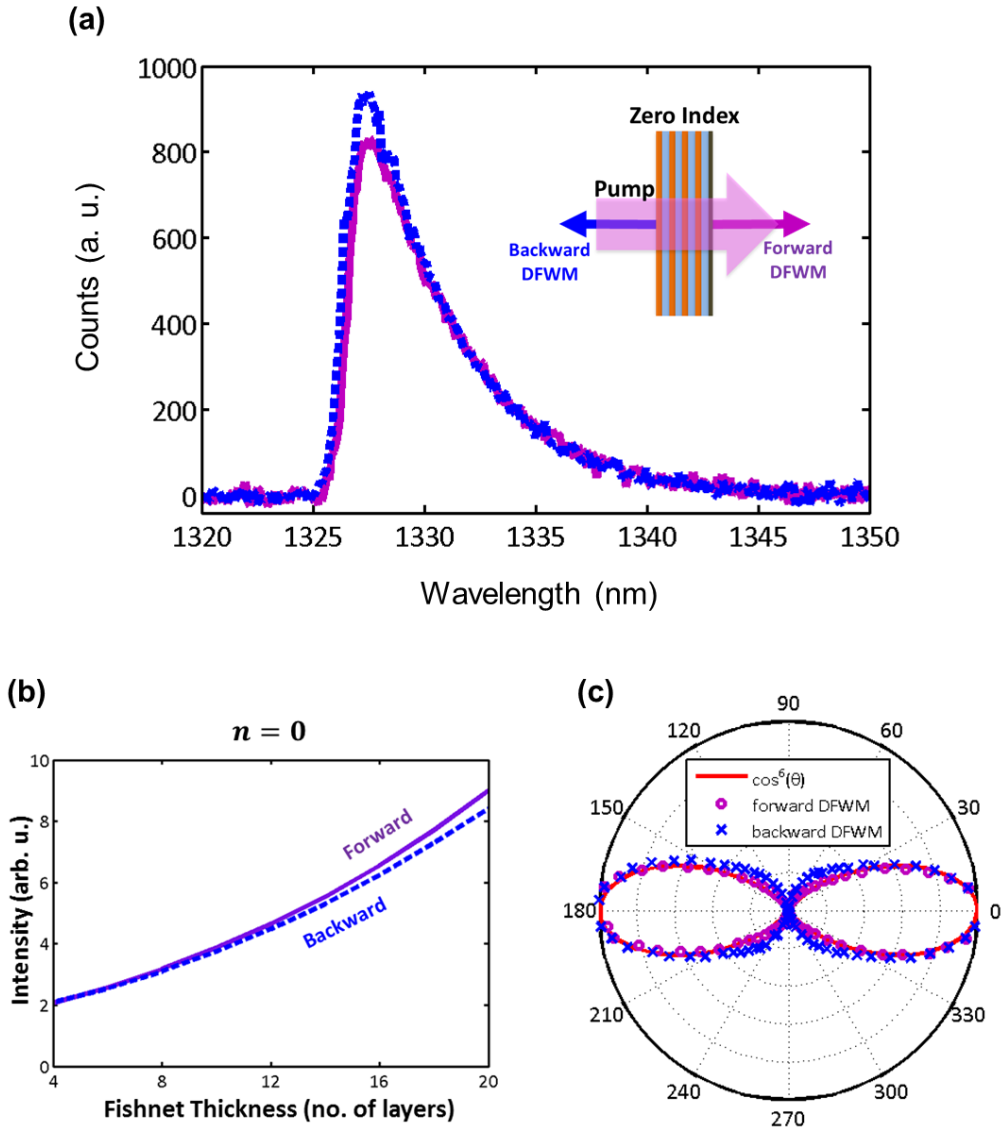

Figure 2.21 Nonlinear FWM at the zero index regime. (a) The measured four wave mixing process in a bulk ZIM has almost the same yield in both directions, illustrating the phase mismatch-free properties of zero index materials. (b) Numerical simulations of nonlinear emission as a function of metamaterial thickness for ZIM where the nonlinear yield in the forward and backward directions is similar and both increase with material thickness due to constructive interference. (c) The dependence of the nonlinear emission (with a horizontally polarized analyzer) on pump polarization, which has the characteristic $cos^6(\theta)$ of $\chi^{(3)}$ dynamics.

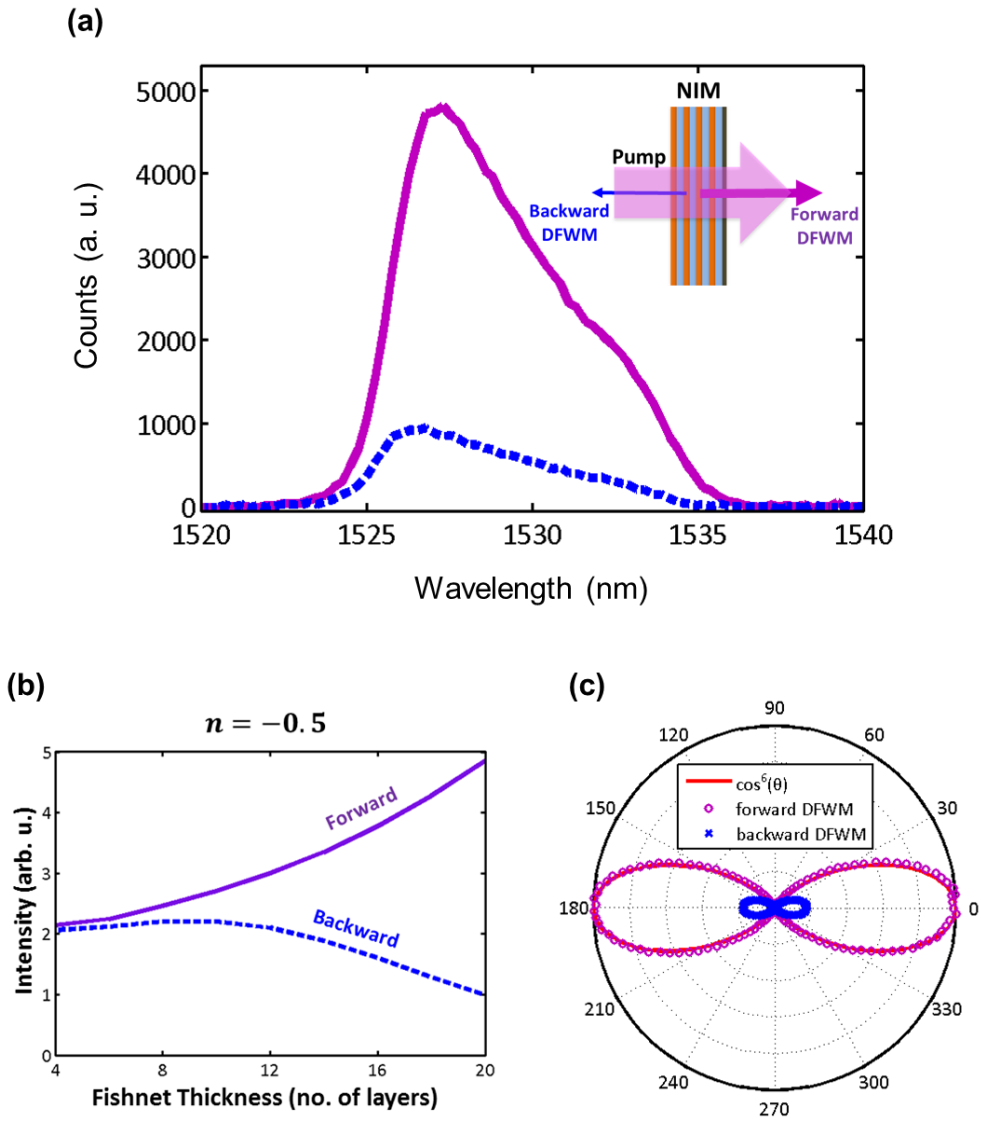

Figure 2.22 Nonlinear FWM at the negative index regime. (a) The forward propagating four wave mixing (solid purple) is much stronger than the backward in a bulk NIM, due to the phase mismatch. (b) Numerical simulations of nonlinear emission as a function of metamaterial thickness for NIM where only the forward emission increases with material thickness, while the backward emission decreases due to the large phase-mismatch of the finite index material. (c) The dependence of the nonlinear emission (with a horizontally polarized analyzer) on pump polarization for a NIM, which has the characteristic $cos^6(\theta)$ of $\chi^{(3)}$ dynamics, but with a significantly different amplitude for the forward and backward signals.

We also perform numerical simulation to estimate the far-field nonlinear response at different refractive index regimes using the Lorentz reciprocity formalism [64]. For a bulk ZIM, the simulation of the dynamics as a function of thickness predicts a ratio of unity for forward/backward nonlinear emission (Fig. 2.21b); whereas for a bulk NIM, the forward generated nonlinear signal has a much higher yield than that of the backward signal (Fig. 2.22b) for a thick fishnet of 20 layers. In contrast, for thin fishnets (less than 5 layers), the forward/backward ratio is unity regardless of the index of refraction, indicating that phase

matching is not important in these structures [58-61]. The nonlinear simulation is performed with nonlinear scattering theory [64], which calculates the nonlinear properties using the linear results from a full wave simulation of the metamaterial, taking into account the fabricated structure geometry and material losses. To further confirm that phase plays a dominant role in the dynamics and not the loss or surface effects, we artificially remove the phase-mismatch in the nonlinear simulation while keeping loss, thus forcing all waves to add up constructively. We find that the behavior in the zero index region is unchanged, indicating that phase matching plays little role. In contrast, in the negative index region, the forward and backward emissions are now nearly equal, indicating that phase matching is critical in this region. It is worth noting that perfect phase matching using a zero refractive index is different than quasi-phase matching [45], in which the effective momentum supplied by a periodic structuring is used to compensate for a phase mismatch. In these experiments, the sub-wavelength spacing of the layers (80 nm) does not provide sufficient effective momentum to phase match the backward nonlinear generation.

The phase-mismatch free nonlinear generation can be further demonstrated by measuring the nonlinear emission as a function of the polarization angle of the pump for the forward and backward FWM, as shown in Fig. 2.21c (for bulk ZIM) and Fig. 2.22c (for bulk NIM). The relative strength between the forward and backward nonlinear waves in the zero index region is again about the same for all polar angles, while in the negative index regime, the forward nonlinear waves remain stronger than the backward for all polarizations. The polarization dependent FWM (with a horizontally polarized analyzer) matches well the analytical curve of $\cos^6\theta$, a characteristic response of a third order nonlinearity signal. This angular dependence is particularly important as it means that the nonlinearity is originated from the light that is coupled into the metamaterial, and is not a surface nonlinearity associated with the layered structure.

2.5 Summary and Outlook

In this chapter, we have experimentally showed the strategy to attain low-loss, high transmission bulk fishnet NIM and ZIM operating in both the visible and near infrared wavelengths. The phase and refractive index results are confirmed by the spectrally and spatially resolved broadband Mach-Zehnder interferometry setup. In addition, we realized the first magnetic hyperbolic dispersion in a bulk metamaterial. Using the bulk ZIM structure, we also demonstrated phase-mismatch free nonlinear generation using intrapulse four-wave mixing. In contrast to phase-mismatch compensation techniques in conventional nonlinear media, a ZIM eliminates the need for phase-matching, allowing efficient nonlinear generation in both forward and backward directions.

The concept of phase-mismatch free nonlinear interaction in a ZIM provides a new degree of freedom in controlling the nonlinear dynamics in a metamaterial and can be further explored in other nonlinear processes such as coherent Raman for remote sensing applications or spontaneous parametric down-conversions for entangled photon generation. The design of multi-valued or broadband ZIMs can open new opportunities to achieve phase-mismatch free dynamics for simultaneous nonlinear processes. I also look forward to see different nonlinear wave mixing processes to be demonstrated in the visible regime.

References

[1] G. Dolling, C. Enkrich, M. Wegener, C. M. Soukoulis, and S. Linden, "Low-loss negative-index metamaterial at telecommunication wavelengths," *Optics Letters* **31**, 1800 (2006).

[2] G. Dolling, M. Wegener, C. M. Soukoulis, and S. Linden, "Negative-index metamaterial at 780 nm wavelength," *Optics Letters* **32**, 53 (2007).

[3] G. Dolling, M. Wegener, and S. Linden, "Realization of a three-functional layer negative-index photonic metamaterial," *Optics Letters* **32**, 551 (2007).

[4] U.K. Chettiar, A. V. Kildishev, H. K. Yuan, W. S. Cai, S. M. Xiao, V. P. Drachev, and V. M. Shalaev, "Dual-band negative index metamaterial: double negative at 813 nm and single negative at 772 nm," *Optics Letters* **32**, 1671 (2007).

[5] U. K. Chettiar, S. Xiao, A. V. Kildishev, W. Cai, H. K. Yuan, V. P. Drachev, and V. M. Shalaev, "Optical metamagnetism and negative-index metamaterials," *MRS Bulletin* **33**, 921 (2008).

[6] S. Xiao, U. K. Chettiar, A. V. Kildishev, V. P. Drachev, and V. M. Shalaev, "Yellow-light negative-index metamaterials," *Optics Letters* **34**, 3478 (2009).

[7] J. Valentine, S. Zhang, T. Zentgraf, E. Ulin-Aliva, D. A. Genov, G. Bartal, and X. Zhang, "Three-dimensional optical metamaterial with a negative refractive index," *Nature* **455**, 376 (2008).

[8] K. O'Brien, N. D. Lanzillotti-Kimura, H. Suchowski, B. Kante, Y. Park, X. Yin, and X. Zhang, "Reflective interferometry for optical metamaterial phase measurements," *Optics Letters* **37**, 4089 (2012).

[9] D. R. Smith and D. Schurig, "Electromagnetic wave propagation in media with indefinite permittivity and permeability tensors," *Physical Review Letters* **90**, 077405 (2003).

[10] S. S. Kruk, D. A. Powell, A. Minovich, D. N. Neshev, and Y. S. Kivshar, "Spatial dispersion of multilayer fishnet metamaterials," *Optics Express* **20**, 15100 (2012).

[11] A. Poddubny, I. Iorsh, P. Belov, and Y. Kivshar, "Hyperbolic metamaterials," *Nature Photonics* **7**, 948 (2013).

[12] H. N. S. Krishnamoorthy, Z. Jacob, E. Narimanov, I. Kretzschmar, and V. M. Menon, "Topological transition in metamaterials," *Science* **336**, 205 (2012).

[13] J. Yao, Z. Liu, Y. Liu, Y. Wang, C. Sun, G. Bartal, A. M. Stacy, and X. Zhang, "Optical negative refraction in bulk metamaterials of nanowires," *Science* **321**, 930 (2008).

[14] M. Noginov, Y. A. Barnakov, G. Zhu, T. Tumkur, H. Li, and E. Narimanov, "Bulk photonic metamaterial with hyperbolic dispersion," *Applied Physics Letters* **94**, 151105 (2009).

[15] A. Kabashin, P. Evans, S. Pastkovsky, W. Hendren, G. Wurtz, R. Atkinson, R. Pollard, V. Podolskiy, and A. Zayats, "Plasmonic nanorod metamaterials for biosensing," *Nature Materials* **8**, 867 (2009).

[16] J. Kanungo and J. Schilling, "Experimental determination of the principal dielectric functions in silver nanowire metamaterials," *Applied Physics Letters* **97**, 021903 (2010).

[17] M. Noginov, H. Li, Y. A. Barnakov, D. Dryden, G. Nataraj, G. Zhu, C. Bonner, M. Mayy, Z. Jacob, and E. Narimanov, "Controlling spontaneous emission with metamaterials," *Optics Letters* **35**, 1863 (2010).

[18] G. A. Wurtz, R. Pollard, W. R. Hendren, G. P. Wiederrecht, D. J. Gosztola, V. A. Podolskiy, and A. V. Zayats, "Designed ultrafast optical nonlinearity in a plasmonic nanorod metamaterial enhanced by nonlocality," *Nature Nanotechnology* **6**, 107 (2011).

[19] J. Sun, N. M. Litchinitser, and J. Zhou, "Indefinite by nature: from ultraviolet to terahertz," *ACS Photonics* **1**, 293 (2014).

[20] S. Dai, Z. Fei, Q. Ma, A. S. Rodin, M. Wagner, A. McLeod, M. K. Liu, W. Gannett, W. Regan, K. Watanabe, T. Taniguchi, M. Thiemens, G. Dominguez, A. H. Castro Neto, A. Zettl, F. Keilmann, P. Jarillo-Herrero, M. M. Fogler, and D N.Basov, *Science* **343**, 1125 (2014).
[21] P. Li, M. Lewin, A. V. Kretinin, J. D. Caldwell, K. S. Novoselov, T. Taniguchi, K. Watanabe, F. Gaussmann, and T. Taubner, "Hyperbolic phonon-polaritons in boron nitride for near-field optical imaging and focusing," *Nature Communications* **6**, 7507 (2015).
[22] S. Dai, Q. Ma, T. Andersen, A. McLeod, Z. Fei, M. Liu, M. Wagner, K. Watanabe, T. Taniguchi, M. Thiemens, F. Keilmann, P. Jarillo-Herrero, M. M. Fogler, and D. N. Basov, "Subdiffractional focusing and guiding of polaritonic rays in a natural hyperbolic material," *Nature Communications* **6**, 6963 (2015).
[23] A. S. Potemkin, A. N. Poddubny, P. A. Belov, and Y. S. Kivshar, "Green function for hyperbolic media," *Physical Review A* **86**, 023848 (2012).
[24] T. Galfsky, H. N. S. Krishnamoorthy, W. Newman, E. E. Narimanov, Z. Jacob, and V. M. Menon, "Active hyperbolic metamaterials: enhanced spontaneous emission and light extraction," *Optica* **2**, 62 (2015).
[25] D. R. Smith, P. Kolinko, and D. Schurig, "Negative refraction in indefinite media," *Journal of Optical Society of America* B **21**, 1032 (2004).
[26] R. Hussain, S. S. Kruk, C. E. Bonner, M. A. Noginov, I. Staude, Y. S. Kivshar, N. Noginova, and D. N. Neshev, "Enhancing Eu^{3+} magnetic dipole emission by resonant plasmonic nanostructures," *Optics Letters* **40**, 1659 (2015).
[27] M. Kasperczyk, S. Person, D. Ananias, L. D. Carlos, and L. Novotny, "Excitation of magnetic dipole transitions at optical frequencies," *Physical Review Letters* **114**, 163903 (2015).
[28] C. Fietz, Y. Urzhumov, and G. Shvets, "Complex k band diagrams of 3D metamaterial/photonic crystals," *Optics Express* **19**, 19027 (2011).
[29] D. R. Smith, S. Schultz, P. Markoš, and C. M. Soukoulis, "Determination of effective permittivity and permeability of metamaterials from reflection and transmission coefficients," *Physical Review B* **65**, 195104 (2002).
[30] B. Saleh and M. Teich, "Fundamentals of Photonics", Wiley (2007).
[31] E. Cuche, P. Marquet, and C. Depeursinge, "Simultaneous amplitude-contrast and quantitative phase-contrast microscopy by numerical reconstruction of Fresnel off-axis holograms," *Applied Optics* **38**, 6994 (1999).
[32] A. Alu, M. G. Silveirinha, A. Salandrino, and N. Engheta, "Epsilon-near-zero metamaterials and electromagnetic sources: Tailoring the radiation phase pattern," *Physical Review B* **75**, 155410 (2007).
[33] N. Engheta and R. Ziolkowski, "Metamaterials: Physics and Engineering Explorations," Wiley (2006).
[34] H. R. Philipp, "Optical properties of silicon nitride," *Journal of the Electrochemical Society* **120**, 295 (1973).
[35] J. Kischkat, S. Peters, B. Gruska, M. Semtsiv, M. Chashnikova, M. Klinkmuller, O. Fedosenko, S. Machulik, A. Aleksandrova, G. Monastyrskyi, Y. Flores, and W. T. Masselink, "Mid-infrared optical properties of thin films of aluminum oxide, titanium dioxide, silicon dioxide, aluminum nitride, and silicon nitride," *Applied Optics* **51**, 6789 (2012).
[36] H. Li, "Refractive index of alkaline earth halides and its wavelength and temperature derivatives," *Journal of Physical and Chemical Reference Data* **9**, 161 (1980).

[37] P. B. Johnson and R.-W. Christy, "Optical Constants of the Noble Metals," *Physical Review B* **6**, 4370 (1972).
[38] M. A. Gorlach and P. A. Belov, "Nonlocality in uniaxially polarizable media," arXiv:1505.01064 (2015).
[39] A. A. Orlov, P. M. Voroshilov, P. A. Belov, and Y. S. Kivshar, "Engineered optical nonlocality in nanostructured metamaterials," *Physical Review B* **84**, 045424 (2011).
[40] N. Liu, H. Guo, L. Fu, S. Kaiser, H. Schweizer, and H. Giessen, "Three-dimensional photonic metamaterials at optical frequencies," *Nature Materials* **7**, 31 (2008).
[41] J. B. Pendry, "A chiral route to negative refraction," *Science* **306**, 1353 (2004).
[42] J. K. Gansel, M. Thiel, M. S. Rill, M. Decker, K. Bade, V. Saile, G. von Freymann, S. Linden, and M. Wegener, "Gold helix photonic metamaterial as broadband circular polarizer," *Science* **325**, 1513 (2009).
[43] R. Boyd, "Nonlinear Optics", Academic Press (2008).
[44] J. A. Armstrong, N. Bloembergen, J. Ducuing and P. S. Pershan, "Interactions between light waves in a nonlinear dielectric," *Physical Review* **127**, 1918 (1962).
[45] D. S. Hum and M. M. Fejer, "Quasi-phasematching," *Comptes Rendus Physique* **8**, 180 (2007).
[46] A. Arie and N. Voloch, "Periodic, quasi-periodic, and random quadratic nonlinear photonic crystals," *Laser and Photonics Reviews* **4**, 355 (2010).
[47] A. Rose and D. R. Smith, "Overcoming phase-mismatch in nonlinear metamaterials," *Optical Materials Express* **1**, 1232 (2011).
[48] Y. R. Shen, "The Principles of Nonlinear Optics," Wiley-Interscience (1984).
[49] X. Gu, R. Y. Korotkov, Y. J. Ding, J. U. Kang, and J. B. Khurgin, "Backward second-harmonic generation in periodically poled lithium niobate," *Journal Optical Society of America B* **15**, 1561 (1998).
[50] C. Canalias and V. Pasiskevicius, "Mirrorless optical parametric oscillator," *Nature* Photonics **1**, 459 (2007).
[51] C. Argyropoulos, P. Y. Chen, G. D'Aguanno, N. Engheta, and A. Alu, "Boosting optical nonlinearities in near-zero plasmonic channels," *Physical Review B* **85**, 045129 (2012).
[52] E. J. R. Vesseur, T. Coenen, H. Caglayan, N. Engheta, and A. Polman, "Experimental verification of n = 0 structures for visible light," *Physical Review Letters* **110**, 013902 (2013).
[53] A. K. Popov and V. M. Shalaev, "Negative-index metamaterials: Second-harmonic generation, Manley-Rowe relations and parametric amplification," *Applied Physics B* **84**, 131 (2006).
[54] A. K. Popov and V. M. Shalaev, "Compensating losses in negative-index metamaterials by optical parametric amplification," *Optics Letters* **31**, 2169 (2006).
[55] A. K. Popov, S. A. Myslivets, and V. M. Shalaev, "Microscopic mirrorless negative-index optical parametric oscillator," *Optics Letters* **34**, 1165 (2009).
[56] M. Scalora, G. D'Aguanno, M. Bloemer, M. Centini, D. de Ceglia, N. Mattiucci, and Y. S. Kivshar, "Dynamics of short pulses and phase matched second harmonic generation in negative index materials," *Optics Express* **14**, 4746 (2006).
[57] A. Rose, D. Huang, and D. R. Smith, "Controlling the second-harmonic in a phase-matched negative-index metamaterial," *Physical Review Letters* **107**, 063902 (2011).
[58] S. Tang, D. J. Cho, H. Xu, W. Wu, Y. R. Shen, and L. Zhou, "Nonlinear responses in optical metamaterials: Theory and experiment," *Optics Express* **19**, 18283 (2011).

[59] K. M. Dani, Z. Ku, P. C. Upadhya, R. P. Prasankumar, S. R. J. Brueck, and A. J. Taylor, "Sub-picosecond optical switching with a negative index metamaterial," *Nano Letters* **9**, 3565 (2009).
[60] A. Minovich, J. Farnell, D. N. Neshev, I. McKerracher, F. Karouta, J. Tian, D. A. Powell, I. V. Shadrivov, H. H. Tan, C. Jagadish, and Y. S. Kivshar, "Liquid crystal based nonlinear fishnet metamaterials," *Applied Physics Letters* **100**, 1211131 (2012).
[61] J. Reinhold, M. R. Shcherbakov, A. Chipouline, V. I. Panov, C. Helgert, T. Paul, C. Rockstuhl, F. Lederer, E.-B. Kley, A. Tünnermann, A. A. Fedyanin, and T. Pertsch, "Contribution of the magnetic resonance to the third harmonic generation from a fishnet metamaterial," *Physical Review B* **86**, 115401 (2012).
[62] S. M. Barnett, "Resolution of the Abraham-Minkowski dilemma," *Physical Review Letters* **104**, 070401 (2010).
[63] N. Dudovich, D. Oron, and Y. Silberberg, "Single-pulse coherently controlled nonlinear Raman spectroscopy and microscopy," *Nature* **418**, 512 (2002).
[64] S. Roke, M. Bonn, and A. V. Petukhov, "Nonlinear optical scattering: The concept of effective susceptibility," *Physical Review B* **70**, 115106 (2004).

Chapter 3

Engineering the Imaginary Part of Refractive Index

3.1 Parity-time (PT) Symmetry

Engineering of the imaginary part of refractive index is often as essential as the real part, for the imaginary part controls the amount of amplification (gain) or absorption (loss) in a system. The design of standard optical devices is usually on either the gain part or the loss part, but not both simultaneously. In the field of plasmonics and optical metamaterials, loss is a serious bottleneck despite the many beautiful physics demonstrated. One promising way to compensate the loss is through the incorporation of gain medium within the lossy metamaterial system. Therefore, one expects the interplay between the gain and loss medium to play an enormous role in extending the limits of optical metamaterials. In this chapter, I show that by carefully engineering both the gain and loss parts within a single system, very unique optical properties can be attained.

In quantum mechanics, it is believed that a Hamiltonian must be Hermitian in order to ensure the real energy eigenvalues and unitary time evolution [1,2]. However, recent theories revealed that physical systems with specifically designed non-Hermitian Hamiltonians can also show entirely real eigen spectra and the corresponding unitary dynamics, exhibiting a combined PT symmetry where both the individual parity P and time reversal T symmetries are broken [3,4]. Due to the mathematical similarity between the time-dependent Schrodinger equation and the paraxial equation of diffraction (Fig. 3.1), this quantum mechanics concept can also be applied in optics.

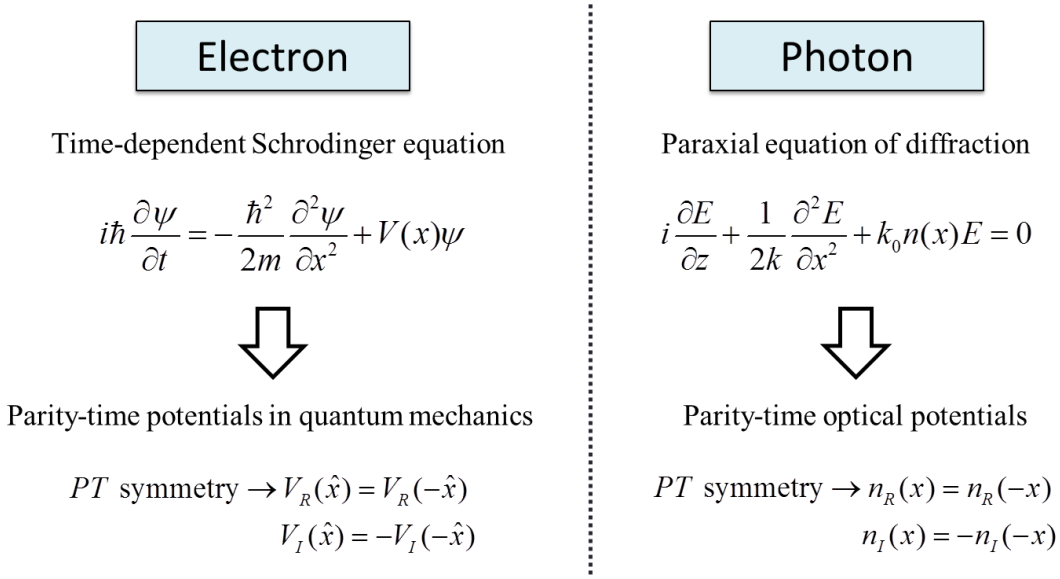

Figure 3.1 Similarity between the time-dependent Schrodinger equation and paraxial equation of diffraction allows the realization of the quantum-inspired parity-time (PT) physics in optics.

Essentially, the potentials in quantum mechanics is replaced by the optical potentials, i.e. the refractive index n. Thus, parity-time (PT) symmetry in optics requires the real part of refractive index modulation to remain symmetric $n'(x) = n'(-x)$, while the imaginary part of index becomes anti-symmetric $n''(x) = -n''(-x)$. This complex index modulation requirement is the essence of non-Hermitian optics, which enables a complex eigen-spectra solution not realizable with the conventional Hermitian optics, as shown in Fig. 3.2. In a non-Hermitian system, the Hamiltonian H should generalize the potential term to be complex [5-8]. Thus, the constant ε (not to be confused with the permittivity) in $V(x) = V_R(x) + i\varepsilon V_I(x)$ determines the imaginary contribution. Interestingly, for a non-Hermitian system, there is an associated threshold value ε_{th} beyond which the eigen-spectra cease to be real. This is attributable to the broken symmetry, rendering the wavenumber (for an optical system) to take the form of $\beta = (n' + n'')k_0$.

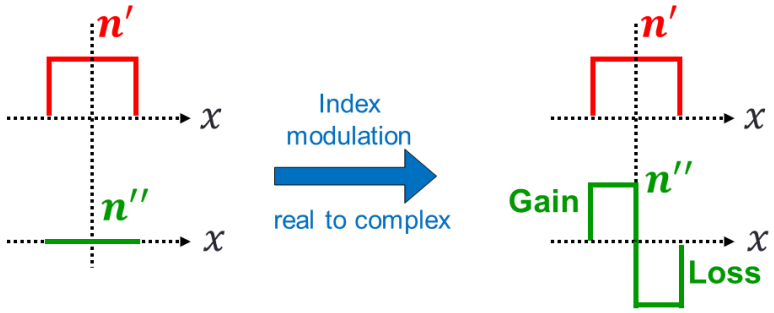

Hamiltonian $\boldsymbol{H}$	$\hat{H} = \frac{\hat{p}^2}{2m} + \hat{V}_R(\hat{x})$	$\hat{H} = \frac{\hat{p}^2}{2m} + \hat{V}_R(\hat{x}) + i\varepsilon\hat{V}_I(\hat{x})$	
Wavenumber $\boldsymbol{\beta}$	**Symmetry Conserved: Real spectra** $\boldsymbol{\beta = n'k_0}$	if $\varepsilon < \varepsilon_{th}$ **Symmetry Conserved: Real spectra** $\boldsymbol{\beta = n'k_0}$	if $\varepsilon > \varepsilon_{th}$ **Symmetry Broken: Complex spectra** $\boldsymbol{\beta = (n' + n'')k_0}$

Figure 3.2 The difference between Hermitian and Non-Hermitian optics. Parity-time (PT) symmetry requires a complex index modulation, i.e. a symmetric real part of index, and an anti-symmetric imaginary part of index. It is non-Hermitian, with a broken symmetry physics resulting in a complex wavenumber when a threshold value ε_{th} is exceeded.

A better way to understand the PT physics in optics is to look at the corresponding field distribution and the eigen-spectra plot in Fig. 3.3. As previously discussed, PT symmetry leads to a transition from a purely real eigen-solution to a complex eigen-solution. This transition point is better known as the exceptional point, with a corresponding PT threshold. As the introduced gain or loss n'' (henceforth named as gain-loss modulation) is increased, bifurcation of β'' takes place once the gain/loss contrast exceeds the PT threshold, and results in the two different PT phases. Here we consider a system with two parallel waveguides consisting of gain and loss materials satisfying the PT symmetry condition $n(x) = n^*(-x)$. In the PT symmetric phase, the electric

fields are equally distributed between the gain and loss waveguides forming a supermode. Therefore, there is no net gain or loss, resulting in a purely real wavenumber β. In the PT broken phase, the electric fields are mainly confined either in the gain or loss waveguide, yielding an effective gain/loss of the system, and thus an imaginary β. Interestingly, while the eigen-frequency is degenerate throughout the PT broken phase, the increase of gain/loss contrast can counterintuitively squeeze the field into the gain region and lead to more effective gain of the system.

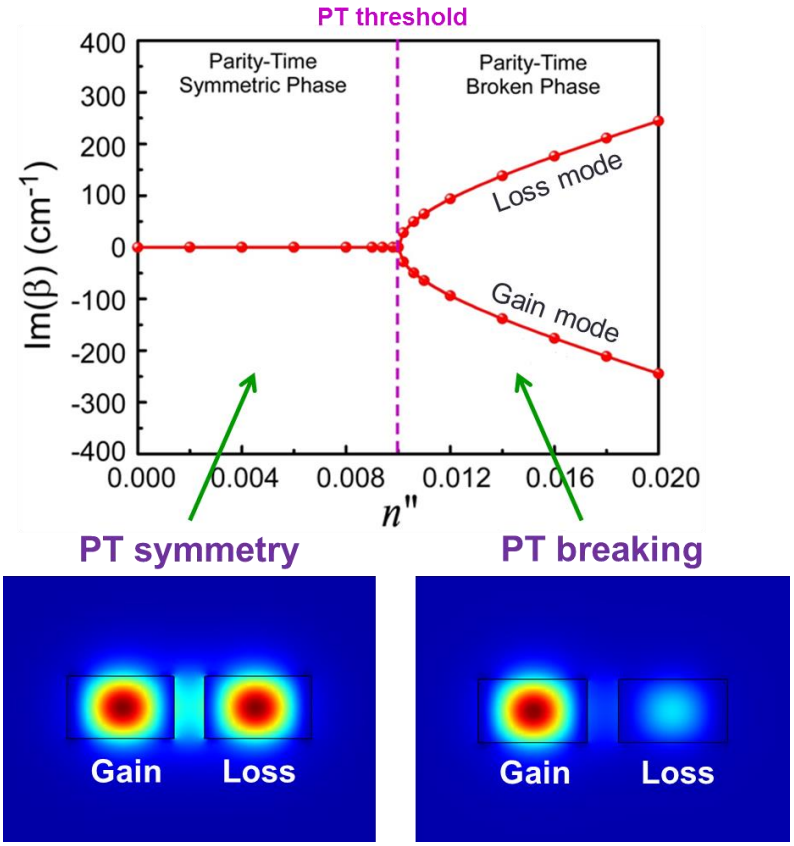

Figure 3.3 Parity-time (PT) symmetry results in two different phases in the complex eigen-spectra: (Left) PT symmetric phase where the electric field is equally distributed between the gain and loss sections, resulting in a zero effective gain/loss. (Right) PT broken phase where the electric field is confined either in the gain region or the loss region, thus lead to either a gain mode or a loss mode. The condition where bifurcation starts to take place in the complex eigen-spectra is known as the exceptional point, and the corresponding imaginary index n'' is the PT breaking threshold. The plots used here are purely for illustrative purpose.

PT symmetry has thus opened a new paradigm for non-Hermitian optics, where optical systems with deliberately designed gain and loss are used to manipulate light transport for information processing. The first observation of PT symmetry in optics is experimentally realized in 2010 using a coupled Fe-doped $LiNO_3$ waveguide system [8]. But even prior to that, there were a couple of seminal theoretical works predicting the interesting properties attainable with the PT physics [6,9,10]. In practice, fabricating carefully-engineered gain and loss structures can be challenging. Guo [11] however showed that a loss-only system could still possess the PT phase

transition eigen-spectra (except with an average loss background), and experimentally demonstrated the counterintuitive increase of transmission with loss. In 2011, another important breakthrough is reported, where a PT index modulation in the longitudinal propagation direction is shown to exhibit unidirectional invisibility [12]. Since then, many unique unidirectional light transport phenomena based on PT physics were experimentally realized [6,8-16]. In addition, PT symmetry offers a new strategy to utilize loss to control gain and its optical properties, deliberately manipulating resonant modes in laser cavities [17,18] and broadening the laser physics [19-21].

3.2 PT Single-Mode Laser

Laser cavities support a large number of closely spaced modes because their dimensions are typically much larger than an optical wavelength. As a result, the outputs from such lasers are subject to random fluctuations and instabilities because of mode competition for limited gain. Over the last decades, effective mode manipulation and selection strategies have been intensively explored to achieve single-mode operation with desired spatial and spectral controllability. This is critical to enhance laser performance for higher monochromaticity, less mode competition, and better beam quality. It is therefore important to create sufficiently modulated gain and loss to obtain single-mode operation, but factors such as inhomogeneous gain saturation makes it a challenging task. Several approaches have been developed, for example, by providing the intra-cavity feedback with an additional cavity [22], by distributed feedback gratings [23], by enlarging the free spectral range through mode size reduction [24,25], and by spatially varied optical pumping [26]. Nevertheless these approaches are only applicable to specific configurations; a general design concept is thus desired with unprecedented control of cavity modes.

Using the PT symmetry breaking concept, we delicately manipulate the gain and loss of a microring resonator and demonstrate single-mode laser oscillation of a whispering-gallery-mode (WGM). We exploit the continuous rotational symmetry of the microring structure to facilitate unique thresholdless PT breaking. This thresholdless PT breaking is only valid for the desired WGM order and enables two energy-degenerate modes: the non-oscillating loss mode and the other oscillating gain mode; whereas all other WGM modes experience balanced gain/loss modulation and thus stay below lasing threshold, leading to a single mode lasing.

The PT-synthetic microring resonator is designed with 500 nm-thick InGaAsP multiple quantum wells (MQWs) on an InP substrate (Fig. 3.4). InGaAsP MQWs have a high material gain coefficient over 1000 cm^{-1} around 1500 nm [27]. The gain/loss modulation, satisfying an exact PT symmetry operation, is periodically introduced using additional Chromium (Cr)/ Germanium (Ge) structures on top of the InGaAsP MQW along the azimuthal direction (φ):

$$\Delta n = \begin{cases} n_{gain} = -in'' & (l\pi/m < \varphi < (l+1/2)\pi/m) \\ n_{loss} = in'' & ((l+1/2)\pi/m < \varphi < (l+1)\pi/m) \end{cases} \tag{3.1}$$

where $n"$ denotes the index modulation in only the imaginary part, and m is the azimuthal order of the desired WGM in the microring and $l = 0,\ 1,\ 2\ ...\ 2m-1$ divides the microring into $2m$ periods (i.e. $4m$ sections of gain and loss in total). The PT modulation is designed using bilayers on top of the gain material that introduces loss and exactly reverses the sign of the imaginary part of the local modal index, while maintaining the same real part (in practice, the deposition of Cr/Ge also slightly modifies the real part on the order of 0.01%).

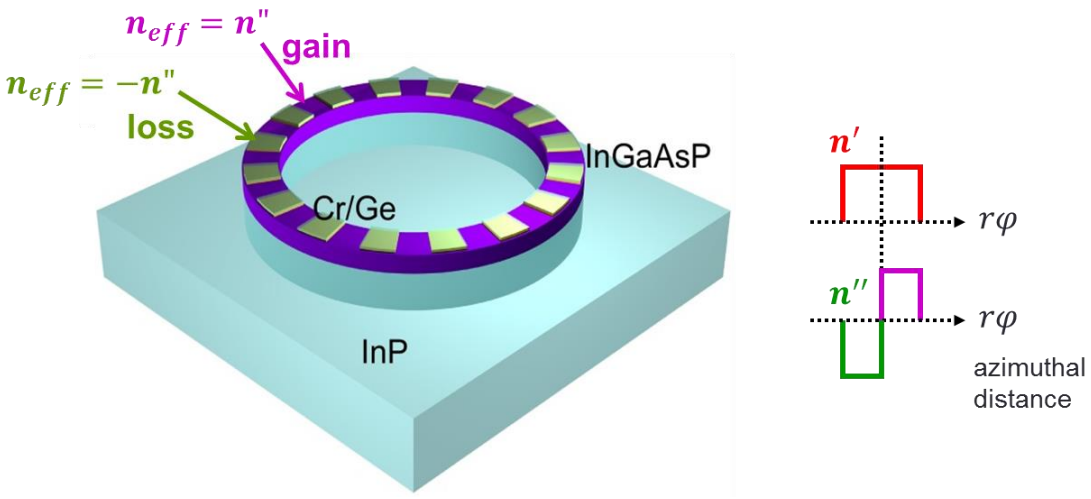

Figure 3.4 Schematic of the PT microring laser consists of Cr/Ge bilayer structures arranged periodically in the azimuthal direction on top of the InGaAsP/InP microring resonator to mimic a pure gain-loss modulation. The diameter of the microring resonator is 8.9 μm and the width of the microring resonator is 900 nm. The microring also extends 1 μm-deeper into the InP substrate. Here, the designed azimuthal order is $m = 53$ to achieve the resonant wavelength around 1500 nm.

Because of the PT modulation, the coupled mode equations for a standard microring resonator have to be modified. Assuming a small variation of index change and negligible scattering loss in the PT microring resonator, the coupled mode equations can be written as

$$\begin{cases} \dfrac{dA}{Rd\varphi} = i\beta_0 A + in"\kappa B \\ \dfrac{dB}{Rd\varphi} = i\beta_0 B - in"\kappa A \end{cases} \tag{3.2}$$

where β_0 is the intrinsic wavenumber of the WGM without gain and loss and κ denotes the coupling between the clockwise and counter-clockwise traveling waves through PT modulation in the microring resonator. By solving the coupled mode equations, the eigen wavenumbers of the WGMs supported in the microring resonator can be obtained as [28]

$$\beta = \beta_0 \pm i\kappa n" \tag{3.3}$$

manifesting non-threshold PT symmetry breaking in our PT microring lasers. This thresholdless condition is robust against the nonlinearity during the pump process. For example, the real part

index change by the optical nonlinear effects [29] only affects β_0 in Eq. (3.3). However, with any arbitrary values for β_0, the bifurcation in the imaginary part of β takes place immediately and the resulted PT symmetry breaking is thresholdless with respect to n''.

Evolution of PT symmetry of the $m = 53$ WGM in the microring resonator as a function of imaginary part index modulation can be seen from the corresponding complex eigen-spectra (Fig. 3.5). Two WGMs are energy degenerate at the same eigen resonant frequency, but their modal wavenumbers are complex conjugates of each other, corresponding to PT symmetry breaking with a simultaneous coexistence of lasing and absorption eigen-modes. More interestingly, the microring resonator goes into the PT broken phase with a bifurcation in the imaginary spectrum even if the strength of gain-loss modulation is infinitesimal. This thresholdless feature in our PT phase transition owes to the continuous rotational symmetry associated with the desired WGM order in the absence of a real index modulation. This feature is unique compared to the previously studied coupled PT waveguide systems including the recently developed coupled gain/loss WGM resonators [15,19]. In those systems, there are no continuous symmetries, such that PT symmetry breaking requires a finite strength of the gain-loss modulation [30]. Although our design is based on a linear model by assuming a steady lasing state with a certain gain coefficient of InGaAsP, it is worth noting that lasing itself is an intrinsic nonlinear process. However, this thresholdless PT breaking in our system is robust against optical nonlinearity and its induced PT phase transition [29].

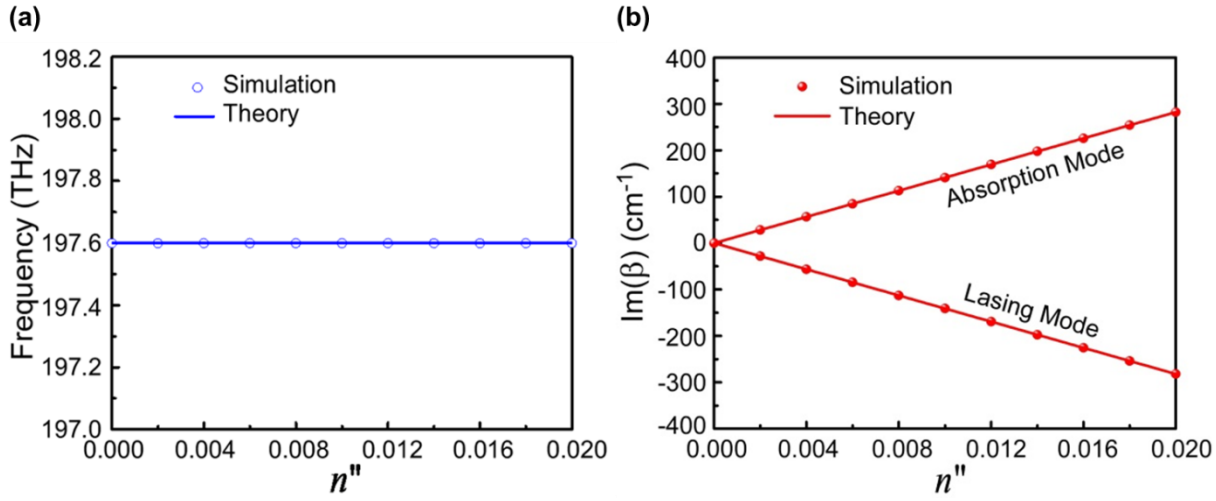

Figure 3.5 (a) and (b) show the same eigen frequency (197.6 THz) and complex conjugate imaginary eigen spectra for the two modes at $m = 53$ determined by numerical simulations (circles/dots) and theoretical calculations (solid lines). The onset in (c) indicates thresholdless PT symmetry breaking.

In the experiment, a slight deviation from the desired perfectly balanced gain/loss modulation is possible. However, the thresholdless PT breaking in our system is robust even if the introduced PT modulation is of unbalanced gain and loss as follows,

$$\Delta n = \begin{cases} n_{gain} = -in"(1-\delta) & (l\pi/m < \varphi < (l+1/2)\pi/m) \\ n_{loss} = in" & ((l+1/2)\pi/m < \varphi < (l+1)\pi/m) \end{cases} \tag{3.4}$$

where δ is the introduced factor denoting the difference between the gain and loss strengths. In this case, the coupled mode equations for the desired WGM order can be written as

$$\begin{cases} \dfrac{dA}{Rd\varphi} = i\left(\beta_0 - i\dfrac{\pi\delta}{4}n"\kappa\right)A + i\left(n" - \dfrac{\delta}{2}n"\right)\kappa B \\ \dfrac{dB}{Rd\varphi} = i\left(\beta_0 - i\dfrac{\pi\delta}{4}n"\kappa\right)B + i\left(-n" + \dfrac{\delta}{2}n"\right)\kappa A \end{cases}. \tag{3.5}$$

The two eigen wavenumbers of the supported WGMs can then be obtained as

$$\beta = \beta_0 + i\kappa\frac{\pi\delta}{4}n" \pm i\kappa\left(n" - \frac{\delta}{2}n"\right). \tag{3.6}$$

Evolution of PT symmetry as a function of $n"$ according to Eq. (3.6) can be seen in Fig. 3.6 for a reasonable assumption of $\delta = 0.1$. The complex eigen-spectra clearly show thresholdless PT breaking is maintained, but modal gain and loss coefficients are slightly different as $\mathrm{Im}(\beta_1) = -0.8715\kappa n"$ and $\mathrm{Im}(\beta_2) = 1.0285\kappa n"$, respectively.

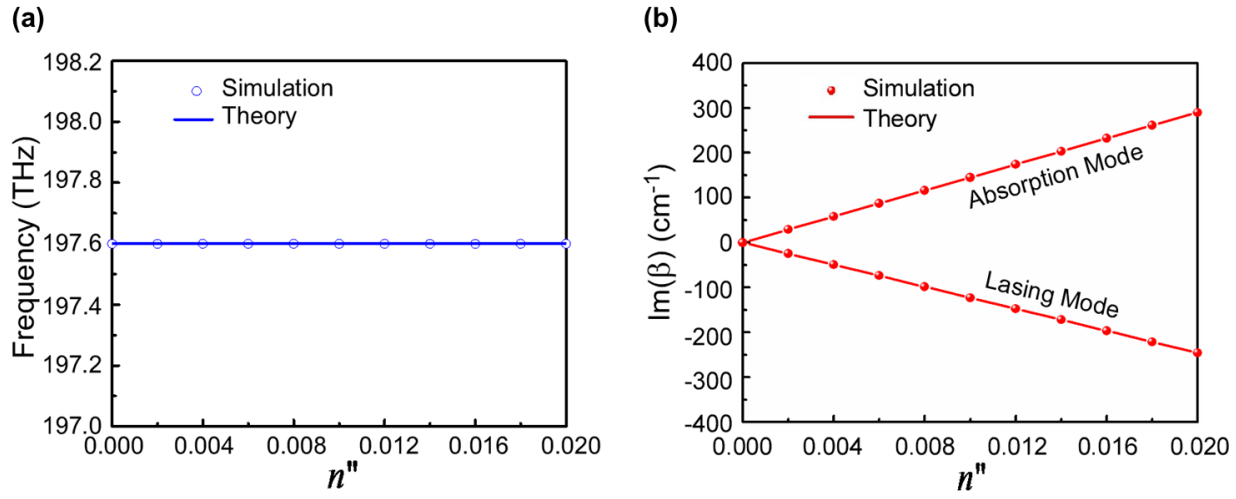

Figure 3.6 PT phase transition in an imbalanced gain/loss modulated microring resonator. (a) and (b) are the real and imaginary eigen-spectra for $m = 53$ by numerical simulations (circles/dots) and analytical calculations (solid lines), respectively.

In reality, the fabricated device might not ideally reach perfect gain and loss balance. However, it can still be treated as a gain/loss balanced PT system after averaging out the system loss [14]. With an additional attenuation term α/π representing the average loss, at the steady lasing state, the introduced gain/loss modulation can be written as

$$\Delta n = \begin{cases} n_{gain} = -i\frac{\alpha}{2} + i\frac{\alpha}{\pi} & (l\pi/m < \varphi < (l+1/2)\pi/m) \\ n_{loss} = i\frac{\alpha}{2} + i\frac{\alpha}{\pi} & ((l+1/2)\pi/m < \varphi < (l+1)\pi/m) \end{cases} . \tag{3.7}$$

The coupled mode equations for the desired WGM order then become

$$\begin{cases} \frac{dA}{Rd\varphi} = i\beta_0 ' A + i\left(\frac{\alpha}{2}\right)\kappa B \\ \frac{dB}{Rd\varphi} = i\beta_0 ' B + i\left(-\frac{\alpha}{2}\right)\kappa A \end{cases} \tag{3.8}$$

where $\beta_0 ' = \beta_0 + i\frac{\alpha}{2}\kappa$. Thus the wavenumbers of the eigen-modes are derived as

$$\beta = \beta_0 ' \pm i\frac{\kappa\alpha}{2} . \tag{3.9}$$

Comparing Eq. (3.9) with Eq. (3.3), it clearly shows that the unbalanced gain/loss system maintains the features of the ideal gain/loss balanced PT system, supporting two energy degenerate modes with complex conjugate gain/loss coefficients after averaging the system loss with $\beta_0 '$.

Fig. 3.7 show the modal intensity distribution of the lasing and absorption modes in the PT microring resonator with 15 nm Cr and 40 nm Ge on top (corresponding to the InGaAsP MQWs material gain coefficient of 800 cm^{-1} for the presumed ideal balanced gain/loss modulation): one with electric fields confined mainly underneath the amplification sections exhibiting a net modal gain coefficient of 268 cm^{-1}, while the other is loss dominant with electric fields mainly under the Cr/Ge sections with a loss coefficient of -268 cm^{-1}. Their eigen frequencies are energy-degenerate but their gain/loss coefficients are opposite one another, consistent with the features of PT symmetry breaking. For other WGMs, for instance $m = 54$, electric fields in both energy-degenerate WGMs are uniformly distributed in gain and loss regimes. As a result, gain and loss are averaged out, creating modal wavenumbers without net gain or loss (simulations show both modes have a similarly small loss coefficient of about -8 cm^{-1}), as shown in Fig. 3.8. In this case, WGMs fall into the PT symmetric phase for the non-desired azimuthal orders. It is therefore clear that only the lasing mode at the desired order contains a positive effective gain coefficient above the lasing threshold, enabling single-mode lasing. All other WGMs are suppressed by the intentionally introduced loss from the PT modulation. This unique single-mode operation is even valid with an arbitrarily wide gain spectrum due to its stringent mode selectivity, which is inherently different from the conventional single-mode microring lasers that use the real-index coupling and modulation to achieve the mode splitting in eigen frequencies and are limited by the bandwidth of the gain media [31,32].

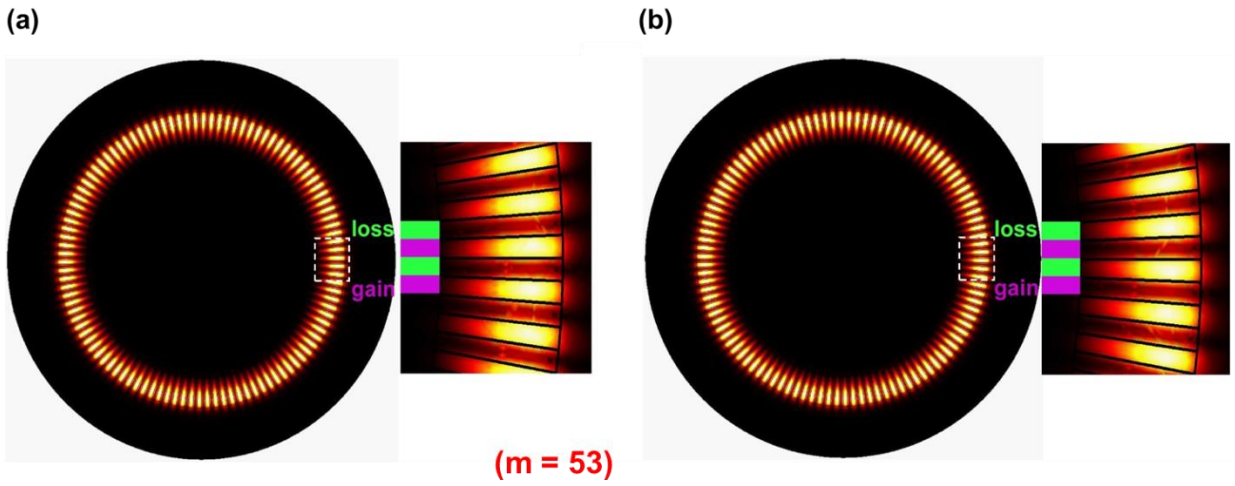

Figure 3.7 Eigen electric field intensity distributions of paired lasing (a) and absorption (b) modes for $m = 53$ at 197.6 THz. Fields are confined in the gain (a) and loss (b) sections, resulting in conjugate modal gain/loss coefficients: effective gain of 268 cm^{-1} ($\mathrm{Im}(\beta) = -134\ cm^{-1}$) for the lasing mode (a) and effective loss of -268 cm^{-1} ($\mathrm{Im}(\beta) = 134\ cm^{-1}$) for the absorption mode (b).

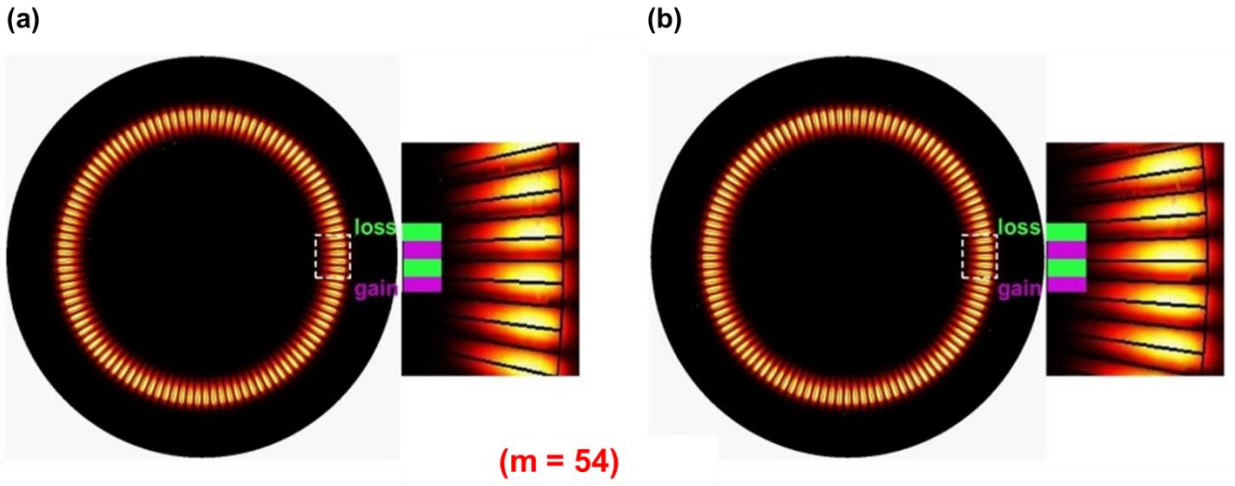

Figure 3.8 (c) and (d) show eigen electric field intensity distributions of paired WGMs at $m = 54$. The two modes share the same eigen frequency of 200.9 THz and a similar modal loss coefficient of -8 cm^{-1} ($\mathrm{Im}(\beta) = 4\ cm^{-1}$).

The PT microring laser with Cr/Ge modulations was fabricated using overlay electron beam lithography and plasma etching. The fabrication steps are illustrated in Fig. 3.9. A 500-nm-thick InGaAsP multiple-quantum-well (MQW) was first grown on an InP substrate by metal organic chemical vapor deposition (MOCVD). The PT structures and the alignment marks were then defined in a bilayer copolymer EL8/PMMA A2 resist using the electron beam lithography (EBL). This is followed by electron beam evaporation of 15 nm of Chromium (Cr) and 40nm of Germanium (Ge). We then used a shadow mask to block the PT structures area such that only the alignment mark regions were exposed where an additional 2 nm of Chromium (as adhesion layer)

and a 40 nm of gold (Au) were deposited. Gold was used to make the alignment marks for its better image contrast under the scanning electron microscope (SEM) during the subsequent EBL alignment step. Upon the lift-off process, we used a thick HSQ (FOX-15) as the negative resist for the second EBL exposure to define the microring. Upon development, the HSQ structures served as the etch mask for the 1.5-μm-deep inductively coupled plasma (ICP) etching using $Cl_2/CH_4/H_2$ gases. Finally, the mask layer was removed by soaking the sample in hydrofluoric (HF) acid solution for 1 minute. The SEM image of the fabricated sample is shown in Fig. 3.10.

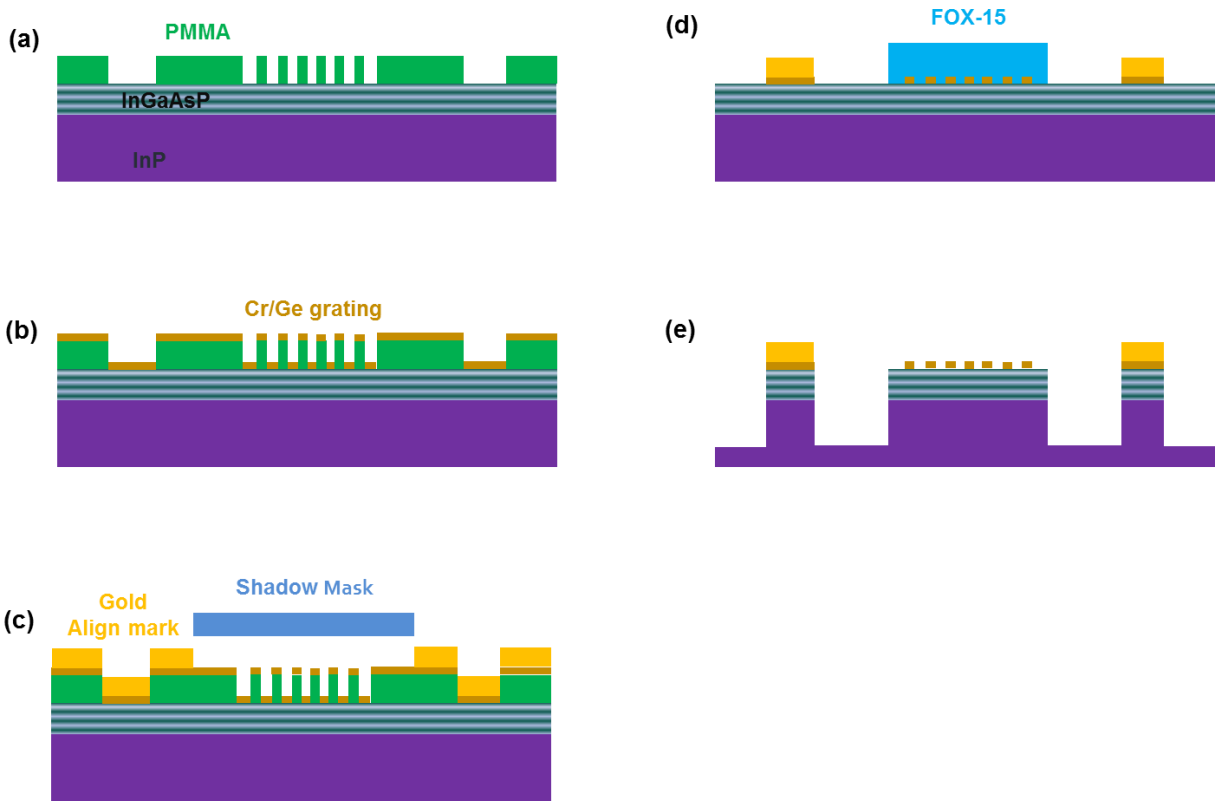

Figure 3.9 Schematic of the fabrication process. (a) EBL patterning of the PT structures and the alignment marks with a PMMA resist on a InGaAsP MQW grown on an InP substrate. (b) Electron beam evaporation of Cr/Ge layers. (c) Selective electron beam evaporation of a thick Au layer at the alignment mark positions using a shadow mask. (d) EBL patterning on a FOX-15 negative resist to define the microring. (e) Deep ICP etching followed by the removal of the masking layer.

The fabricated PT synthetic laser was optically pumped using a Ti:Sapphire pulsed laser operating at a repetition rate of 80 MHz, with the central wavelength of 890 nm, and with a pulse width of 100 fs, as illustrated in Fig. 3.11. The input pump power was adjusted using a variable neutral density (ND) filter and monitored with a power meter. A longpass dichroic mirror (50% transmission/reflection at 1180 nm) was employed to selectively reflect the pump laser but allowing the longer-wavelength emitted light to pass through. The pump beam was delivered to the device through a Mitutoyo 20× long-working distance objective (NA = 0.4) that was also used to collect the light emission. In other words, the sample was optically pumped from the top and lasing emission was also collected from the top as well. Emitted light was then coupled into

a liquid nitrogen cooled spectrometer for spectral analysis and the lasing image was captured with an InGaAs infrared CCD camera.

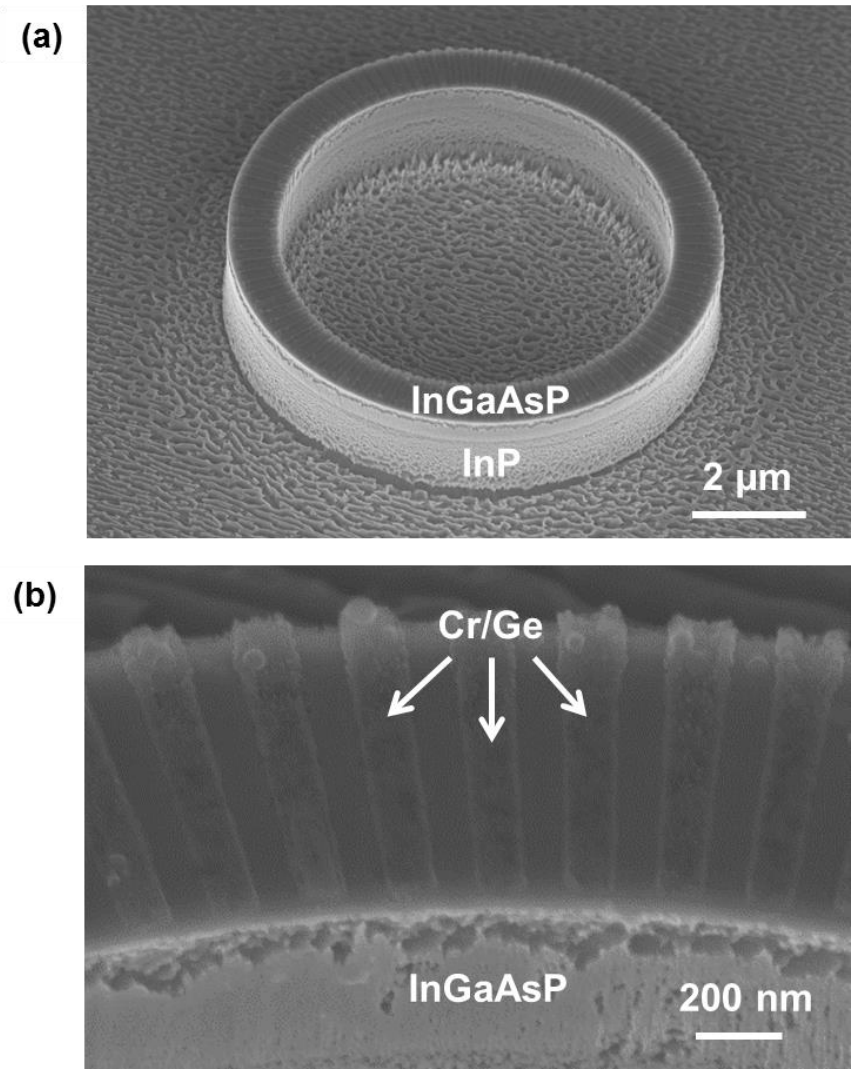

Figure 3.10 (a) Scanning electron microscope image of the fabricated PT microring laser. (b) Close-up view showing the lossy Cr/Ge PT structures on top of the InGaAsP gain medium.

Under optical pumping with the femtosecond laser, a broad photoluminescence (PL) emission around 1500 nm was first observed at low pump power densities (Fig. 3.12). As the pump power was increased, the transition to amplified spontaneous emission (ASE) and full laser oscillation was clearly observed from the rapidly increasing spectral purity of the cavity mode. At higher pumping intensities well above the lasing threshold, the single-mode peak is seen lasing at the wavelength of 1513 nm, confirming our theoretical prediction of the single WGM lasing operation of the PT microring laser. The lasing linewidth is about 1.7 nm around the transparency pump power, corresponding to a quality factor of about 890 that is limited by the surface roughness of the sample.

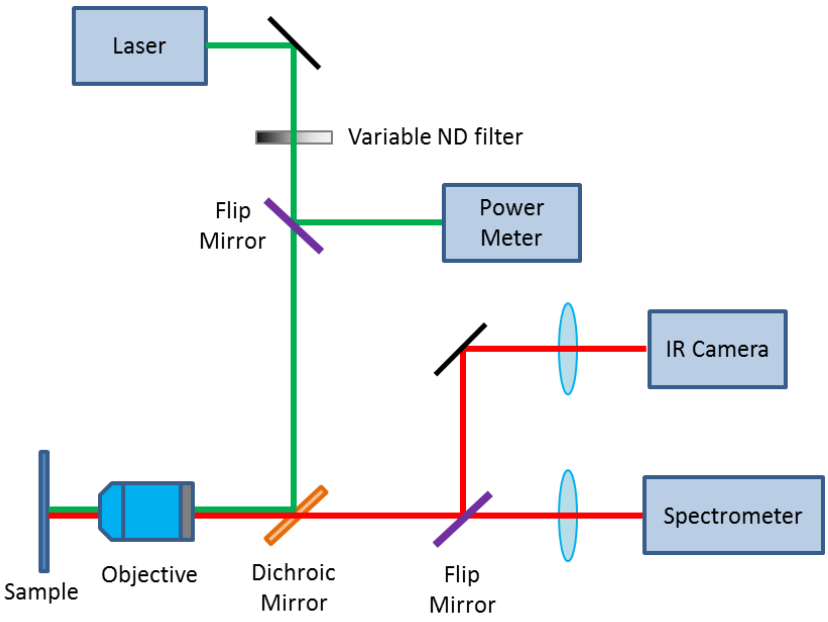

Figure 3.11 Measurement setup to characterize the PT microring laser.

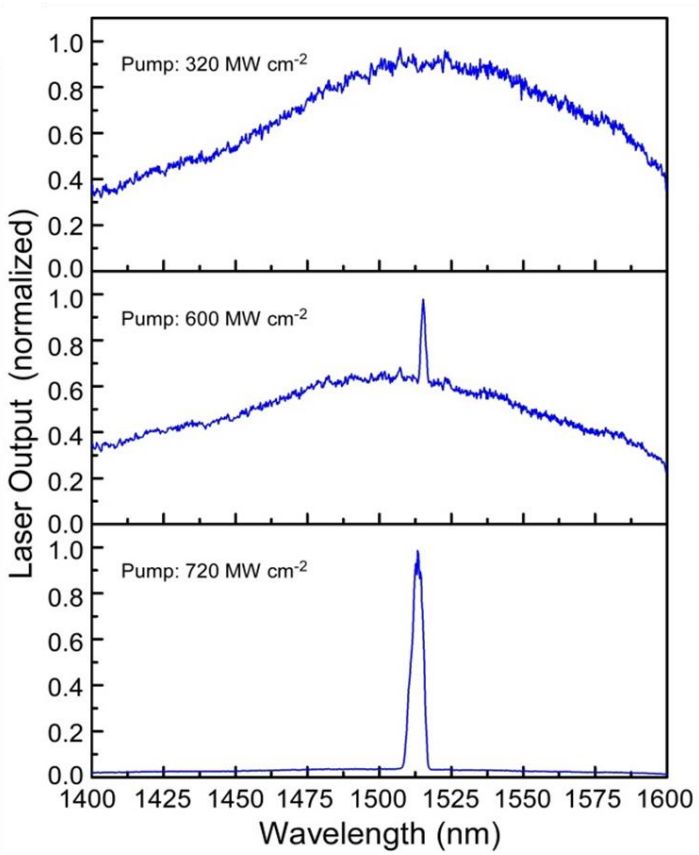

Figure 3.12 Evolution of the light emission spectrum from PL, to ASE, and to single-mode lasing at the wavelength of about 1513 nm, shown as the peak power density of pump light was increased from 320 MW cm^{-2}, 600 MW cm^{-2}, to 720 MW cm^{-2}, respectively.

In Fig. 3.13, the light-light curve corresponding to single-mode emission clearly shows a slope change corresponding to a lasing threshold at peak pump power density of about 600 MW cm^{-2}. While the lasing mode ($m = 53$) in the PT broken phase emerges above the lasing threshold, creating well-pronounced single-mode lasing with an extinction ratio of more than 14 dB, other WGMs are all below the lasing threshold and are strongly suppressed.

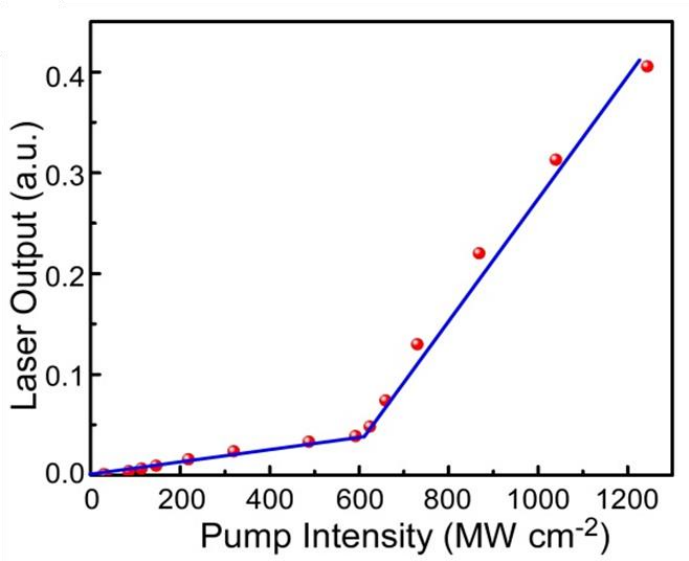

Figure 3.13 Light-light curve of the PT microring laser shows the power relationship between the lasing emission and the pump light. A clear onset of the intrinsic single-mode lasing appears at threshold slightly larger than 600 MW cm^{-2}.

For comparison, a control sample of a WGM laser was fabricated consisting of the same-sized InGaAsP/InP microring resonator without additional Cr/Ge index modulation. As expected, we observed a typical multimode lasing spectrum with different WGM azimuthal orders distributed over the gain spectral region (Fig. 3.14a). Compared to the PT microring laser, it can be seen that under a similar pumping condition, the resonance peak for the same azimuthal order of $m = 53$ well matches the single-mode lasing of PT ring resonator at the wavelength of 1513 nm (Fig. 3.14b). The power efficiency and the lasing threshold are also similar because the introduced loss in the PT microring laser minimally affects the desired lasing mode. Moreover, we also fabricated an additional PT microring laser with a different azimuthal PT modulation for the order of $m = 55$. Its lasing emission at 1467 nm (Fig. 3.14b) also agrees well with the multimode lasing spectrum of the conventional WGM laser for the same azimuthal order (Fig. 3.14a). It is evident that instead of altering the WGM in the microring resonator, the introduced PT gain/loss modulation selects the lasing WGM in the PT broken phase over a broad band of spectrum. By changing the desired azimuthal order of the structured PT modulation, the single-mode lasing frequency can be efficiently selected. Although we only demonstrated lasing for two WGM orders, this mode selection concept is general and in principle valid for arbitrary gain spectra. In applications, the demonstrated stable single-mode lasing can be efficiently routed, using a bus waveguide through the evanescent ring-waveguide coupling, to photonic integrated circuits for on-chip signal amplification and processing.

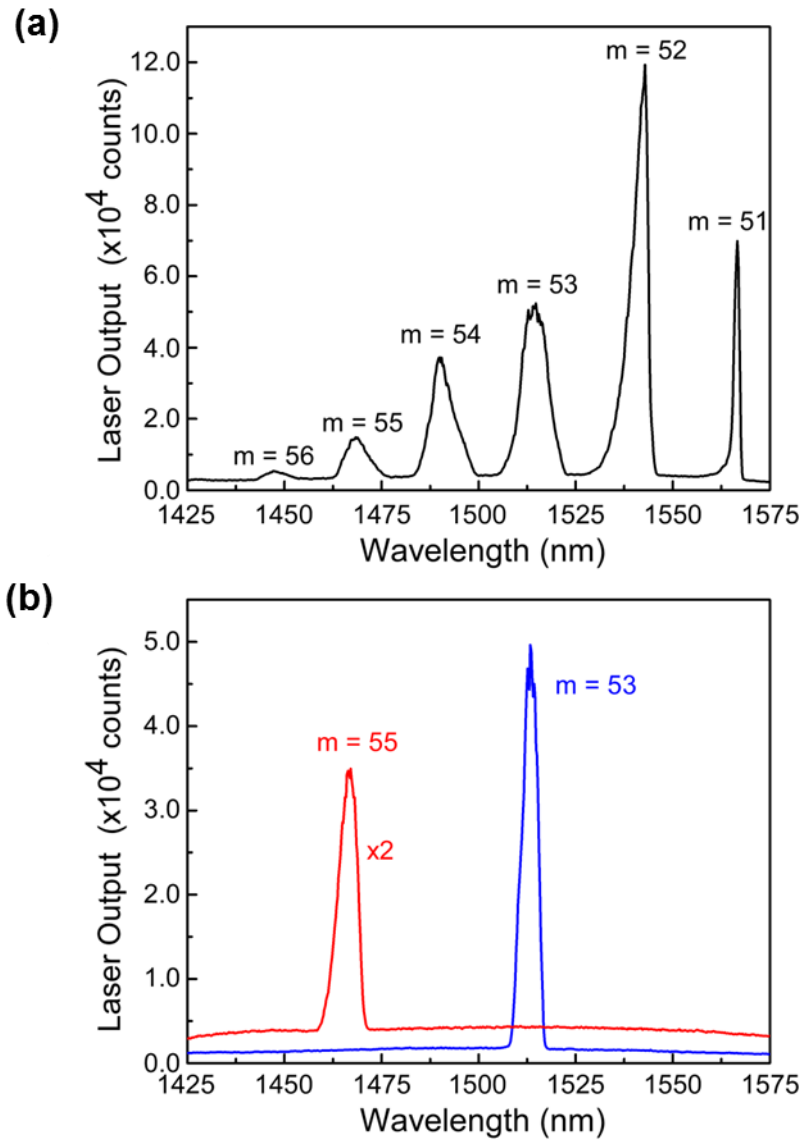

Figure 3.14 Comparison between PT laser and typical microring laser. (a) Multimode lasing spectrum observed from the typical microring WGM laser, showing a series of lasing modes corresponding to different azimuthal orders. (b) Single-mode lasing spectra of the PT microring lasers operating at the $m = 53$ and $m = 55$ azimuthal orders, consistent with the lasing wavelength for the same azimuthal orders in (a). This confirms that our PT microring laser does not alter original WGMs but efficiently select the desired lasing mode.

We have demonstrated a PT microring laser by delicate exploitation of optical loss and gain. Such a microring laser is intrinsically single-mode regardless of the gain spectral bandwidth. This is because the continuous rotational symmetry of PT modulation enables the thresholdless PT breaking only for the desired mode. More importantly, our PT laser demonstration is a major step towards unique photonic devices such as a PT symmetric laser-absorber that coincides lasing and anti-lasing, i.e. coherent perfect absorption [33,34] simultaneously.

3.3 PT Coherent Optical Amplifier-Absorber

Power loss by optical absorption is a serious problem in optics, significantly degrading the performance and efficiency of optical devices such as microscopes and fiber networks. Oppositely, optical gain, attained through external pumping, has been invested in light amplification that overcomes the undesirable absorption [35,36], leading to the birth of lasers. A laser distinguishes itself from other light sources for its intrinsic coherence in both space and time. The time-reversed counterpart of laser emission enables coherent perfect absorption in a loss-dominant resonator, facilitating the emergence of anti-laser. An anti-laser (or coherent perfect absorber) based on interferometric control of absorption is shown to completely annihilate both the transmitted and reflected light signals [33,34], promising novel applications in enhanced nano-optical mode coupling [37], ultrathin perfect absorbers [38,39], and integrated photonic circuits [40]. While both the laser and anti-laser are individually of important functionalities to advance the current optics and photonics technology, simultaneous lasing and anti-lasing is deemed impossible since the conventional laser physics requires either gain or loss, respectively, but not both. Therefore, unique synergy of simultaneous lasing and anti-lasing is very difficult to achieve, which, however, can revolutionize optical applications if realized. For example, while many light modulation and switching schemes have been proposed relying on either linear or nonlinear light controls [41-44], significant challenges remain to effectively approach the ultimate modulation depth, a key figure-of-merit to assess the performance of optical modulators, set by the maximum contrast between the lasing and anti-lasing states [45,46]. The state-of-the-art modulation depth is still orders of magnitude lower than the ultimately attainable limit. Recent theoretical proposals [30,45] suggested that a delicate interplay between gain and loss may resonantly realize simultaneous lasing and anti-lasing using the concept of parity-time (PT) symmetry.

Here the simultaneous lasing and anti-lasing condition is derived for a waveguide system with balanced PT gain/loss modulation along the propagation direction of z, where the coupled mode equations can be written as

$$\begin{cases} \dfrac{dA(z)}{dz} = -i\kappa B(z) \\ \dfrac{dB(z)}{dz} = -i\kappa A(z) \end{cases} \tag{3.10}$$

where the coupling coefficient between the forward amplitude $A(z)$ and backward amplitude $B(z)$ is $\kappa = \dfrac{2n''}{\pi} k_0$. The amplitudes of the forward and backward propagating waves at both ends of the optical system ($z = 0$ and $z = L$) are related through the 2 × 2 transfer matrix M as follows,

$$\begin{pmatrix} A(L) \\ B(L) \end{pmatrix} = \begin{pmatrix} M_{11} & M_{12} \\ M_{21} & M_{22} \end{pmatrix} \begin{pmatrix} A(0) \\ B(0) \end{pmatrix}. \tag{3.11}$$

Solving the coupled mode equations will lead to $M_{11}=M_{22}=\cos(\kappa L)$, and $M_{12}=M_{21}=-i\sin(\kappa L)$. Therefore, in this unique PT-symmetric system, both the lasing ($M_{22}=0$) and anti-lasing ($M_{11}=0$) conditions can be satisfied simultaneously by equating $\cos(\kappa L)=0$. This is in stark contrast with conventional non-PT optical systems where M_{11} and M_{22} cannot both become 0 at the same frequency. For the design in an experiment, a device length of $L=\dfrac{\pi}{2\kappa}$ can be used.

In reality, a slight deviation of the mode index from the perfectly balanced PT gain-loss modulation is possible. Considering both the real and imaginary part of index deviation from the design, the gain-loss modulation can be written as

$$\Delta n=\begin{cases} n_{gain}=-in''+\Delta n_{\mathrm{Re}}^{(1)}+i\Delta n_{\mathrm{Im}}^{(1)} & 0<z<a/2 \\ n_{loss}=in''+\Delta n_{\mathrm{Re}}^{(2)}+i\Delta n_{\mathrm{Im}}^{(2)} & a/2<z<a \end{cases}. \tag{3.12}$$

where $\Delta n_{\mathrm{Re}}^{(1)}$, $\Delta n_{\mathrm{Im}}^{(1)}$ and $\Delta n_{\mathrm{Re}}^{(2)}$, $\Delta n_{\mathrm{Im}}^{(2)}$ are the real and imaginary index deviation for the gain and loss modulation, respectively. In addition, to obtain the spectral dependence for coherent amplification and absorption, a frequency detuning term $\Delta k=k-k_0$ is added to the coupled mode equations:

$$\begin{cases} \dfrac{dA(z)}{dz}=i\theta A(z)-i\kappa B(z)\,\mathrm{e}^{-i2\Delta kz} \\ \dfrac{dB(z)}{dz}=-i\theta B(z)-i\kappa A(z)\,\mathrm{e}^{i2\Delta kz} \end{cases}. \tag{3.13}$$

where the coupling coefficient between the forward amplitude and backward amplitude is now given by $\kappa=\dfrac{2n''}{\pi}-\dfrac{i}{\pi}\left[\left(\Delta n_{\mathrm{Re}}^{(2)}-\Delta n_{\mathrm{Re}}^{(1)}\right)+i\left(\Delta n_{\mathrm{Im}}^{(2)}-\Delta n_{\mathrm{Im}}^{(1)}\right)\right]$, while the self-coupling coefficient is $\theta=\left[\left(\Delta n_{\mathrm{Re}}^{(2)}+\Delta n_{\mathrm{Re}}^{(1)}\right)+i\left(\Delta n_{\mathrm{Im}}^{(2)}+\Delta n_{\mathrm{Im}}^{(1)}\right)\right]/2$.

The transfer matrix *M* that relates the complex amplitudes at two ends $z=0$ and $z=L$ is

$$\begin{pmatrix} A(L) \\ B(L) \end{pmatrix}=\begin{pmatrix} M_{11} & M_{12} \\ M_{21} & M_{22} \end{pmatrix}\begin{pmatrix} A(0) \\ B(0) \end{pmatrix}. \tag{3.14}$$

Solving the coupled mode equations above will now yield a more general transfer matrix *M* of

$$\begin{pmatrix} M_{11} & M_{12} \\ M_{21} & M_{22} \end{pmatrix} = \begin{pmatrix} \left(\cos(\gamma L) + i\frac{\theta+\Delta k}{\gamma}\sin(\gamma L)\right)e^{-i\Delta kL} & -\frac{i\kappa}{\gamma}\sin(\gamma L)e^{-i\Delta kL} \\ -\frac{i\kappa}{\gamma}\sin(\gamma L)e^{i\Delta kL} & \left(\cos(\gamma L) - i\frac{\theta+\Delta k}{\gamma}\sin(\gamma L)\right)e^{i\Delta kL} \end{pmatrix} \quad (3.15)$$

where $\gamma = \sqrt{\kappa^2 + (\theta + \Delta k)^2}$.

As a cross-check, for the ideal PT-symmetric device ($\Delta n_{\mathrm{Re}}^{(1)} = \Delta n_{\mathrm{Re}}^{(2)} = 0, \Delta n_{\mathrm{Im}}^{(1)} = \Delta n_{\mathrm{Im}}^{(2)} = 0$), the components of the transfer matrix M shall obey the relation $M_{22} = M_{11}^{*}$ which means $real(M_{22}) = real(M_{11})$ and $imag(M_{22}) = -imag(M_{11})$. This can be seen in Fig. 3.15, where the lasing and anti-lasing conditions $M_{11} = M_{22} = 0$ are both satisfied at a designed wavelength close to 1540 nm.

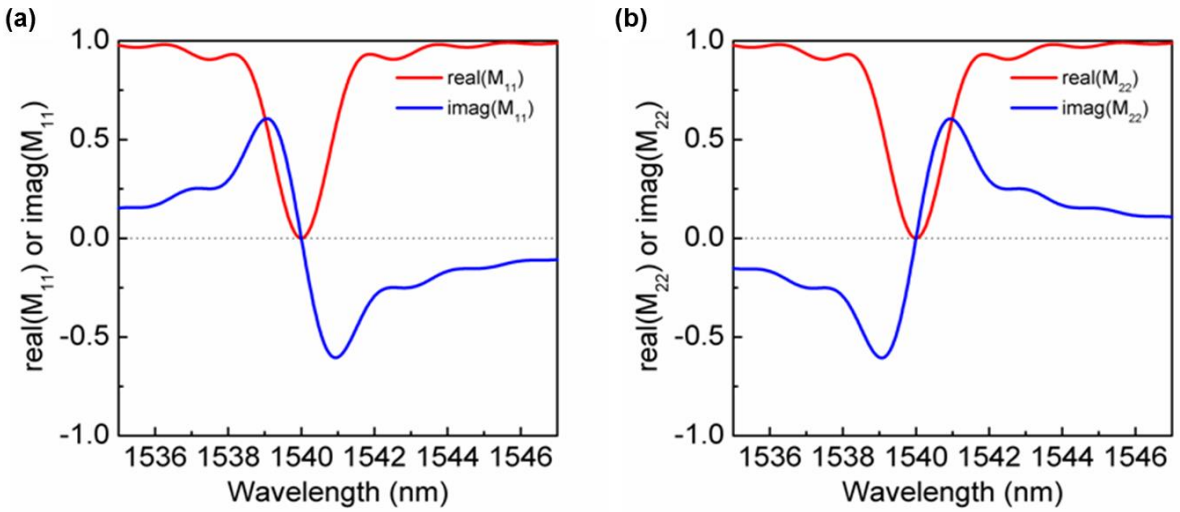

Figure 3.15 M_{11} and M_{22} for the perfectly balanced PT modulation. (a) Real and imaginary values of M_{11} versus wavelength (b) Real and imaginary values of M_{22} versus wavelength. $M_{11} = M_{22} = 0$ is uniquely satisfied at around 1540 nm, where both lasing and anti-lasing resonances can take place.

Here, we demonstrate a coherent optical amplifier-absorber (COAA), where gain and loss are deliberately exploited using the concept of PT symmetry, to approach the ultimate modulation contrast by interferometrically switching photons between lasing and anti-lasing states. An illustration of the proposed structure and working principle is shown in Fig. 3.16. The optical feedback by the deliberately designed PT symmetric modulation in the COAA simultaneously supports two degenerate lasing and anti-lasing modes with complex conjugate gain and loss coefficients. These two eigen-modes are spatially shifted by half the Bragg wavelength, with an offset of π in phase. The phase offset between incoming light beams shifts the constructive interference from one to the other, showing a great modulation contrast between coherent lasing/amplification and anti-lasing/perfect absorption. The synergy of simultaneous lasing and anti-lasing is critical to accomplish large modulation depth with high signal-to-noise ratio.

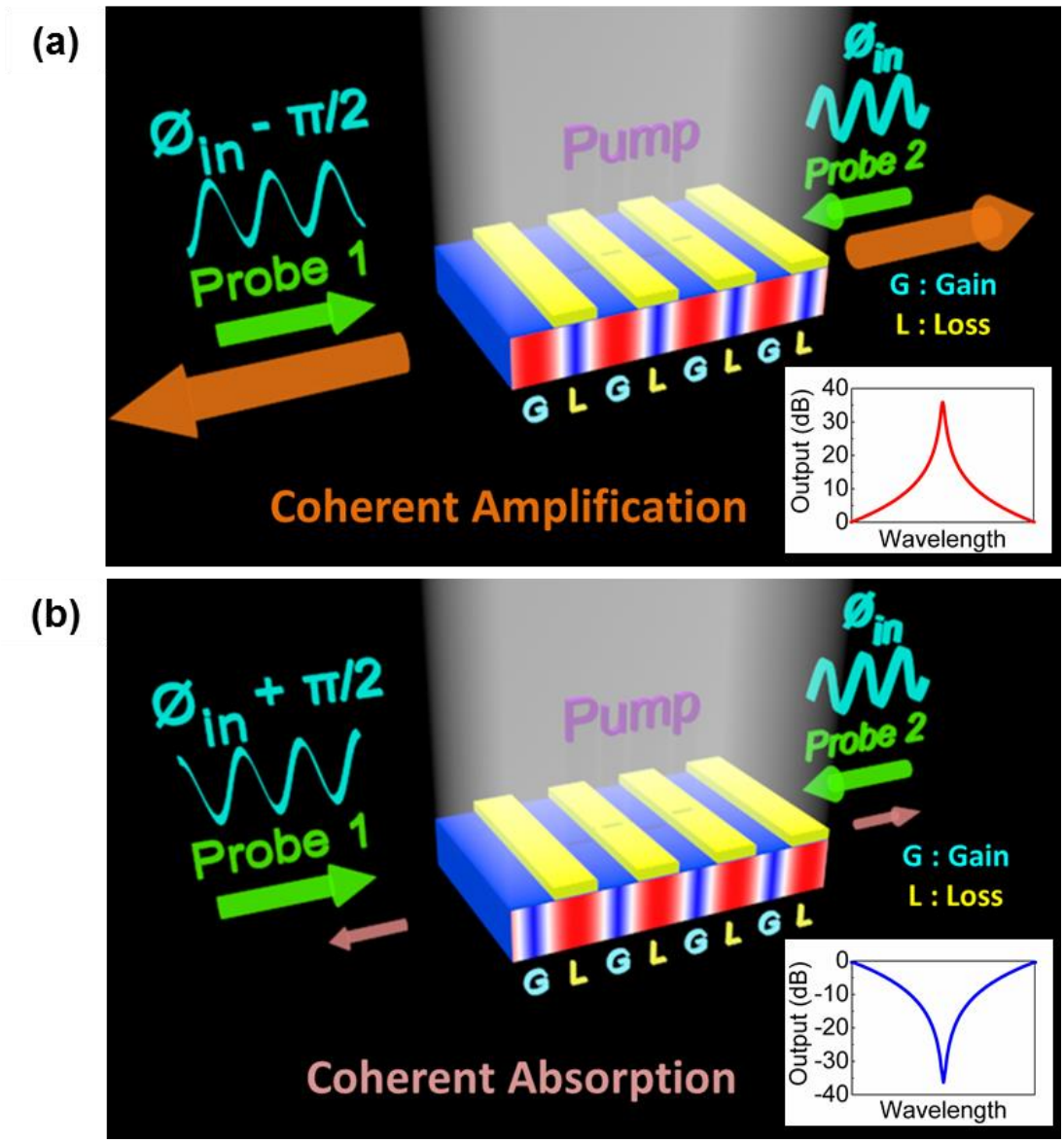

Figure 3.16 A coherent optical amplifier-absorber (COAA). (a) and (b) show the principle of the COAA device, where the pure gain/loss PT modulation is introduced by placing periodic loss structures on a semiconductor InGaAsP/InP gain waveguide. The period of the PT modulation is designed to be half the effective wavelength of guided light, corresponding to the Bragg resonant condition at the wavelength of 1540 nm. By uniformly pumping the device, the balanced gain/loss PT symmetry condition is satisfied to attain both lasing and anti-lasing eigenmodes in this single COAA device. The coherent interferometric phase control on the guided light incoming from both directions can selectively excite either the lasing mode or the anti-lasing mode. (a) When the incoming probe beams are $-\pi/2$ offset in phase, the Bragg resonant electric fields constructively interfere only in the gain regions, which leads to strongly amplified outgoing waves and a sharp peak in the output spectrum corresponding to strong amplification by the lasing mode. (b) When the incoming probe beams are $\pi/2$ offset in phase, the device falls in the anti-lasing mode, where the Bragg interference of electric fields is strongly confined only in the loss regions, causing strong absorption and a narrow dip in the output spectrum.

The COAA is designed using a straight waveguide of 500 nm-thick InGaAsP multiple quantum wells (MQWs) as a gain medium on an InP substrate. The alternating PT symmetric gain-loss modulation is introduced by periodically placing thin absorbing Cr/Ge structures on top of the waveguide. To strongly confine light in the InGaAsP MQWs for maximum modal gain, the waveguide is designed to be 1.5 μm-wide and extends 1 μm-deep into the InP substrate. When the pump light supplies a considerable gain to the InGaAsP/InP waveguide, the loss of the Cr/Ge structures reverses the sign of the imaginary part of the local modal index while maintaining almost the same real part and similar cross-sectional eigen-field distribution along the device. In our work, the additional Cr/Ge structure is of 7 nm-thick Cr and 7 nm-thick Ge, which leads to the effective modal index for both the loss and gain regions of $n_{eff} = 3.203 \pm 0.003i$, respectively, equivalent to a modal gain/loss coefficient of 250 cm^{-1} at the wavelength of 1540 nm. As a result, the guided light experiences an effectively pure gain-loss PT-symmetric modulation as

$$\Delta n = \begin{cases} n_{gain} = -in'' & (0 < z < a/2) \\ n_{loss} = in'' & (a/2 < z < a) \end{cases} \tag{3.16}$$

where n'' denotes the index modulation in only the imaginary part and a is the Bragg period corresponding to half the effective wavelength of the guided light. While the gain-loss modulation results in distributed optical feedback similar to conventional loss coupled-distributed feedback lasers [23], only the optical modulation stringently satisfying the combined PT symmetry can sustain simultaneous lasing and anti-lasing at the same eigen frequency in a single compact device [45]. In our work, specifically, the lasing and anti-lasing eigen-modes are degenerate at the boundary of the Brillouin zone due to the distributed Bragg feedback introduced by the periodic gain-loss interaction. By carefully designing the optical transfer matrix $M = \begin{bmatrix} M_{11} & M_{12}; & M_{21} & M_{22} \end{bmatrix}$ of such a two-port system using the coupled mode theory, our COAA can uniquely satisfy both the lasing ($M_{22} = 0$) and anti-lasing ($M_{11} = 0$) conditions. Remarkably, the realization of PT broken phase makes two mutually exclusive states – lasing (amplification) and anti-lasing (absorption) modes – synergize at the same frequency in the same device for the guided light. As shown in Figs. 3.16a and 3.16b, respectively, the lasing and anti-lasing eigen-states are orthogonal and spatially shifted by π in phase. Therefore, the optical switching between these two states can be demonstrated by tuning the initial phase offset of two counter-propagating coherent incoming beams to locate the constructive interference on demand. When the two incoming probe beams are -π/2 offset in phase (Fig. 3.16a), light is interferometrically confined in the gain regions where stimulated emission from the lasing mode takes place to resonantly amplify the outgoing beams. When the two incoming probe beams are of a π/2 offset (Fig. 3.16b), light becomes localized in the loss regions and coherently absorbed by the anti-lasing mode, thus strongly attenuating and even fully annihilating the outgoing beams. To minimize the possible scattering due to mode mismatch while switching between these two modes, the lasing and anti-lasing modes are designed to have similar cross-sectional electric field distribution confined in the top InGaAsP MQWs gain layer, as shown in Fig. 3.17a and Fig. 3.17b.

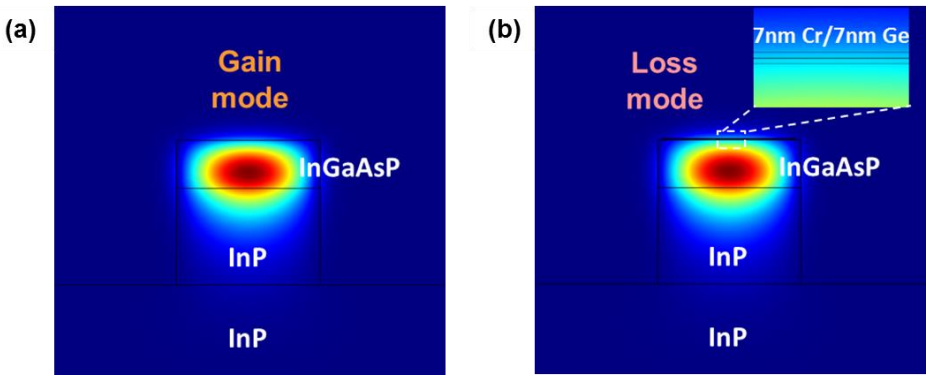

Figure 3.17 (a) Cross-sectional eigen field distribution of the lasing/amplification mode, leading to a gain-dominant effective index of $n_{eff} = 3.203 - 0.003i$. (b) Introducing the 7 nm Cr/7 nm Ge structure on top of the gain waveguide results in a similar cross-sectional eigen field distribution for the anti-lasing/absorption mode with a loss-dominant effective index of $n_{eff} = 3.203 + 0.003i$. These two modes with the complex conjugate effective indices lead to the pure gain/loss PT modulation required for supporting simultaneous lasing and anti-lasing.

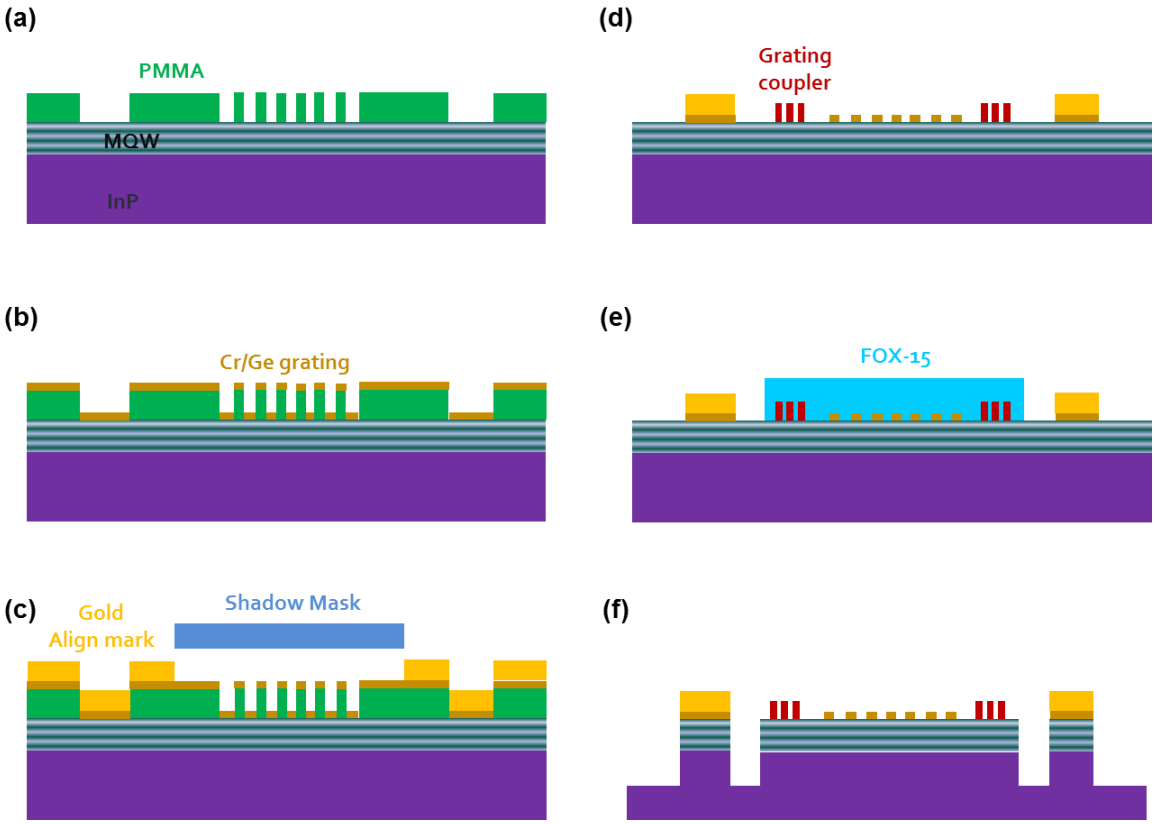

Figure 3.18 Schematic of the fabrication process. (a) EBL patterning of the COAA nanostructures and the alignment marks with a PMMA resist on a InGaAsP MQW grown on an InP substrate. (b) Electron beam evaporation of Cr/Ge layers to form the PT nanostructures. (c) Selective electron beam evaporation of a thick Au layer at the alignment mark positions using a shadow mask. (d) EBL patterning and lift-off process to form the thick Ge grating couplers. (e) EBL patterning on a FOX-15 negative resist to define the waveguides and MMI couplers. (f) Deep ICP etching followed by the removal of the masking layer.

The COAA sample is fabricated using overlay electron beam lithography and plasma etching. The key steps of the fabrication process are illustrated in Fig. 3.18. A 500-nm-thick InGaAsP multiple-quantum-well (MQW) was first grown on an InP substrate by metal organic chemical vapor deposition (MOCVD). The COAA pattern and the alignment marks were then defined in PMMA A2 resist by electron beam lithography (EBL), followed by electron beam evaporation of Chromium (Cr) and Germanium (Ge), 7 nm each, to form the PT structures. We then used a shadow mask to block the COAA area such that only the alignment mark regions were exposed where a 2 nm of Chromium (as adhesion layer) and a 40 nm of gold (Au) were deposited. Gold was used to make the alignment marks for its better image contrast under the scanning electron microscope (SEM) during the subsequent EBL alignment steps. Upon the lift-off process, the grating coupler patterns were defined in a thicker PMMA A6 resist by a second EBL exposure. Electron beam evaporation of 200-nm-thick Germanium was then carried out followed by another lift-off process. To define the multimode interference (MMI) coupler and the waveguide patterns, we used a thick HSQ (FOX-15) as the negative resist for the third EBL exposure. Upon development, the HSQ structures served as the etch mask for the 1.5-μm-deep inductively coupled plasma (ICP) etching using $Cl_2/CH_4/H_2$ gases. Finally, the mask layer was removed by soaking the sample in hydrofluoric (HF) acid solution for 1 minute. The SEM images of the fabricated samples are shown in Fig. 3.19.

In experiments, it is necessary to separate the input and output signals and simultaneously measure both the transmission and reflection spectra of the COAA waveguide. Although such a measurement is easy to perform for free space devices [34], to isolate the output signal from the input on a chip would require the use of external components that can route the light at will. To address this challenge in our on-chip measurements, we intentionally designed and fabricated, together with the COAA, 6 groups of Ge grating couplers and a pair of 2 × 2 multimode interference (MMI) couplers, as shown in Fig. 3.19b. While two input grating couplers convert light from free space to the guided mode, two MMI couplers efficiently sort the output signal from the input and guide them to different grating couplers that radiate the guided light back to free space. Essentially the input beams (I_1 and I_2) entering the COAA device are monitored using Coupler A and Coupler B, respectively, while the outgoing lights upon resonant coherent amplification/absorption (O_1 and O_2) associated with the lasing/anti-lasing states are collected using Coupler C and Coupler D, respectively. The output coefficient of the COAA, defined as the ratio of total outgoing light intensity to the total incoming light intensity for the device, can be determined,

$$\Theta = 2\left(\frac{O_1 + O_2}{I_1 + I_2}\right). \tag{3.17}$$

It is also important to note that probing and switching on the lasing and anti-lasing modes are based upon an interferometrically coherent strategy and thus insensitive to the incoherent contributions from the pump-induced spontaneous emission and background noise. Therefore, the undesired incoherent signals are deducted in all the terms defined in Θ.

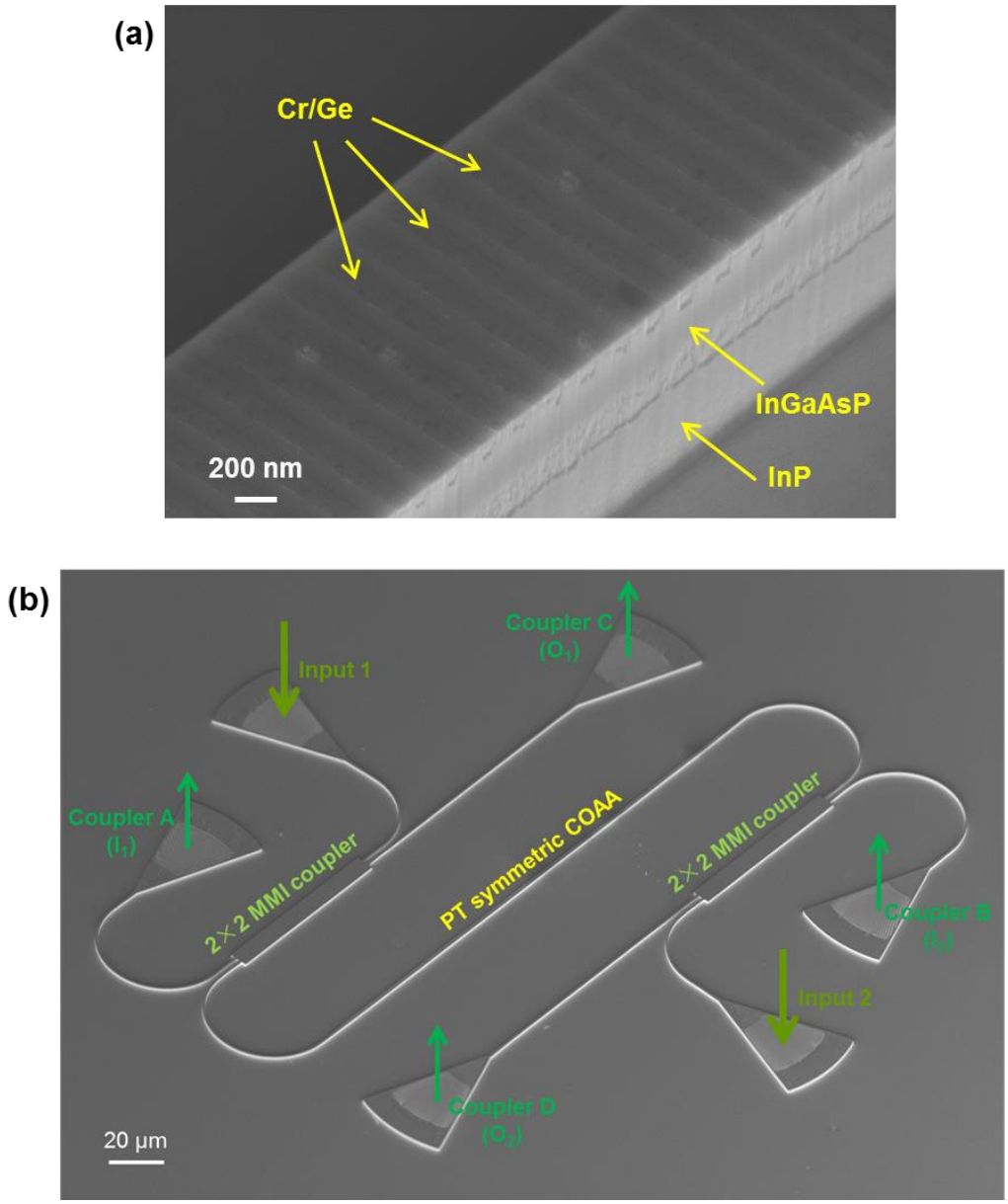

Figure 3.19 Experimental characterization scheme for the COAA to validate simultaneous lasing and anti-lasing. (a) SEM images of the fabricated COAA waveguide on the InGaAsP/InP platform. Coherent guided probe light coming from both directions selectively excites either the lasing mode or the anti-lasing mode by the interferometric phase control. (b) Full device layout to measure the incoming and outgoing light passing through the COAA to characterize the lasing/amplification by the lasing mode and anti-lasing/absorption due to the anti-lasing mode. Two probe beams are coupled into the waveguide using Input 1 and Input 2 grating couplers, respectively. Each of them is then equally split into two paths by a 2×2 multimode interference (MMI) coupler to isolate the input and output signals. By collecting the signal at Coupler A (B), the intensity of input light waves at the COAA boundary can be determined; meanwhile, upon interacting with the COAA, the outgoing waves are collected by Coupler C and Coupler D. The output coefficient of the COAA can thus be obtained by monitoring the outgoing lights from these grating couplers as $\Theta = 2\left(\frac{O_1 + O_2}{I_1 + I_2}\right)$, which is used to characterize the corresponding amplification/absorption of the fabricated COAA.

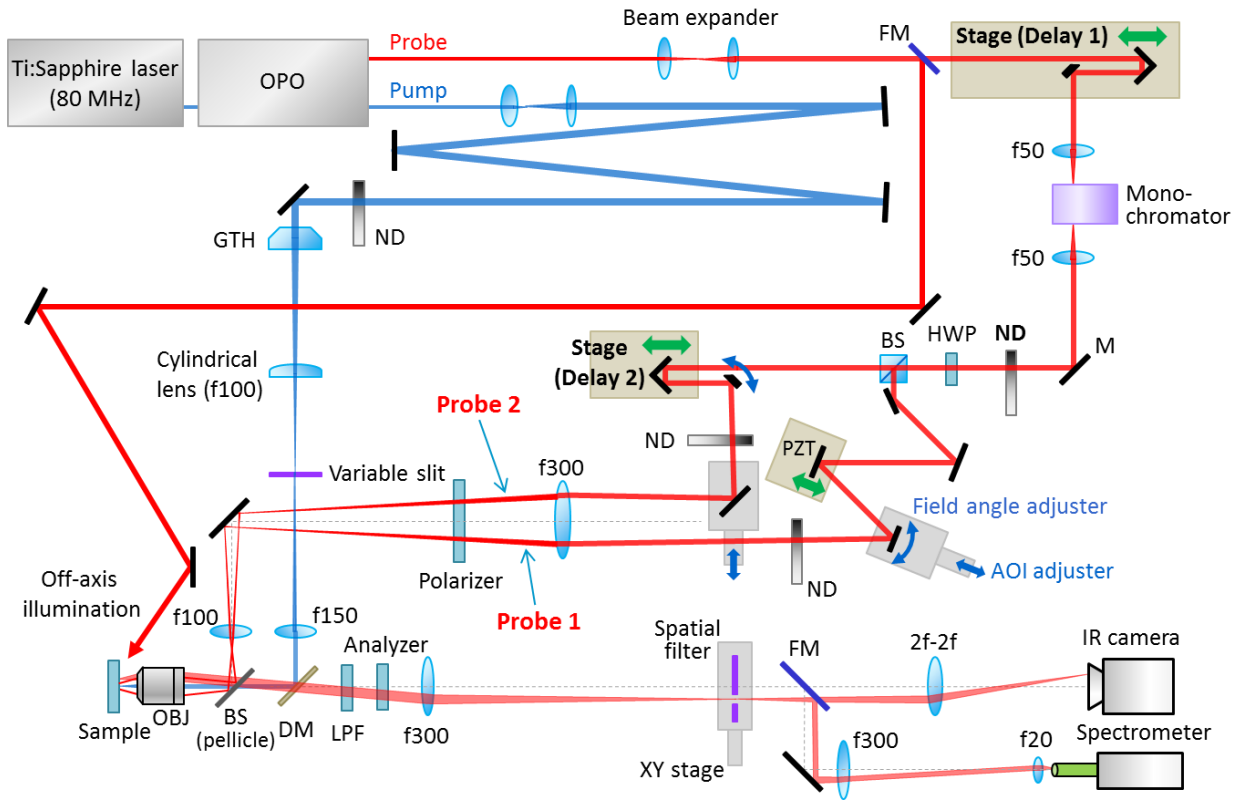

Figure 3.20 Schematic of the measurement setup. OPO: optical parametric oscillator; ND: variable neutral density filter; GTH: Gaussian-to-Top-Hat beam shaping lens; DM: dichroic mirror; BS: beam splitter; OBJ: objective lens; FM: flipping mirror; M: mirror; HWP: half-wave plate; PZT: piezoelectric actuator; LPF: long pass filter with a cutoff at 1500 nm.

To demonstrate coherent optical amplification and absorption, we built a single-pump double-probe measurement setup with precise phase control at telecommunication wavelengths. The detailed layout of the setup is shown in Fig. 3.20. To attain uniform pumping over the entire length of the PT-symmetric COAA, the pump beam from a mode-locked Ti:Sapphire laser (Chameleon Ultra II, Coherent) at 840 nm is carefully shaped into a slit beam as follows. We employ a Gaussian-to-Top-Hat beam shaping lens (GTH) which converts a Gaussian intensity profile into a square intensity profile. The Ti:Sapphire output was 2.2X expanded to make a Gaussian beam diameter ($1/e^2$) of 5 mm as an input requirement of GTH (GTH-5-250-4-IR, Eksma Optics). The GTH forms a square intensity distribution (4 mm x 4 mm) at 250 mm distance away. By placing a cylindrical lens at its focal distance (f = 100 mm), the square beam is transformed into a slit beam, of which length is fine-tuned by a variable slit. The tailored slit beam is 15x demagnified by the tube lens (f = 150 mm) and the objective lens (f = 10 mm, M Plan Apo NIR 20X, 0.40 NA, Mitutoyo) to uniformly pump only the PT-symmetric COAA area.

For unambiguous demonstration of the coherent amplification and absorption effects, two probe beams with precise phase control are required. The probe beams in our experiment are supplied from an OPO signal tuned to around 1540 nm in wavelength. The beam is collimated by 1.2X expansion optics and is passed through a monochromator (100 μm slit, MC1-05, Optometrics Corp.) to narrow its spectral width and increase its coherent length. Then the light is split into

two, forming the two probe beams which couple to the COAA device via input grating couplers at a designed angle of incidence (AOI) of 10°. The positions of the two mirrors sitting on one-dimensional (1D) stages (i.e. the AOI adjusters) are tuned to laterally shift the probe beams from the optical axis, thereby adjusting the AOIs of the probe beams onto the grating couplers as desired. Also, the tip/tilt of two mirrors (i.e. the Field angle adjusters), of which positions are conjugate to the back focal plane (BFP) of the objective lens through 3:1 reduced relay optics, is adjusted to induce field angles of the probe beams at the BFP, so that each of the focused probe spots illuminates the correct location of the gratings while keeping their AOIs unchanged. The "Delay 1", which consists of a retroreflector on a 1D motorized stage, is used to adjust the temporal overlap between the pump and probe pulses. The "Delay 2", another retroreflector on a 1D motorized stage, is utilized to further tune the delay between probe 1 and probe 2. A PZT is incorporated along the path of probe 1 to control the relative phase between the two probes and allow for precise phase scanning during the measurement. The HWP and linear polarizer provide the right polarization direction for the grating couplers, while the LPF and analyzer selectively capture the output probe signals. An iris on a XY stage, as a spatial filter, is placed at the intermediate image plane of the sample to spatially select the signal from one of the output gratings for collection. The position and the diameter of the iris are visually adjusted from images by an IR camera (SU640HSX-GV01, Goodrich Corp.) placed at the conjugate image plane via 2f-2f optics. The spatially filtered probe signal is captured by a spectrometer (SP-2300i, Princeton Instruments) through 15x demagnification optics. The off-axis illumination of a by-passed probe beam is intermittently used to find the device on the sample and to adjust the imaging focus of the device as seen by the IR camera. The mounted device is aligned to the pump beam and then the two probe beams are independently aligned to the corresponding input gratings. The picture of the built setup is shown in Fig. 3.21.

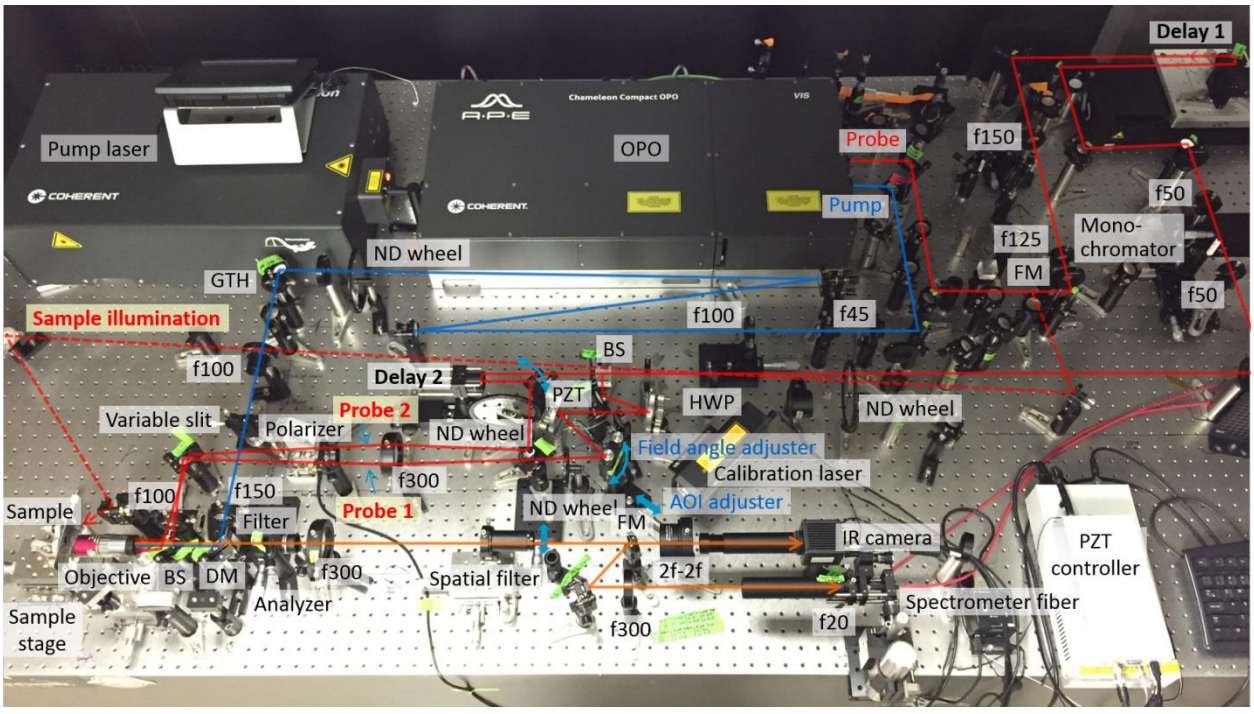

Figure 3.21 A picture of the real measurement setup built on an optical table.

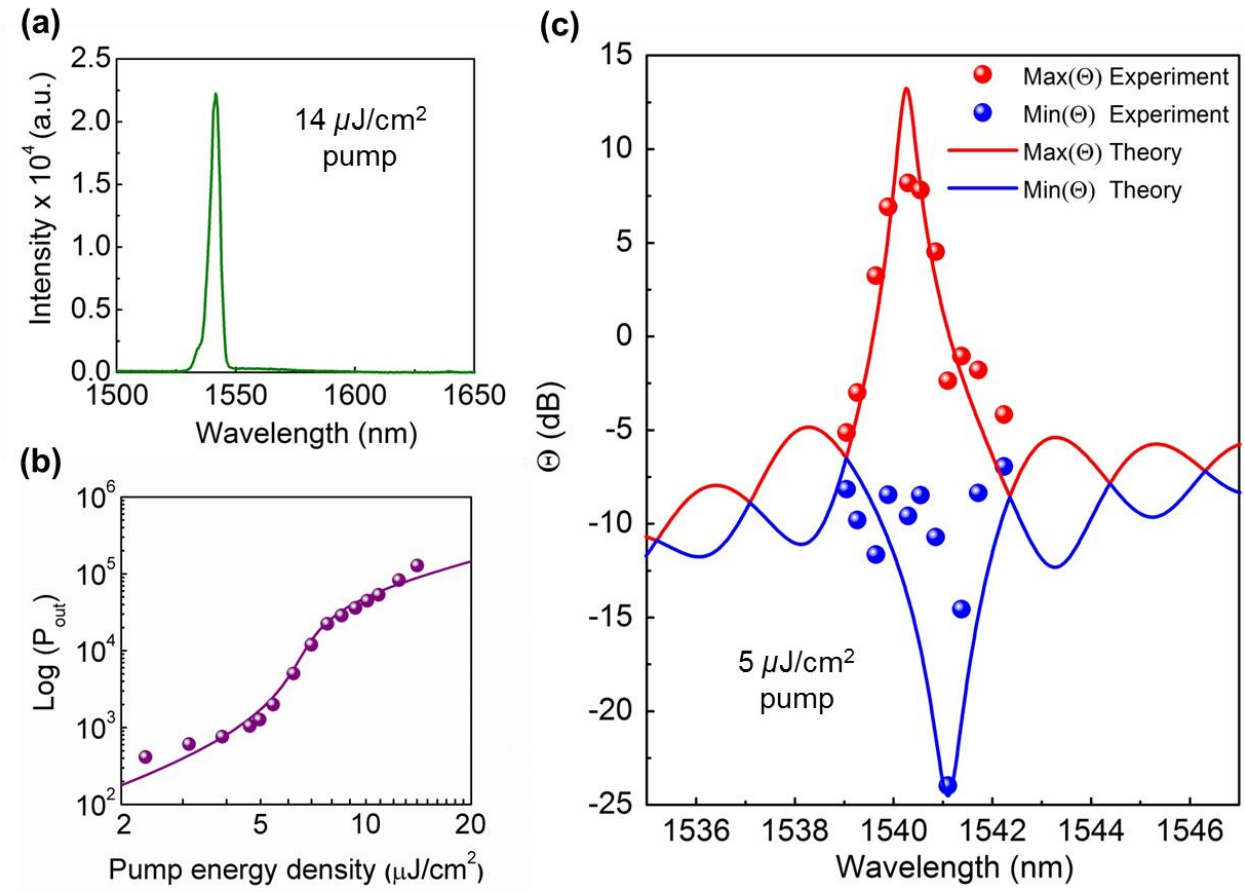

Figure 3.22 Lasing and anti-lasing modes in the COAA. (a) The lasing spectrum at pump energy density of 14 μJ/cm^2 well above the lasing threshold, showing the resonant lasing/amplification mode centered around 1541.6 nm. (b) Light-light curve plotted on a log-log scale, where the data points represent the experimental values and the solid line is based on the best-fit of the rate equation model. The lasing threshold occurs at around 5 μJ/cm^2, above which the effect of nonlinear laser dynamics on the exact PT symmetry and properties of the COAA remains unclear. We therefore performed the simultaneous lasing and anti-lasing characterizations around the lasing threshold. (c) The spectra output coefficient $\Theta = 2\left(\frac{O_1 + O_2}{I_1 + I_2}\right)$ of the COAA in the wavelength range from 1535 nm to 1547 nm for a pump energy density of 5 μJ/cm^2. With the -π/2 phase-offset probe beams, the maximum Θ, shown in red, manifests a distinct amplification peak of 8 dB at 1540.3 nm, corresponding to the resonant lasing mode; while with the π/2 phase-offset probe beams, the minimum Θ, shown in blue, is associated with the anti-lasing mode inducing an absorption dip down to -24 dB at 1541.1 nm. The lasing and anti-lasing modes share similar resonant wavelengths, which is due to the complex conjugate energy degeneracy supported by the PT broken phase. The small difference in their resonant wavelengths is caused by a slight mismatch of the real part of their mode index in the experiment, i.e. $\Delta n' = 0.002$ due to fabrication imperfection.

In the COAA under PT broken phase, the existence of the lasing mode can be directly validated with the lasing emission alone without the two probe beams. The PT gain/loss modulation was obtained by uniformly pumping the entire length of the COAA using a femtosecond pulse at the wavelength of 840 nm, which produced the Bragg optical feedback to support the mode oscillation in the COAA. As the pumping energy density is increased above the lasing threshold,

stimulated emission of the resonant lasing mode dominates and lasing oscillation is observed (Fig. 3.22a). With the pump energy density at 14 μJ/cm^2 a lasing peak inherently associated with PT broken phase occurs at the wavelength of 1541.6 nm, corresponding to the resonant wavelength of the lasing mode. Note that the lasing line broadening is observed. This is due to the ultrafast pump that cannot support an efficient overlap in time with the pump-generated carriers, leading to non-steady lasing emissions. The output light intensity as a function of pump energy density is plotted in Fig. 3.22b, which shows the lasing threshold, i.e. the nonlinear kink, at around 5 μJ/cm^2. On the other hand, the anti-lasing mode for coherent perfect absorption must be characterized using two coherent probe beams that mimic the time-reversed lasing radiation, while maintaining the same pump condition used in lasing and amplification measurements. It is ideal to have a large pump to enhance lasing and amplification, however, the nonlinear laser dynamics above the lasing threshold breaks the exact PT symmetry condition [45] that is required for the synergy of simultaneous lasing and anti-lasing. The effect from nonlinear laser dynamics on the COAA remains rather unclear. Therefore, we intentionally fixed the pump around the lasing threshold at 5 μJ/cm^2, where the lasing-associated optical nonlinearities were negligible, when we conducted the anti-lasing measurements. By controlling the phase offset between two probe beams to be $\pi/2$, we successfully excited the anti-lasing eigenmode with constructive light interference mainly localized in the loss regions. As shown in Fig. 3.22c, the sharp absorption dip of Θ down to -24 dB, in contrast to the lasing peak, can be observed at the anti-lasing resonant wavelength around 1541.1 nm. Meanwhile, when the phase offset between two probe beams was switched to $-\pi/2$, under the same pumping condition, the excited resonant mode became the lasing mode with a maximum amplified Θ of 8 dB at the wavelength around 1540.3 nm. The results clearly demonstrated the simultaneous coincidence of coherent amplification and absorption under the same resonant condition, which is due to the successful synergy of simultaneous lasing and anti-lasing in the COAA operated under PT symmetry breaking. In contrast to the standard optical modulators/amplifiers that are typically limited to either absorption or amplification alone, our COAA demonstrates the ability of achieving both amplification and absorption within a single device simply by tuning the phase, promising an ultimate limit to the maximum modulation depth attainable.

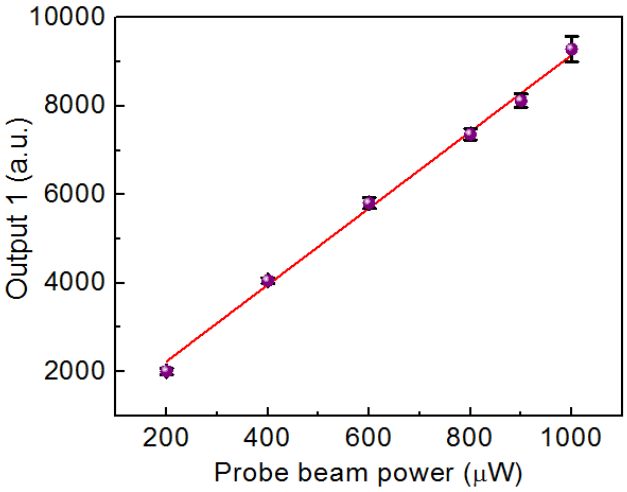

Figure 3.23 Linear scaling of output signals to the input probe beam power. The Output 1 signal intensity at the lasing/amplification mode is found to linearly scale with the averaged input probe power. The error bars are the standard deviations from 20 measurements.

It is important to note that strong probe beams can also cause undesired saturation effects and nonlinear frequency mixing with the pump beams. This in principle can also perturb the exact PT symmetry condition and degrade the associated amplification and absorption performance. To prove that the measured sharp amplification and absorption peaks are not caused by nonlinear interactions, we investigate the power scaling of the collected signals. The average probe power is tuned from 200 μW to 1000 μW by the variable neutral density (ND) filter wheel located between the monochromator and the HWP, while the Output 1 signal is measured at the coherent amplification resonance wavelength (1540.3 nm). It is apparent from Fig. 3.23 that the signals scale linearly with the input probe power. Since we perform the amplification and absorption measurements at 900 μW probe power, this confirms that the sharp amplification and absorption effects observed in our COAA strictly follows the linear scattering theory and it eliminates any contribution due to gain saturation and other nonlinear properties.

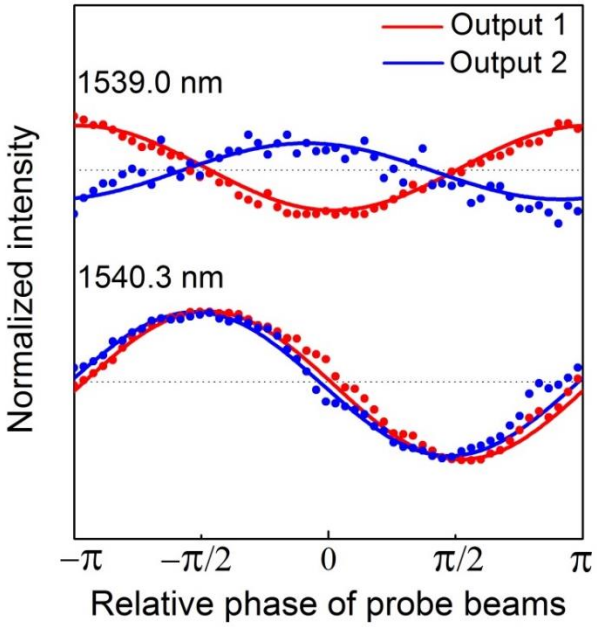

Figure 3.24 Phase response of outgoing waves by coherent light control. The phase response from both the normalized Output 1 and Output 2 signals by continuously varying the phase offset between probe beams from -π to π. For the phase-insensitive wavelength at 1539.0 nm (as a control), the two outgoing waves are completely out-of-phase. If the resonant mode (either lasing or anti-lasing) is excited, however, the outgoing waves become in-phase, as shown at 1540.3 nm wavelength.

While it is evident that the light modulation by our COAA is a linear coherent process based upon the coherent control on optical phase, we further investigated the related phase sensitivity at different wavelengths by monitoring the outgoing waves, as shown in Fig. 3.24. For the wavelengths where the system is on resonance where the strong distributed Bragg feedback is dominant, either the lasing or anti-lasing mode is excited with the constructive interference in the gain or loss regions, respectively. This requires the electric field inside the COAA to be closely in-phase, leading to the same in-phase outgoing waves from two different ports of the device. The phase dependences for both lasing and anti-lasing modes are almost identical, which again indicates the synergy of the lasing and anti-lasing modes by PT symmetry breaking. If the

operation wavelength is off resonance, a weak optical feedback is formed by the two boundaries of the COAA. Outgoing waves from the two ports continuously vary between in-phase and out-of-phase in wavelengths as suggested by the side ripples in the output coefficient spectra (Fig. 3.22c). The system becomes phase-insensitive where the amplification and absorption spectra cross [34], for example, at the wavelength of 1539.0 nm. Here, outgoing waves are completely out-of-phase, equal to the scattered field from incoherent illumination.

To better understand the coherent amplification and absorption mechanisms, we utilize the finite-difference time-domain technique (Lumerical FDTD software) to obtain the local field distribution inside the COAA device (i.e. at the gain/loss regions) in addition to acquiring the complex transmission and reflection properties. As shown in Fig. 3.25, two plane wave sources are excited in opposite directions at the left and right side of the COAA device respectively, and the input phase of source 1 can be easily tuned by changing its position. The two positions $-x_0 - \Delta x$ and $-x_0 + \Delta x$ correspond to $\pi/2$ and $-\pi/2$ phase difference between the two sources, respectively. Output monitor 1 and output monitor 2 are used to record the output at the left and right side of the device respectively, while the field monitor is used to record the field distribution throughout the entire device.

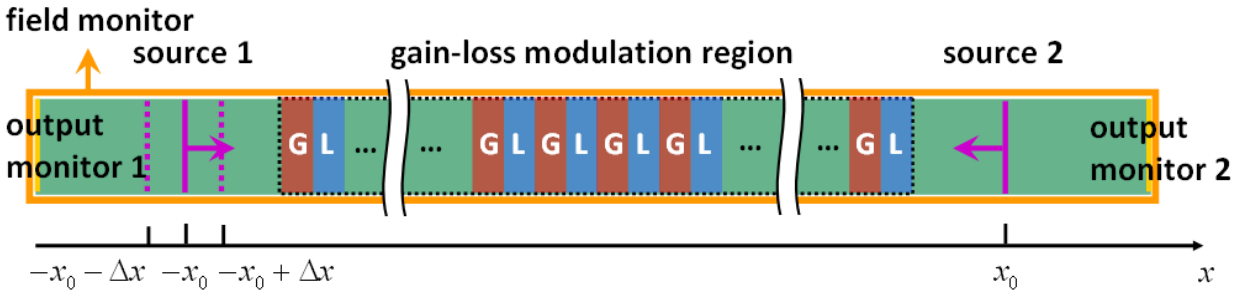

Figure 3.25 Setup of the numerical simulation. A schematic of the simulation setup and setting to capture the coherent amplification and absorption effects.

By directly adding the results recorded by the two output monitors (already normalized by the input sources), we can obtain the COAA output coefficient Θ. The maximum and minimum of Θ are acquired by altering the position of source 1, and consequently their responses at different wavelengths are obtained. Taking the non-perfect PT symmetric case as an example, we can see from Fig. 3.26 that the numerical simulation and coupled mode theory results are perfectly matched.

Upon verifying the rigorousness of this numerical simulation technique, we can then simulate the field distributions inside the COAA device. As shown in Fig. 3.27, at the control wavelength of 1539.0 nm, the electric field amplitude is located between the gain and loss regions, therefore the outgoing waves experience neither amplification nor absorption. On the contrary, when the amplification mode is excited at the wavelength of 1540.3 nm, the electric field amplitude is now confined in the gain regions, leading to in-phase constructive interference which strongly amplifies the outgoing waves.

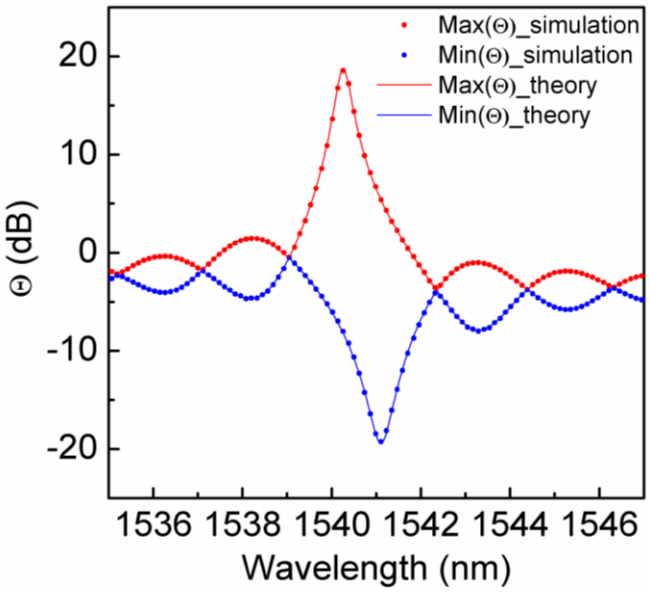

Figure 3.26 Perfect-matching between the simulated and theoretical results. COAA output coefficient Θ versus wavelength for the non-perfect PT symmetric case where the dots and curves denote the simulation and theoretical results respectively, which show perfect agreement.

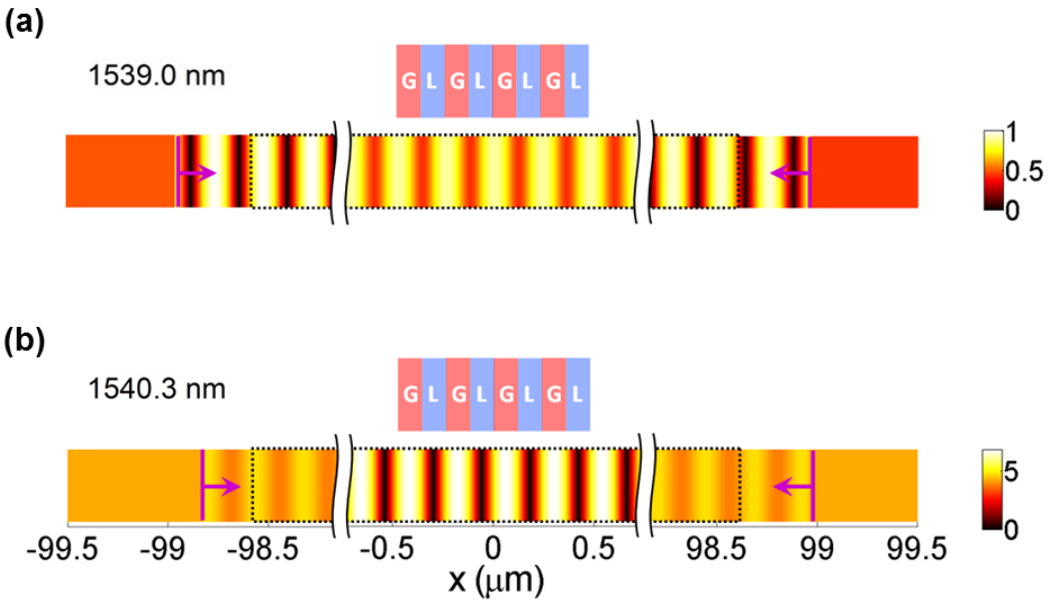

Figure 3.27 At the phase-insensitive wavelength of 1539.0 nm (as a control), the interference pattern is located between gain and loss regions, leading to the scattered intensities similar to incoherent illumination. When the lasing (anti-lasing) resonant mode is excited, at 1540.3 nm for example, the interfered electric field amplitude distribution can be predominantly confined in the gain (loss) regions, which leads to strong coherent amplification (absorption) for the outgoing waves at both ends. The dotted lines mark the position of the COAA with the arrows representing the incoming probe beams. Depending on the arrow position, a phase shift to one of the incident probe beams can be introduced.

To further understand the phase relationship between the two outgoing waves, we plot here the output phase difference ($|\Delta\varphi_{out}| = |\Delta\varphi_{out,1} - \Delta\varphi_{out,2}|$) as a function of wavelength. As shown in Fig. 3.28, the overall trend of the measured data agrees well with the simulation result. When the two outgoing waves are out-of-phase for the off-resonance wavelength such as 1539.0 nm, they are completely out-of-phase. However, the output phase difference gradually diminishes as it approaches the coherent amplification (1540.3 nm) and absorption (1541.1 nm) resonance wavelengths. This closely in-phase behavior is to be expected due to the constructive interference in the gain/loss regions, which leads to simultaneous buildup/termination of the outgoing waves at both ports of the COAA device. This confirms the similar phase dependence of the lasing and anti-lasing modes in the COAA.

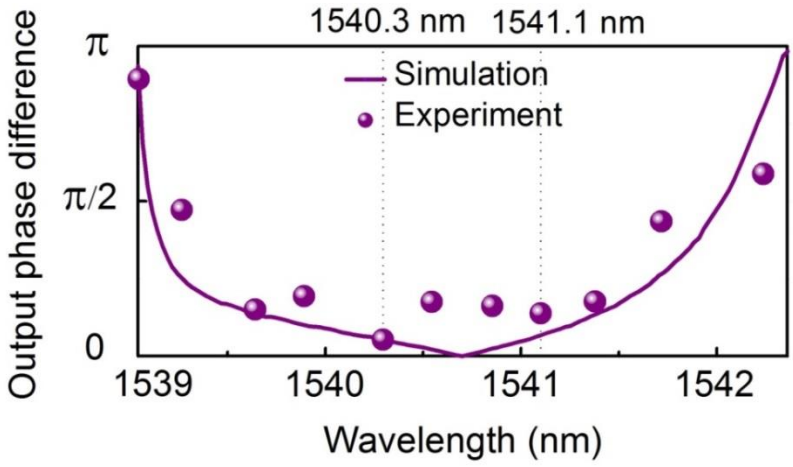

Figure 3.28 Output phase difference versus wavelength. The relative phase difference between the two outgoing waves gradually diminishes as the wavelength approaches the point of lasing and anti-lasing modes.

3.4 Summary and Outlook

In this chapter, we showed how the imaginary part of refractive index can be engineered to realize unique optical devices. Using the concept of PT symmetry, loss and gain structures are coupled to give rise to degenerate gain and loss resonant modes. First we experimentally demonstrated a PT single-mode laser with unique mode control capability. Thresholdless PT symmetry breaking due to the rotationally symmetric microring structure leads to stable single-mode operation with the selective whispering gallery mode order. Next we realized a coherent optical amplifier-absorber that uniquely attained both the lasing and anti-lasing states within a single device, paving the way for optical modulators approaching the ultimate modulate depth limit.

The engineering of loss and its interplay with gain is no doubt extremely important in optical metamaterials research. This opens plenty of new opportunities for using the lossy metals to manipulate the cavity modes, steer the radiation profile, and enable unidirectional light transport in photonic integrated circuits. Incorporating nonlinearity in a PT symmetric system can

potentially lead to many interesting nonlinear optical devices (eg. saturable absorbers, Raman, optical solitons, etc) with unique properties unattainable otherwise. It might even be possible to generalize the synergy between the loss and gain mediums to other opposite states, such as the interplay between negative index and positive index materials.

References

[1] D. J. Griffiths, "Introduction to quantum mechanics," Pearson Prentice Hall (2005).

[2] D. A. B. Miller, "Quantum mechanics for scientists and engineers," Cambridge University Press (2008).

[3] C. M. Bender and S. Boettcher, "Real spectra in non-Hermitian Hamiltonians having PT symmetry," *Physical Review Letters* **80**, 5243 (1998).

[4] C. M. Bender, "Making sense of non-Hermitian Hamiltonians," *Reports on Progress in Physics* **70**, 947 (2007).

[5] R. El-Ganainy, K. G. Makris, D. N. Christodoulides, and Z. H. Musslimani, "Theory of coupled optical PT-symmetric structures," *Optics Letters* **32**, 2632 (2007).

[6] K. G. Makris, R. El-Ganainy, D. N. Christodoulides, and Z. H. Musslimani, "Beam dynamics in PT-symmetric optical lattices," *Physical Review Letters* **100**, 103904 (2008).

[7] Z. H. Musslimani, R. El-Ganainy, K. G. Makris, and D. N. Christodoulides, "Optical solitons in PT periodic potentials," *Physical Review Letters* **100**, 030402 (2008).

[8] C. E. Rüter, K. G. Makris, R. El-Ganainy, D. N. Christodoulides, M. Segev, and D. Kip, "Observation of parity-time symmetry in optics," *Nature Physics* **6**, 192 (2010).

[9] S. Klaiman, U. Guenther, and N. Moiseyev, "Visualization of branch points in PT-symmetric waveguides," *Physical Review Letters* **101**, 080402 (2008).

[10] S. Longhi, "Bloch oscillations in complex crystals with PT symmetry," *Physical Review Letters* **103**, 123601 (2009).

[11] A. Guo, G. J. Salamo, D. Duchesne, R. Morandotti, M. Volatier-Ravat, V. Aimez, G. A. Siviloglou, and D. N. Christodoulides, "Observation of PT-symmetry breaking in complex optical poteneials," *Physical Review Letters* **103**, 093902 (2009).

[12] Z. Lin, H. Ramezani, T. Eichelkraut, T. Kottos, H. Cao, and D. N. Christodoulides, "Unidirectional invisibility induced by PT-symmetric periodic structures," *Physical Review Letters* **106**, 213901 (2011).

[13] A. Regensburger, C. Bersch, M.-A. Miri, G. Onischukov, D. N. Christodoulides, and U. Peschel, "Parity-time synthetic photonic lattices," *Nature* **488**, 167 (2012).

[14] L. Feng, Y.-L. Xu, W. S. Fegadolli, M.-H. Lu, J. E. B. Oliveira, V. R. Almeida, Y.-F. Chen, and A. Scherer, *Nature Materials* **12**, 108 (2013).

[15] B. Peng, Ş. K. Özdemir, F. Lei, F. Monifi, M. Gianfreda, G. L. Long, S. Fan, F. Nori, C. M. Bender, and L. Yang, *Nature Physics* **10**, 394 (2014).

[16] L. Chang, X. Jiang, S. Hua, C. Yang, J. Wen, L. Jiang, G. Li, G. Wang, and M. Xiao, "Parity-time symmetry and variable optical isolation in active-passive-coupled microresonators," *Nature Photonics* **8**, 524 (2014).

[17] L. Feng, Z. J. Wong, R.-M. Ma, Y. Wang, and X. Zhang, "Single-mode laser by parity-time symmetry breaking," *Science* **346**, 972 (2014).

[18] H. Hodaei, M.-A. Miri, M. Heinrich, D. N. Christodoulides, and M. Khajavikhan, "Parity-time-symmetric microring lasers," *Science* **346**, 975 (2014).

[19] M. Brandstetter, M. Liertzer, C. Deutsch, P. Klang, J. Schöberl, H. E. Türeci, G. Strasser, K. Unterrainer, and S. Rotter, "Reversing the pump dependence of a laser at an exceptional point," *Nature Communications* **5**, 4034 (2014).
[20] B. Peng, Ş. K. Özdemir, S. Rotter, H. Yilmaz, M. Liertzer, F. Monifi, C. M. Bender, F. Nori, and L. Yang, "Loss-induced suppression and revival of lasing," *Science* **346**, 328 (2014).
[21] H. Schomerus, "Quantum noise and self-sustained radiation of PT-symmetric systems," *Physical Review Letters* **104**, 233061 (2010).
[22] D. C. Hanna, B. Luther-Davies, and R. C. Smith, "Active Q switching technique for producing high laser power in a single longitudinal mode," *Electronics Letters* **8**, 369 (1972).
[23] H. Ghafouri-Shiraz, "Distributed feedback laser diodes and optical tunable filters," Wiley (2003).
[24] M. T. Hill, Y.-S. Oei, B. Smalbrugge, Y. Zhu, T. de Vries, P. J. can Veldhoven, F. W. M. van Otten, T. J. Eijkemans, J. P. Turkiewicz, H. de Waardt, E. J. Geluk, S.-H. Kwon, Y.-H. Lee, R. Nötzel, and M. K. Smit, "Lasing in metallic-coated nanocavities," *Nature Photonics* **1**, 589 (2007).
[25] R. M. Ma, R. F. Oulton, V. J. Sorger, G. Bartal, and X. Zhang, "Room-temperature sub-diffraction-limited plasmon laser by total internal reflection," *Nature Materials* **10**, 110 (2011).
[26] S. F. Liew, B. Redding, L. Ge, G. S. Solomon, and H. Cao, "Active control of emission directionality of semiconductor microdisk lasers," *Applied Physics Letters* **104**, 231108 (2014).
[27] M. Korbl, A. Groning, H. Schweizer, and J. L. Gentner, "Gain spectra of coupled InGaAsP/InP quantum wells measured with a segmented contact traveling wave device," *Journal of Applied Physics* **92**, 2942 (2002).
[28] J. Wiersig, S. W. Kim, and M. Hentschel, "Asymmetric scattering and nonorthogonal mode patterns in optical microspirals," *Physical Review A* **78**, 053809 (2008).
[29] Y. Lumer, Y. Plotnik, M. C. Rechtsman, and M. Segev, "Nonlinearly induced PT transition in photonic systems," *Physical Review Letters* **111**, 263901 (2013).
[30] Y. D. Chong, L. Ge, and A. D. Stone, "PT-symmetry breaking and laser-absorber modes in optical scattering systems," *Physical Review Letters* **106**, 093902 (2011).
[31] L. Shang, L. Liu, and L. Xu, "Single-frequency coupled asymmetric microcavity laser," *Optics Letters* **33**, 1150 (2008).
[32] A. Arbabi, Y. M. Kang, C.-Y. Lu, E. Chow, and L. L. Goddard, "Realization of a narrowband single wavelength microring mirror," *Applied Physics Letters* **99**, 091105 (2011).
[33] Y. D. Chong, L. Ge, H. Cao, and A. D. Stone, "Coherent perfect absorbers: Time-reversed lasers," *Physical Review Letters* **105**, 053901 (2010).
[34] W. Wan, Y. C, L. Ge, H. Noh, A. D. Stone, and H. Cao, "Time-reversed lasing and interferometric control of absorption," *Science* **331**, 889 (2011).
[35] S. Xiao, V. P . Drachev, A. V. Kildishev, X. Ni, U. K. Chettiar, H.-K. Yuan, and V. M. Shalaev, "Loss-free and active optical negative-index metamaterials," *Nature* **466**, 735 (2010).
[36] O. Hess, J. B. Pendry, S. A. Maier, R. F. Oulton, J. M. Hamm, and K. L. Tsakmakidis, "Active nanoplasmonic metamaterials," *Nature Materials* **11**, 573 (2012).
[37] H. Noh, Y. Chong, A. D. Stone, and H. Cao, "Perfect coupling of light to surface plasmons by coherent absorption," *Physical Review Letters* **108**, 186805 (2012).

[38] M. Pu, Q. Feng, M. Wang, C. Hu, C. Huang, X. Ma, Z. Zhao, C. Wang, and X. Luo, *Optics Express* **20**, 2246 (2012).
[39] Y. Fan, F. Zhang, Q. Zhao, Z. Wei, H. Li, "Tunable terahertz coherent perfect absorption in a monolayer graphene," *Optics Letters* **39**, 6269 (2014).
[40] R. Bruck and O. L. Muskens, "Plasmonic nanoantennas as integrated coherent perfect absorbers on SOI waveguides for modulators and all-optical switches," *Optics Express* **21**, 27652 (2013).
[41] G. T. Reed, G. Mashanovich, F. Y. Gardes, and D. J. Thomson, "Silicon optical modulators," *Nature Photonics* **4**, 518 (2010).
[42] J. Zhang, K. F. MacDonald, and N. I. Zheludev, "Controlling light-with-light without nonlinearity," *Light: Science & Applications* **1**, e18 (2012).
[43] Q. Xu. B. Schmidt, S. Pradhan, and M. Lipson, "Micrometre-scale silicon electro-optic modulator," *Nature* **435**, 325 (2005).
[44] M. Hochberg, T. Baehr-Jones, G. Wang, M. Shearn, K. Harvard, J. Luo, B. Chen. Z. Shi. R. Lawson, P. Sullivan, A. K. Y. Jen, L. Dalton, and A. Schrer, "Terahertz all-optical modulation in a silicon-polymer hybrid system," *Nature Materials* **5**, 703 (2006).
[45] S. Longhi, "PT-symmetric laser absorber," *Physical Review A* **82**, 031801(R) (2010).
[46] S. Longhi, and L. Feng, "PT-symmetric microring laser-absorber," *Optics Letters* **39**, 5026 (2014).

Chapter 4

Subwavelength Local Phase Engineering

4.1 Metasurface

Recent development of metasurfaces pointed out a way to manipulate the phase of a propagating wave directly. The metasurface is an optically thin layer consisting of subwavelength-sized elements with the unique ability to locally tailor the electromagnetic response at the nanoscale accompanied by dramatic light confinement [1-7]. Metasurfaces have enabled a variety of unique phenomena and applications which cannot be achieved conventionally [8,9], for example, negative-angle refraction in a broad wavelength range [1,2], unidirectional surface wave coupling [10,11], planar optical lenses and waveplates [4,12-15], ultra-thin high-resolution holograms [16-18], and enhancement of nonlinear optical responses [19]. Fig. 4.1 shows some of the key achievements using metasurfaces.

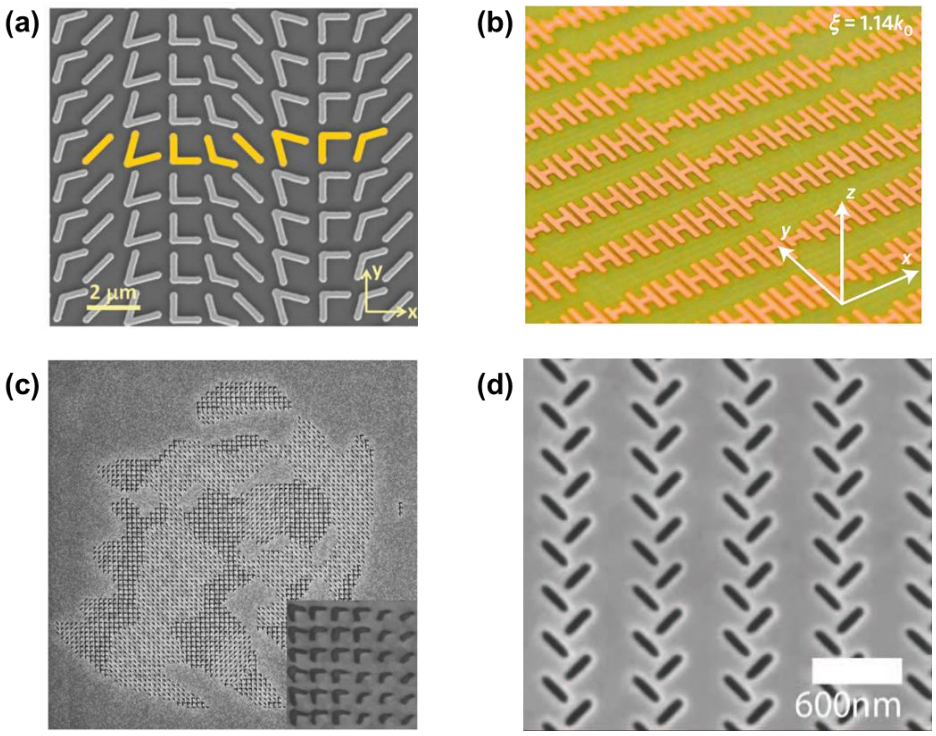

Figure 4.1 Representative metasurface works demonstrating novel light properties: (a) Anomalous reflection and refraction at 8 μm wavelength [1]. (b) Perfect coupling from propagating waves to surface waves at 15 GHz microwave frequency [3]. (c) Ultra-thin holograms for visible light at 676 nm [17]. (d) Polarization-controlled tunable directional coupling of surface plasmon polaritons at 633 nm [11].

4.2 Ultra-thin Three-dimensional Invisibility Skin Cloak

A cloak is a stealth device that can render objects invisible under illumination of incoming waves. Transformation optics and metamaterials provide us powerful tools to build cloaking devices. Different schemes, either by coordinate transformation [20-22] or by scattering cancellation [23-25] have been studied. Although the concept was first proposed for electromagnetic waves, soon it was extended to acoustic waves [26], heat flows [27-29], elastic or seismic waves [30-32], and even for the matter waves [33,34]. Recently, a quasi-conformal mapping technique [35] was used to design a so-called carpet cloak that conceals an object by restoring the wavefront as if it were reflected from a flat surface. This technique relaxes the requirement of extreme material properties and anisotropy as in the case of the original cloak, therefore making it easier to design and fabricate. Such invisibility carpet cloaks were demonstrated experimentally from the microwave frequencies [36,37] up to the optical frequencies [38-44], as summarized in Fig. 4.2. Recent theoretical proposal also suggested the use of phase gradient along a metasurface to build an ultra-thin invisibility device in the terahertz frequency regime [45].

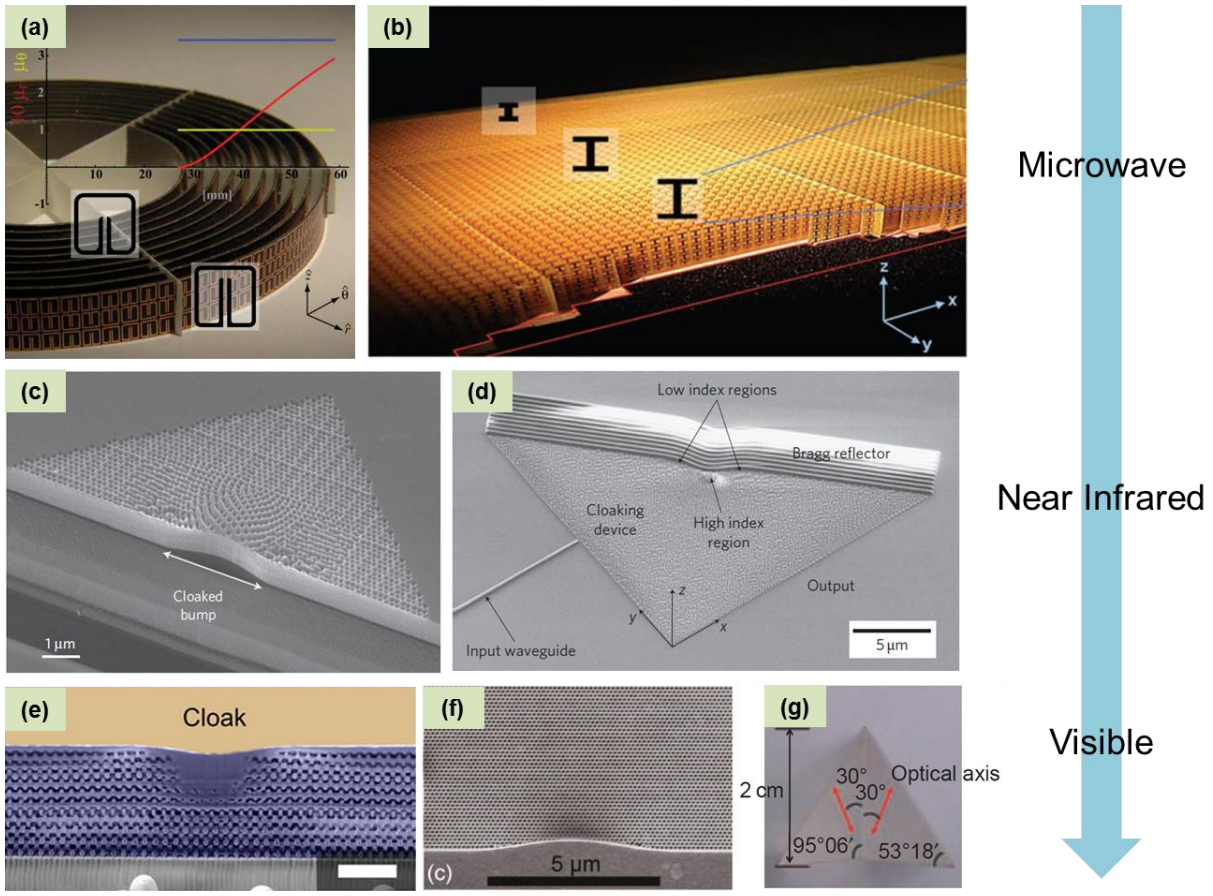

Figure 4.2 Experimental realizations of electromagnetic cloaks in thfenge past decades from microwave to visible frequencies. (a) The first cloak used copper split ring resonators with spatially varying effective magnetic permeability to achieve the cloaking effect at 8.5 GHz [21]. (b) A broadband carpet cloak using non-resonant metamaterial elements working from 13-16 GHz [36]. (c) A dielectric cloak working for a broad range of wavelengths (1.4 μm to 1.8 μm) was built by spatially varying the filling fraction of silicon (using effective medium theory) to achieve the required index distribution for cloaking [38]. (d) A

near infrared cloak similar to (c) except pillars of nanostructured silicon were formed (instead of holes in (c)) [39]. (e) A three-dimensional cloak made using direct laser writing showed good cloaking performance down to about 600nm [41]. (f) A visible cloak using similar design strategy as (c) but with a finer resolution silicon nitride structures enabled cloaking from 700 nm down to 480 nm [42]. (g) A macroscopic visible cloak using natural birefringent crystal at 532 nm wavelength. All the cloaks above used either the transformation optics principle or the quasi-conformal mapping technique, where all of them (except (g)) require a spatial variation of the electromagnetic property [43].

Nevertheless, there are still significant limitations in the current optical cloak designs which utilize the quasi-conformal mapping technique. This requires that the refractive index modulation is over a large volume to avoid extremely high or low index, leading to a bulky cloak. In addition, this necessitates sophisticated three-dimensional fabrication with very high spatial resolution. Therefore, it is extremely challenging to scale up to macroscopic sizes. In addition, the varying index has to be less than that of the environment in certain regions (Fig. 4.3a), making it difficult to create a cloak working in the air. As a result, the cloak is usually embedded in a dielectric prism of higher index which, however, introduces an additional phase in the reflected light, and makes the optical cloak itself visible by phase-sensitive detection.

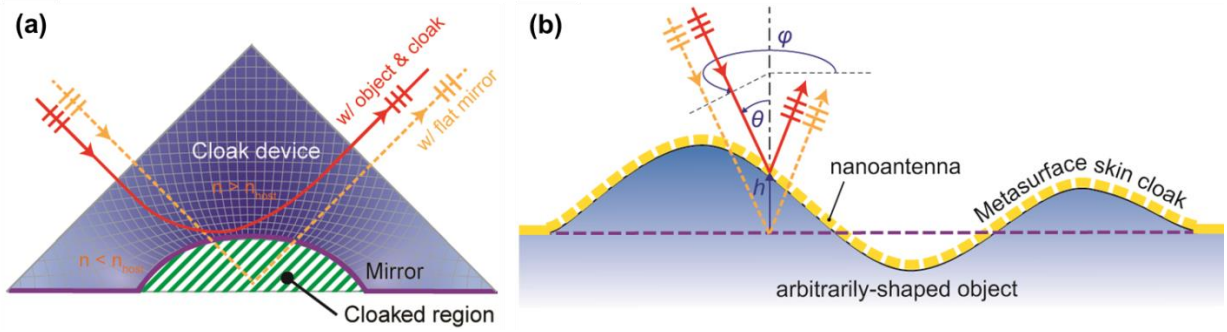

Figure 4.3 (a) A schematic illustration of a conventional carpet cloak. The cloak device is a region with spatially varying refractive index designed using optical conformal/quasi-conformal mapping technique. The blue color of the cloak device region qualitatively indicates the local refractive index (the darker color indicates higher index) and the grid lines indicate the deformed optical space. The light incidents from the left and exits to the right as represented by the arrowed lines. The devices recover the wavefront (indicated as triple short lines) of the exiting light, such that the object is hidden and look like a flat mirror judging from the scattering pattern of the exiting light. However, a typical conventional cloak introduces additional phase retardation due to the light propagation inside its host material, which makes it detectable to the phase-sensitive measuring devices. (b) A schematic view of a cross section of the metasurface skin cloak. The metasurface skin cloak fully restores both the wavefront and the phase of the scattered light and thus the object is perfectly hidden. On a metasurface skin cloak, a phase shift is provided by each nanoantenna to realign the wavefront. At an arbitrary point on the object with height h to the flat reference plane, the nanoantenna should recover the phase of the scattered light. Suppose the light (red solid lines) is incident at an oblique angle (θ, φ) at that point, the scattered wave should look as if it were reflected by the reference plane (orange dashed lines). The nanoantenna at that point should provide a phase shift $\Delta\Phi = -2k_0 h\cos\theta + \pi$, which compensates the phase difference between the solid and dashed lines. Note that the height is negative where the surface is below the reference plane.

Here, we aim to demonstrate an ultra-thin invisibility skin cloak in the optical frequencies that overcomes the limitations of a bulky cloak. A metasurface conformally wrapped over an object to render it free from optical detection highly desired. In contrast to the previous bulky design

using continuous refractive index distribution over a volumetric space [35], an ultra-thin layer of skin cloak can reroute the light and restore the wavefront scattered from the object by compensating the phase difference using phase-shifting resonant elements on the cloak surface. With the complete wavefront and phase recovery, a three-dimensional object of arbitrary shape can be concealed using this skin cloak.

Our metasurface skin cloak consists of subwavelength-scale nanoantennas which provide distinct phase shifts locally to the reflected electromagnetic waves. Based on this phase control capability, we design a metasurface so that the phase of the scattered light, at each point on the surface of the cloak, is the same as that reflected from a flat mirror. For an oblique-angle (θ, φ) light incident on an arbitrarily-shaped three-dimensional object at a height of h with respect to the reference plane (Fig. 4.3b), the introduced phase shift should compensate the phase difference between the light scattered by the object and that reflected from the reference plane. It is straightforward to calculate the phase difference, which is $\Delta\Phi = -2k_0 h\cos\theta + \pi$, where$k_0$ is the free space wavenumber. The additional π term represents the phase jump induced by a reflecting mirror. Therefore, by designing nanoantennas with local phase shift, the scattered wavefront will be re-aligned. Moreover, the phase will be completely restored, rendering the object undetectable even for phase-sensitive instruments.

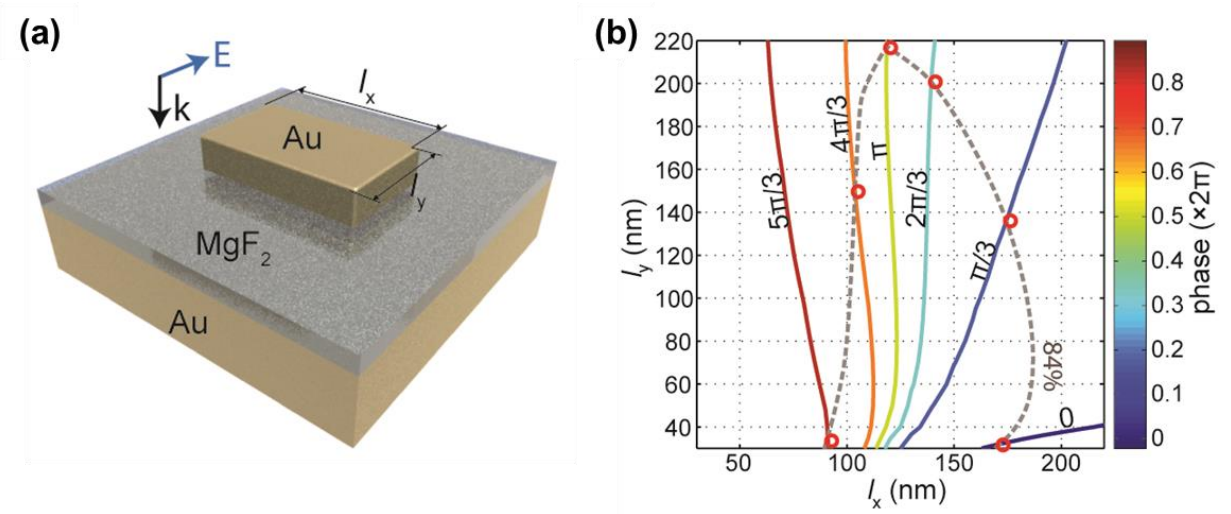

Figure 4.4 (a) A three-dimensional illustration of a nanoantenna used to build the metasurface. (b) Calculated phase shifts and reflectance in a two-dimensional parameter space spanned by l_x and l_y. The solid lines are the contour lines of the phase shift and the dashed line is the contour line of the reflectance at 84%. For simplicity, six different nanoantennas which span the phase from 0 to 2π with an interval of π/3 are chosen as the building blocks to construct the metasurface, as shown by the six red circles intersecting the phase and the 84%-reflectance contour lines.

As a demonstration, we use a simple rectangular nanoantenna design (Fig. 4.4a). The calculated phase shifts and reflectance in a two-dimensional parameter space spanned by nanoantenna dimensions l_x and l_y are mapped out for the selection of designs. Six different antennas with phase shifts covering 0 to 2π while having the same reflectance are chosen as the building blocks of the metasurface skin cloak. To make the invisibility cloak fully working, we need the reflected intensity as close as that to a mirror. With adaptation of an ultra-thin dielectric spacer layer to

create a gap plasmon resonance [46,47], our antennas are designed to attain an overall reflectivity of 84%. The parameters for the nanoantennas used in our experiment are indicated as red circles in Fig. 4.4b. We build a metasurface using those nanoantennas to compensate the local phase change of the reflection.

Full-wave simulation results show that strong scattering and significant wavefront and phase distortion can occur for an arbitrarily-shaped three-dimensional object with a maximum height of about 1 μm and a width of about 10 μm (Fig. 4.5a). However, by wrapping the object with the metasurface skin cloak, the wavefront and phase are completely restored for both normal (Fig. 4.5b) and slightly oblique incidences (Fig.4.5c). Therefore the object is perfectly hidden even from phase sensitive detection.

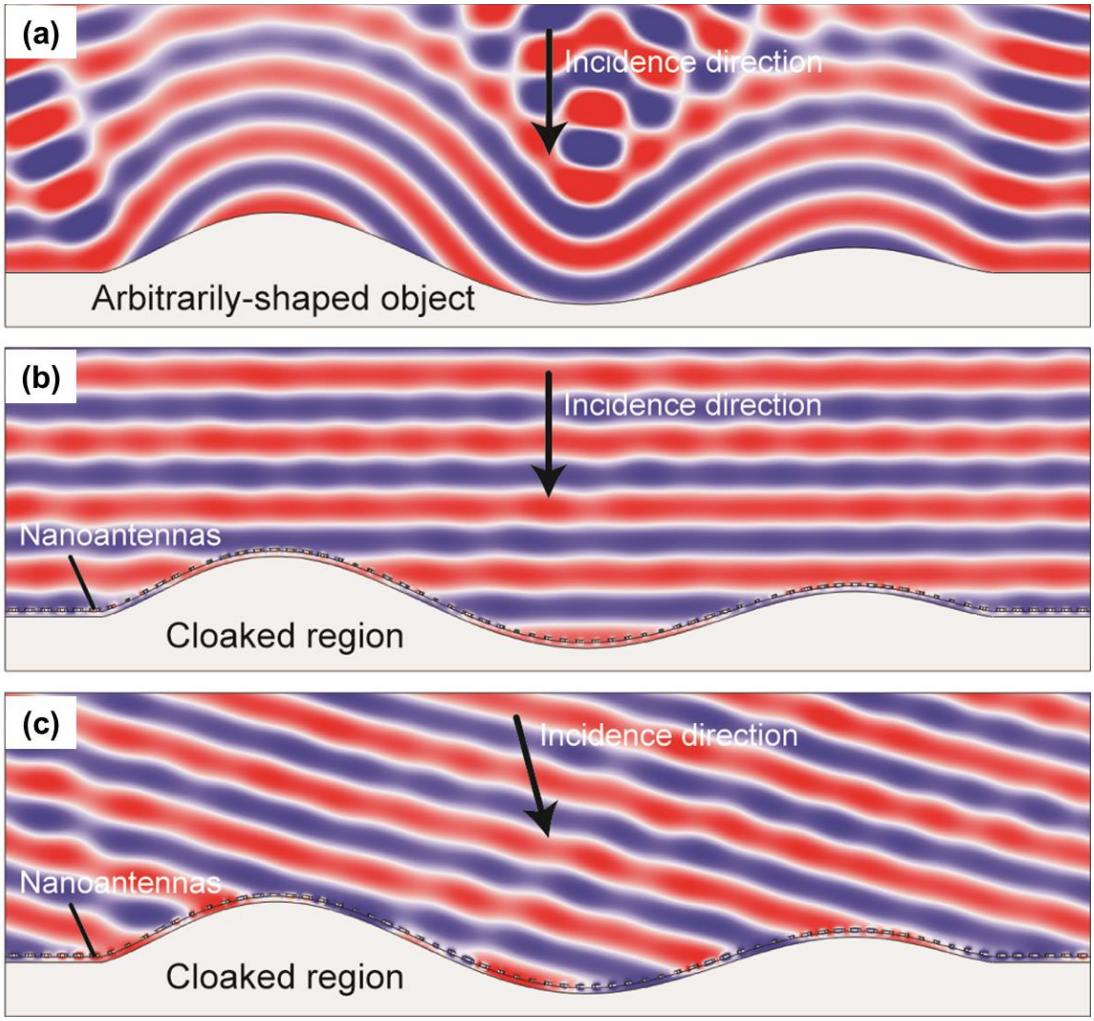

Figure 4.5 (a-c) Full-wave simulated electrical field distribution (shown for a cross section) based on an actual design for (a) a scattering object without a metasurface skin cloak at a normal incidence, (b) the same object with a metasurface skin cloak at a normal incidence, and (c) the same object with the same metasurface skin cloak as in (b) but at a 15degree oblique incidence. Only the reflected field is plotted for clarity. The wavelength of the incident light is 730 nm in the simulation. We can clearly see that the reflected light is almost completely recovered by the skin cloak as if there were no scattering object for both normal and oblique incidence cases.

Our ultra-thin device has merely a thickness of 80 nm (~λ/9) and has much better scalability since the device is two-dimensional. An illustration of the ultra-thin metasurface skin cloak conformally wrapped on a three-dimensional object of arbitrary shape is shown in Fig. 4.6.

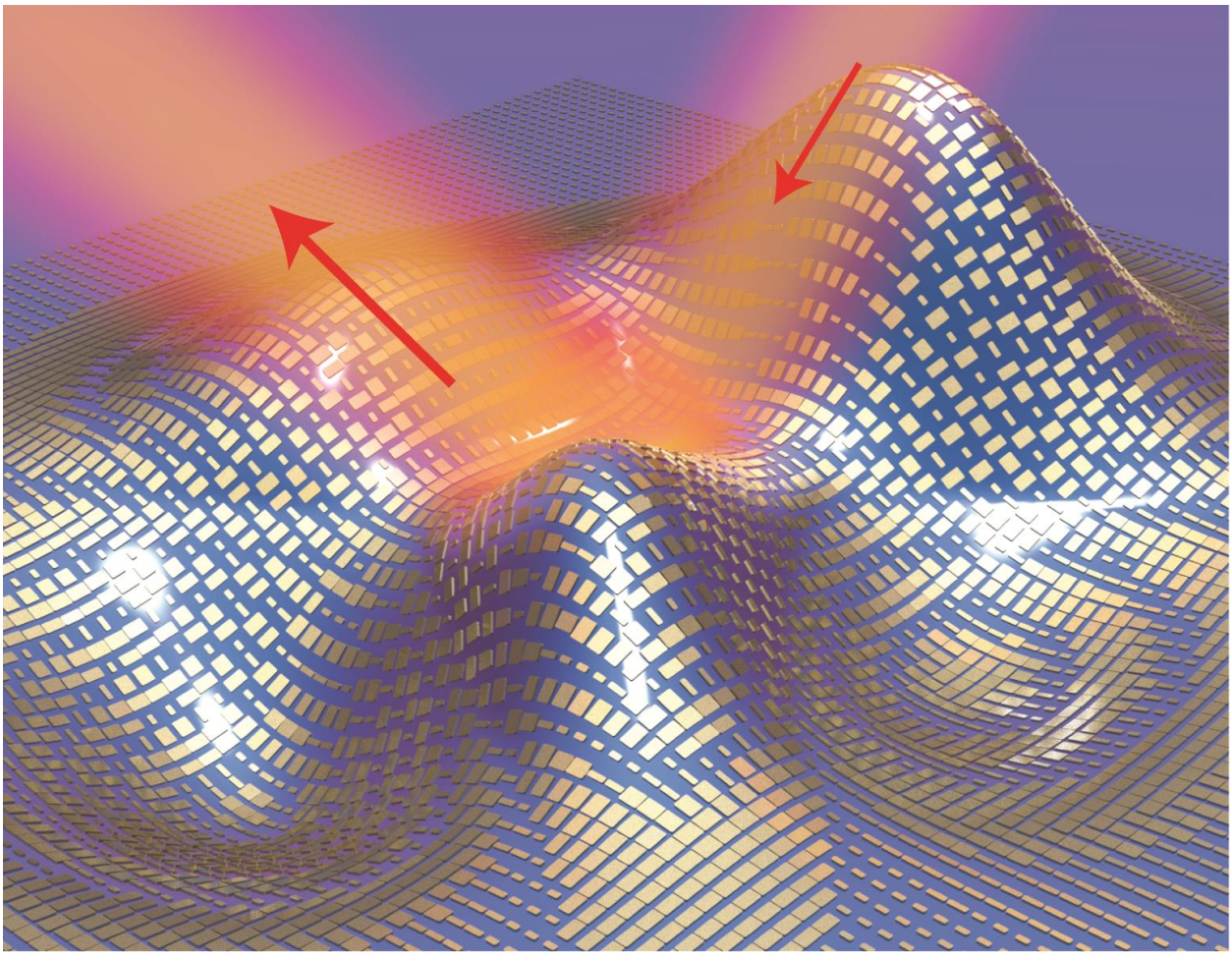

Figure 4.6 A three-dimensional illustration of a metasurface skin cloak. The skin cloak is an ultra-thin layer of nanoantennas conformally covering the arbitrarily-shaped object. The small golden blocks are the nanoantennas forming the cloak.

The fabrication of the three-dimensional object and skin cloak requires precise nanofabrication steps. The procedure (Fig. 4.7) begins with a 1 μm thick oxidation on a silicon substrate. A Gallium-based focused ion beam (FIB) is then used to carve the three-dimensional profile and pattern the alignment marks. The oxidation layer is to trap and prevent the remnant Gallium ions (implanted during the FIB milling process) from diffusing to the top surface and cause undesired roughness. This is followed by electron beam evaporation of a thick 200 nm of gold to form the bottom reflective layer. Next, we utilize an atomic force microscopy (AFM) to scan the height profile of the entire three-dimensional contour, as shown in Fig. 4.8a. Using the height data as the input, this allows us to design and fabricate the corresponding metasurface nanoantennas at each local position. An extra step of coordinate marking of the patterned alignment marks is also performed to further improve the alignment accuracy. We can then do electron beam evaporation of 50 nm MgF_2 to create the dielectric layer for gap plasmon resonance. Importantly, the

metasurface nanoantennas are patterned on a bilayer PMMA A2 resist using electron beam lithography (EBL) with extremely precise alignment. Upon development, 2 nm of Chromium (as adhesion layer) and 30 nm of gold are evaporated followed by the lift-off process. Fig. 4.8b and Fig. 4.8c show the scanning electron microscope (SEM) images of the fabricated metasurface conformally positioned on the three-dimensional object.

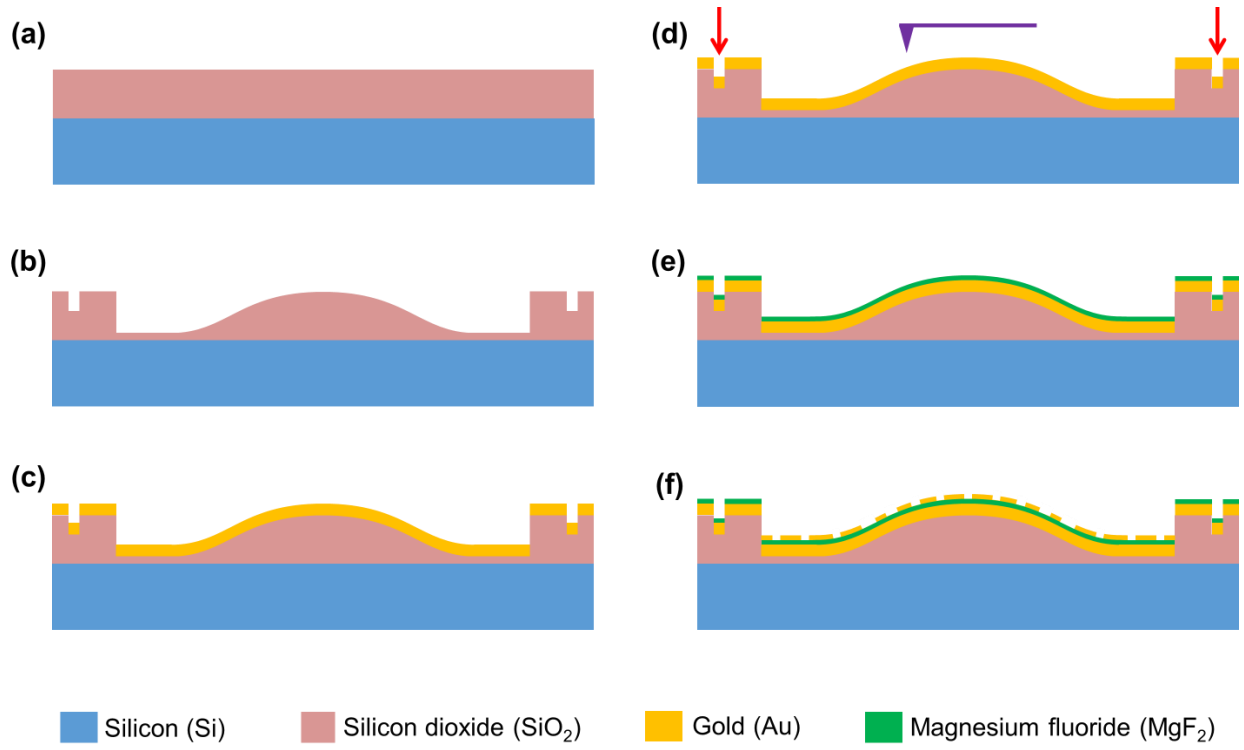

Figure 4.7 Schematic of the fabrication process. (a) 1 μm thick SiO_2 deposited on the Si substrate. (b) FIB milling of the 3D profile and the alignment marks. (c) Electron beam evaporation of a 200 nm thick Au layer. (d) AFM scanning and coordinate marking of the alignment marks. (e) Electron beam evaporation of a 50 nm MgF_2 layer. (f) EBL patterning of the metasurface nanostructures.

To test the cloaking performance, we first collect the wide-field reflection image of the device. We use a low numerical aperture (NA) objective lens in a standard microscope setup to acquire the image for its wider field of view and the closer resemblance to a plane wave incidence. To simplify the measurement, the metasurface nanoantennas are designed for a particular linear polarization, thus by rotating the polarization of the incident light we can easily switch the cloak between on and off states. Testing at each separate wavelength requires a tunable laser source, and a diffuser is added along the path to reduce the speckles caused by the interference of the input laser beam. In addition, a Mach-Zehnder interferometer setup (Fig. 4.9) is also built to acquire the phase information of the reflected light. A temperature tunable diode laser is used as the light source. The incident light is split into two paths when reaches the first beam splitter. One enters an objective and interacts with the sample. The other one act as the reference light to form the interference pattern. The optical path of the reference arm is adjustable using a retroreflector mounted on a translation stage. The two paths rejoin at the second beam splitter and form the interference fringes at a charge-coupled device (CCD).

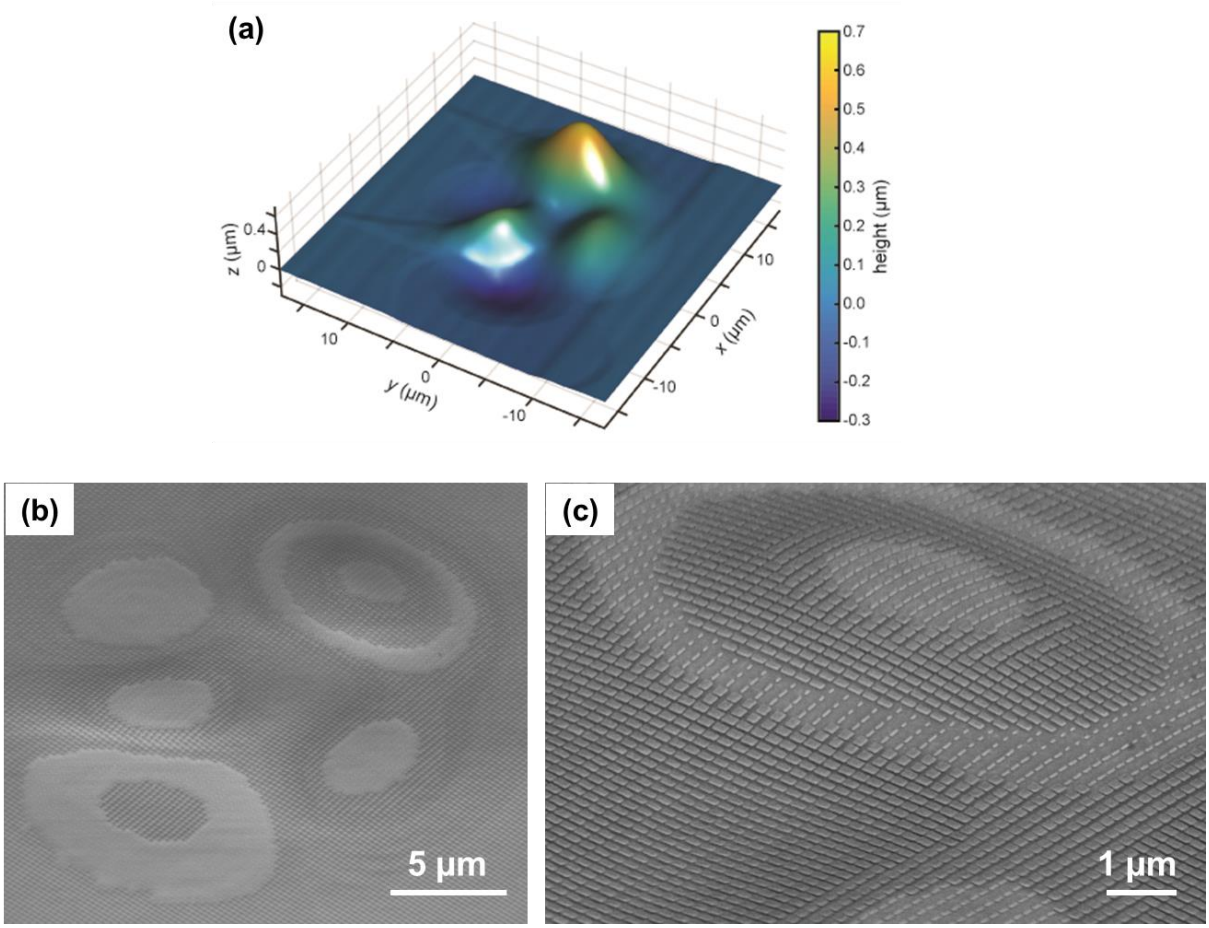

Figure 4.8 A metasurface invisibility skin cloak for a three-dimensional arbitrarily-shaped object. (a) The AFM height profile of a three-dimensional arbitrarily-shaped object that includes multiple bumps and dents. (b) SEM images of the zoomed-out image of the entire object. (c) Close-up view of the metasurface skin cloak conformally fabricated on top of the three-dimensional object.

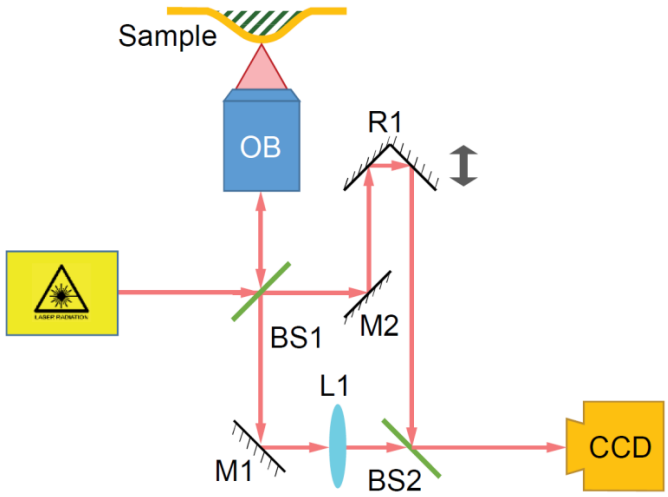

Figure 4.9 Mach-Zehnder interferometer setup for the phase measurement. (BS – beam splitter, M – mirror, R – retroreflector, L – lens, OB – objective, CCD - charge-coupled device)

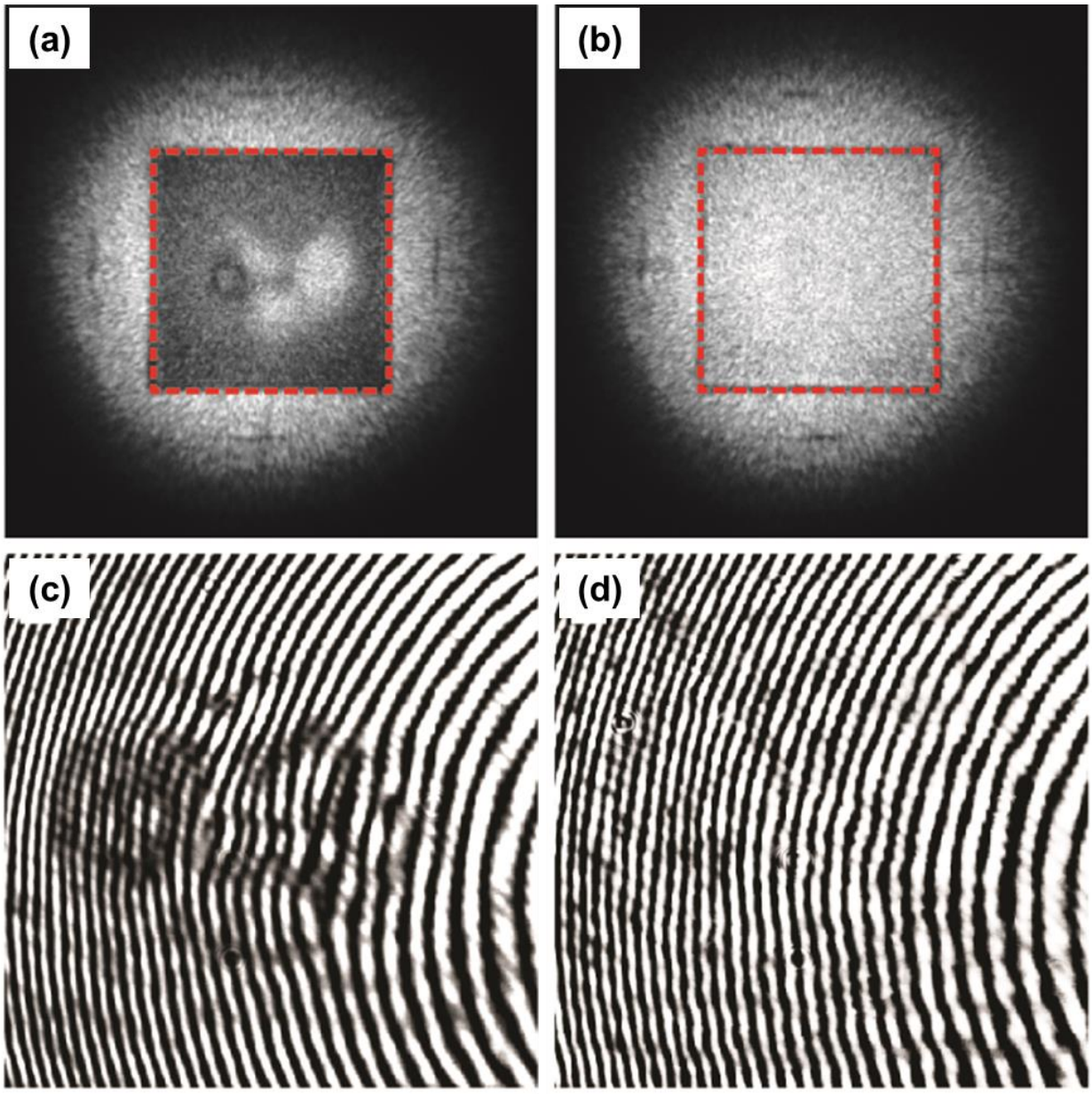

Figure 4.10 (a) and (b) Optical wide-field reflection image obtained with a 0.3 numerical aperture objective lens with 730-nm-wavelength laser illumination. The sample region is indicated by the red dashed boxes. (a) The obtained reflection image when the cloak is off and (b) when the cloak is on, taken at the same position. The on/off switching of the cloak is carried out by changing the polarization of the incident light since the cloak is intentionally designed to work in one linear polarization. We can see that with the cloak off, the bumps and dents are observable under the microscope, while they are totally invisible with the cloak on. Note that the noise in the images is due to the laser speckles. (c) and (d) The interference images when the cloak is off (c) and when it is on (d). When the cloak is off, the interference fringes are distorted on the three-dimensional object, which indicates the height difference on the surface. When the cloak is on, the interference fringes smoothen again, matching with that of the flat surface outside the object region, thus proving that both the wavefront and the phase are well restored without any distortion.

The measurement results of both the reflection and phase are shown in Fig. 4.10. Since we design our nanoantennas to have the correct phase shift only in the x-polarization, we can easily turn the cloak on and off by switching the polarization. When the cloak is off, a strong contrast between the cloaked region and the surrounding reflective surface reveals the object (Fig. 4.10a); but when the cloak is turned on, the contrast becomes indistinguishable, rendering the object completely invisible (Fig. 4.10b). For the phase measurement, when the cloak is off, there are distortions in the interference fringes indicating the phase of the reflected light is non-uniform due to the scattering of the object (Fig. 4.10c). When the cloak is on, the distortions disappear and the fringes are smoothly aligned indicating the reflected phase is perfectly uniform over the surface (Fig. 4.10d). As we are using an objective to image the sample, the interference fringes are rings rather than perfectly straight lines. We also test an object with identical profile but without a skin cloak. The interference results (Fig. 4.11) show fringe distortions similar to when the cloak is turned off, thereby verifying that the distortion of fringes is purely due to the object scattering and not because of the metasurface's polarization dependency.

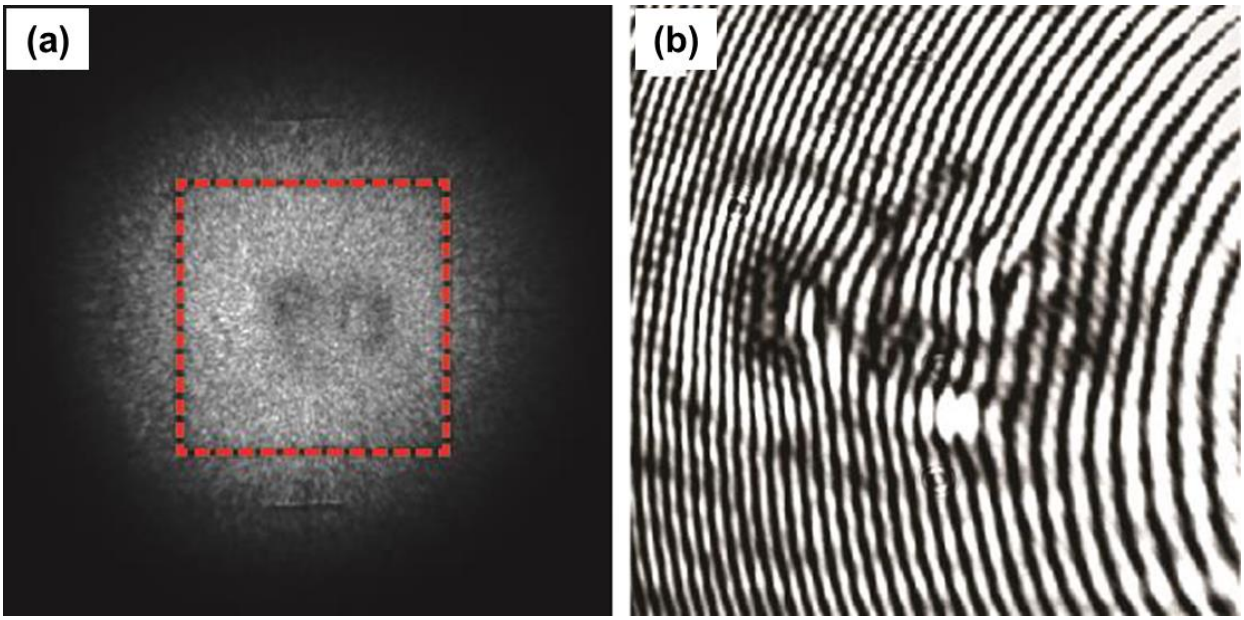

Figure 4.11 Experimental measurement results for a control sample of same three-dimensional height profile but without the metasurface cloak. (a) A wide-field reflection image where the bumps are clearly visible. The red dashed box indicates the sample region. (b) An interference pattern showing the phase information of the reflected light. We can see that the fringes are distorted in the region of the object. Note that the pattern looks similar as that obtained when the metasurface skin cloak is ineffective (Fig. 4.10c). This control sample is fabricated on the same chip.

To quantify the performance of a skin cloak, we fabricated and measured a three-dimensional bump-shaped object (Fig. 4.12). When the cloak is off (Fig. 4.13c), the interference fringes are shifted in the direction perpendicular to the stripes. The amount of phase shift is approximately proportional to the local height of the bump surface. When the cloak is on (Fig. 4.13d), the interference fringes become smooth and realign with those from the flat region. Importantly, no phase jump is observed even at the edges of the skin cloak, proving that there is no additional phase introduced by the cloak. The relative height information is extracted from the amount of fringe dislocation. It is compared with the AFM height profile measured before the nanoantennas

are fabricated (Fig. 4.14). When the skin cloak is off, the height from the interference measurement matches well with the AFM results, revealing the true bump profile. Thus, the bump can be precisely mapped out using this phase-sensitive method. When the cloak is on, the extracted height remarkably drops to zero over the entire area and appears invisible.

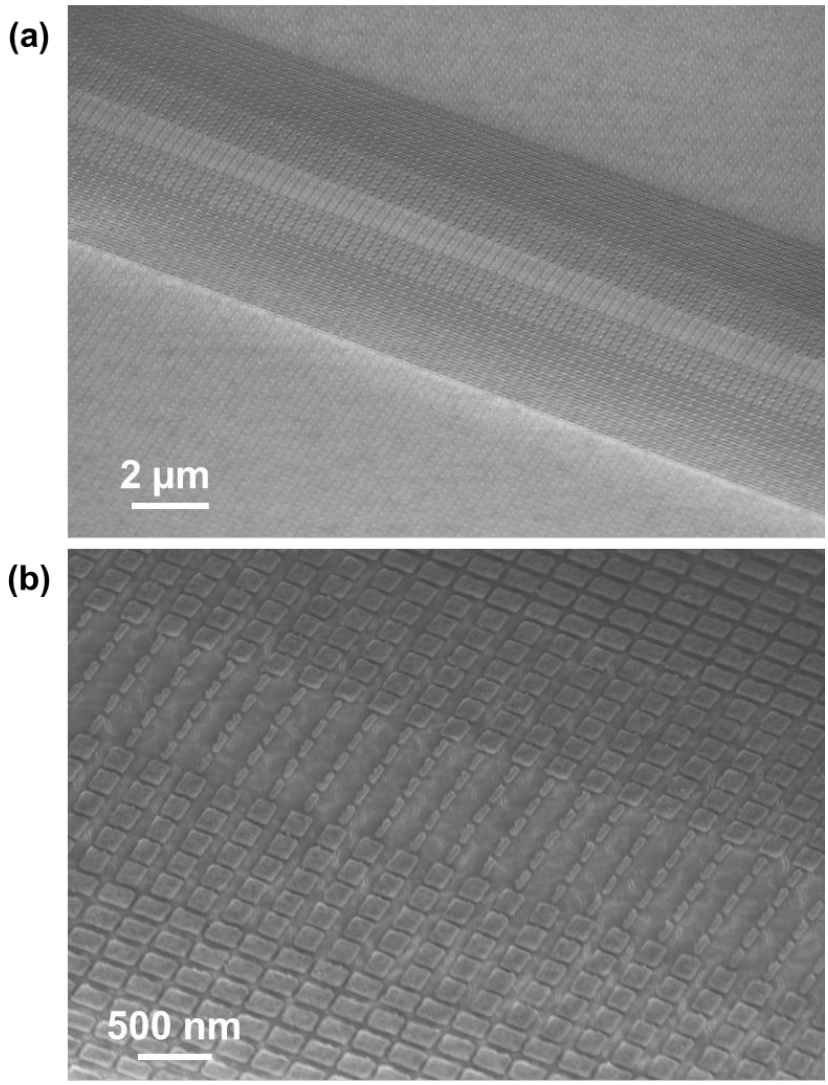

Figure 4.12 (a) SEM image of a fabricated three-dimensional bump-shaped object with the metasurface skin cloak wrapped over it. (b) Close-up view of the metasurface nanoantennas.

Our skin cloak fully inherits the advantages from the metasurfaces. It is extremely thin, with an antenna and dielectric spacer thickness of 30 nm and 50 nm, respectively. The total thickness is almost a tenth of the operating wavelengths. Our skin cloak is conformal and fully scalable to macroscopic sizes. The cloak can also work on objects with sharp features like abrupt edges and peaks because the invisibility is attained via the local phase adjustments. Within our experiments, our design can tolerate incident angles at least within 30 degrees. We also found that the metasurface skin cloak can work over a range of wavelengths, as the arbitrarily-shaped object can be concealed relatively well from 710 nm to 810 nm (Fig. 4.15). To allow easy switching between cloak on and cloak off configurations for direct comparison, the metasurface is designed

to work only in one polarization. However, by making the nanoantenna shapes symmetric in both x- and y- directions it is possible to have a polarization independent invisibility skin cloak. Furthermore, if the nanoantennas can be made adaptive, passively or actively, a deformable skin cloak can potentially conceal any object.

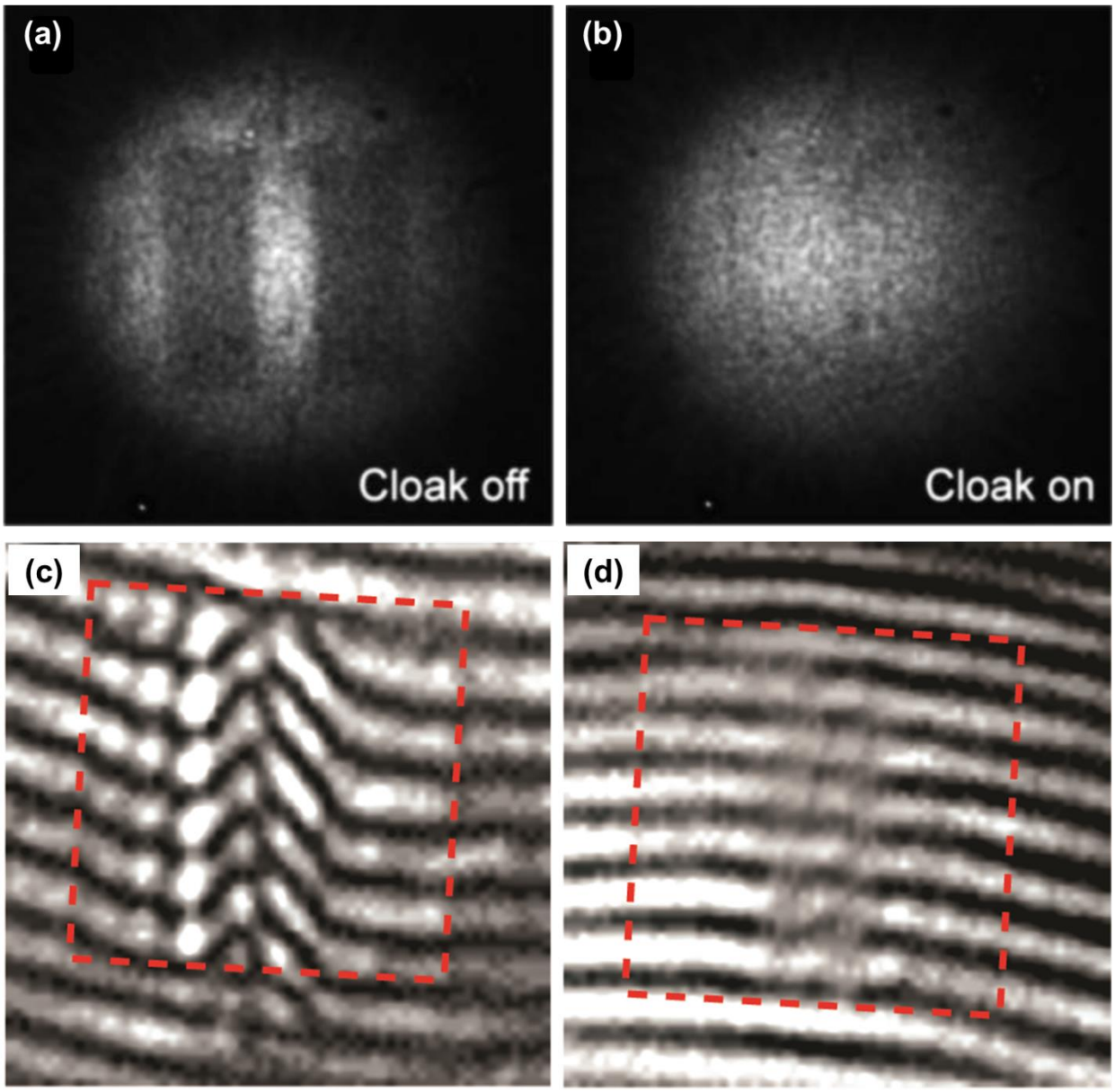

Figure 4.13 Quantitative performance evaluation for a metasurface skin cloak on a three-dimensional bump-shaped object. The bump has a maximum height of around 400 nm and a width of approximately 10 μm. (a) and (b) Wide-field reflection image when the cloak is off (a) and when the cloak is on (b). (c) and (d) Interference fringes obtained when the cloak is off (c) and when the cloak is on (d). The sample regions are indicated by the red dashed boxes.

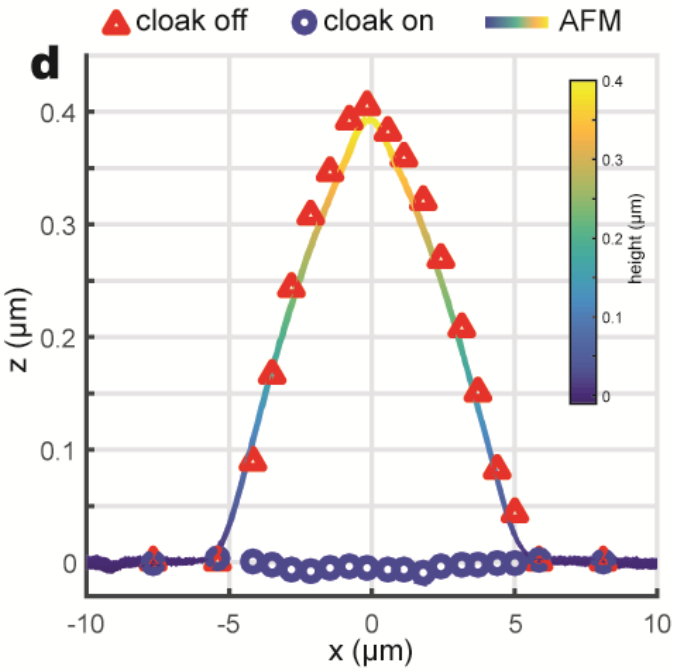

Figure 4.14 The extracted height profile from the interference measurement together with that from the atomic force microscope (AFM) measurement. The solid line represents the AFM results measured before the fabrication of the nanoantennas. The red triangles show the height information extracted from the interference pattern with the cloak off. The data match well with the AFM results. The blue circles denote the height information extracted from the interference pattern with the cloak on. The height becomes almost zero all over the bump region, making the object appears hidden as if it is just a perfectly reflecting mirror.

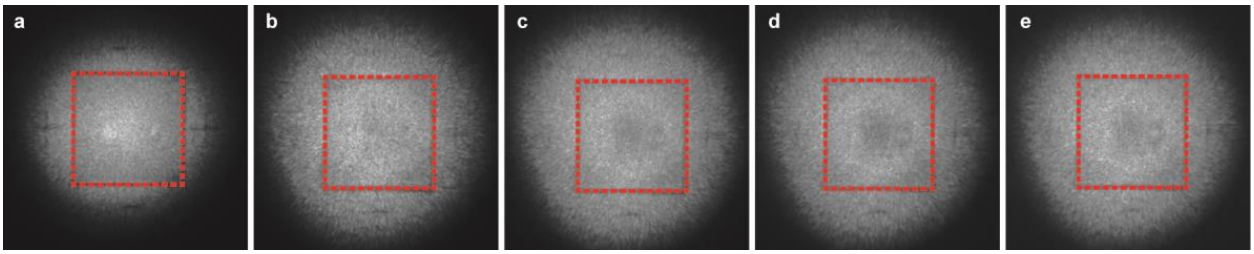

Figure 4.15 Widefield reflection images for the metasurface skin mask at different wavelengths. (a) 710 nm, (b) 750 nm, (c) 770 nm, (d) 790 nm, (e) 810 nm. We can see that the skin cloak works moderately well in this wavelength range. The sample region is indicated by the red dashed boxes.

4.3 Summary and Outlook

In chapter 4, we present an ultra-thin invisibility skin cloak in the visible wavelength range using the concept of subwavelength reflection phase manipulation enabled by metasurface. To the best of our knowledge, this is the first conformal invisibility cloak for three-dimensional arbitrarily-shaped objects, with complete restoration of both the wavefront and the phase of the reflected light. As the metasurface is extremely thin, lightweight, and easy to fabricate, this new approach

is a promising way for making large-scale ultra-thin invisibility devices to conceal macroscopic objects for real-world applications.

Subwavelength phase control essentially provides a new degree of freedom to engineer the effective electromagnetic response. Unlike standard optical metamaterials which are periodic in the planar dimension, metasurface completely breaks the symmetry and allows spatial phase modulation of arbitrary form, limited only by imagination. It is therefore not hard to imagine using metasurface as antenna to control the far field radiation and couple it with emitters to enhance the light matter interaction. Owing to its two-dimensional ultra-thin nature, I believe metasurface also has a huge potentials in engineering the surface nonlinearity and be integrated into the emerging field of flexible optoelectronics.

References

[1] N. Yu, P. Genevet, M. A. Kats, F. Aieta, J.-P. Tetienne, F. Capasso, and Z. Gaburro, "Light propagation with phase discontinuities: Generalized laws of reflection and refraction," *Science* **334**, 333 (2011).

[2] X. Ni, N. K. Emani, A. V. Kildishev, A. Boltasseva, and V. M. Shalaev, "Broadband light bending with plasmonic nanoantennas," *Science* **335**, 427 (2012).

[3] S. Sun, Q. He, S. Xiao, Q. Xu, X. Li, and L. Zhou, "Gradient-index meta-surfaces as a bridge linking propagating waves and surface waves," *Nature Materials* **11**, 426 (2012).

[4] X. Ni, S. Ishii, A. V. Kildishev, and V. M. Shalaev, "Ultra-thin, planar, Babinet-inverted plasmonic metalenses," *Light: Science and Applications* **2**, e72 (2013).

[5] L. Huang, X. Chen, B. Bai, Q. Tan, G. Jin, T. Zentgraf, and Shuang Zhang, "Helicity dependent directional surface plasmon polariton excitation using a metasurface with interfacial phase discontinuity," *Light: Science and Applications* **2**, e70 (2013).

[6] N. Shitrit, I. Yulevich, E. Maguid, D. Ozeri, D. Veksler, V. Kleiner, and E. Hasman, "Spin-optical metamaterial route to spin-controlled photonics," *Science* **340**, 724 (2013).

[7] X. Yin, Z. Ye, J. Rho, Y. Wang, and X. Zhang, "Photonic spin Hall effect at metasurfaces," *Science* **339**, 1405 (2013).

[8] A. V. Kildishev, A. Boltasseva, and V. M. Shalaev, "Planar photonics with metasurfaces," *Science* **339**, 1232009 (2013).

[9] N. Yu and F. Capasso, "Flat optics with designer metasurfaces," *Nature Materials* **13**, 139 (2014).

[10] S. Sun, Q. He, S. Xiao, Q. Xu, X. Lin, and L. Zhou, "Gradient-index meta-surfaces as a bridge linking propagating waves and surface waves," *Nature Materials* **11**, 426 (2012).

[11] J. Lin, J. P. B. Mueller, Q. Wang, G. Yuan, N. Antoniou, X.-C. Yuan, and F. Capasso, "Polarization-controlled tunable directional coupling of surface plasmon polaritons," *Science* **340**, 331 (2013).

[12] D. Lin, P. Fan, E. Hasman, and M. L. Brongersma, "Dielectric gradient metasurface optical elements," *Science* **345**, 298 (2014).

[13] F. Aieta, P. Genevet, M. A. Kats, N. Yu, R. Blanchard, Z. Gaburro, and F. Capasso, "Aberration-free ultrathin flat lenses and axicons at telecom wavelengths based on plasmonic metasurfaces," *Nano Letters* **12**, 4932 (2012).

[14] N. Yu, F. Aieta, P. Genevet, M. A. Kats, Z. Gaburro, and F. Capasso, "A broadband, background-free quarter-wave plate based on plasmonic metasurfaces," *Nano Letters* **12**, 6328 (2012).
[15] A. Pors, M. G. Nielsen, and S. I. Bozhevolnyi, "Broadband plasmonic half-wave plates in reflection," *Optics Letters* **38**, 513 (2013).
[16] L. Huang, X. Chen, H. Mühlenbernd, H. Zhang, S. Chen, B. Bai, Q. Tan, G. Jin, K.-W. Cheah, C.-W. Qiu, J. Li, T. Zentgraf, and S. Zhang, "Three-dimensional optical holography using a plasmonic metasurface," *Nature Communications* **4**, 3808 (2013).
[17] X. Ni, A. V. Kildishev, and V. M. Shalaev, "Metasurface holograms for visible light," *Nature Communications* **4**, 2807 (2013).
[18] G. X. Zheng, H. M ühlenbernd, M. Kenney, G. Li, T. Zentgraf, and S. Zhang, "Metasurface holograms reaching 80% efficiency," *Nature Nanotechnology* **10**, 308 (2015).
[19] J. Lee, M. Tymchenko, C. Argyropoulos, P.-Y. Chen, F. Lu, F. Demmerle, G. Boehm, M.-C. Amann, A. Alù, and M. A. Belkin, "Giant nonlinear response from plasmonic metasurfaces coupled to intersubband transitions," *Nature* **511**, 65 (2014).
[20] J. B. Pendry, D. Schurig, and D. R. Smith, "Controlling electromagnetic fields," *Science* **312**, 1780 (2006).
[21] D. Schurig, J. J. Mock, B. J. Justice, S. A. Cummer, J. B. Pendry, A. F. Starr, and D. R. Smith, "Metamaterial electromagnetic cloak at microwave frequencies," *Science* **314**, 977 (2006).
[22] W. S. Cai, U. K. Chettiar, A. V. Kildishev, and V. M. Shalaev, "Optical cloaking with metamaterials," *Nature Photonics* **1**, 224 (2007).
[23] A. Alu, "Mantle cloak: Invisibility induced by a surface," *Physical Review B* **80**, 245115 (2009).
[24] P. Y. Fan, U. K. Chettiar, L. Cao, F. Afshinmanesh, N. Engheta, and M. L. Brongersma, "An invisible metal-semiconductor photodetector," *Nature Photonics* **6**, 380 (2012).
[25] M. Selvanayagam, and G. V. Eleftheriades, "Experimental Demonstration of Active Electromagnetic Cloaking," *Physical Review X* **3**, 041011 (2013).
[26] L. Sanchis, V. M. García-Chocano, R. Llopis-Pontiveros, A. Climente, J. Martínez-Pastor, F. Cervera, and J. Sánchez-Dehesa, "Three-dimensional axisymmetric cloak based on the cancellation of acoustic scattering from a sphere," *Physical Review Letters* **110**, 124301 (2013).
[27] T. C. Han, X. Bai, D. Gao, J. T. L. Thong, B. Li, and C.-W. Qiu, "Experimental demonstration of a bilayer thermal cloak," *Physical Review Letters* **112**, 054302 (2014).
[28] H. Y. Xu, X. H. Shi, F. Gao, H. D. Sun, and B. L. Zhang, "Ultrathin three-dimensional thermal cloak," *Physical Review Letters* **112**, 054301 (2014).
[29] R. Schittny, M. Kadic, S. Guenneau, and M. Wegener, "Experiments on transformation thermodynamics: Molding the flow of heat," *Physical Review Letters* **110**, 195901 (2013).
[30] G. W. Milton, M. Briane, and J. R. Willis, "On cloaking for elasticity and physical equations with a transformation invariant form," *New Journal of Physics* **8**, 248 (2006).
[31] M. Farhat, S. Guenneau, and S. Enoch, "Ultrabroadband Elastic Cloaking in Thin Plates," *Physical Review Letters* **103**, 024301 (2009).
[32] M. Brun, S. Guenneau, and A. B. Movchan, "Achieving control of in-plane elastic waves," *Applied Physics Letters* **94**, 061903 (2009).
[33] S. Zhang, D. A. Genov, C. Sun, and X. Zhang, "Cloaking of matter waves," *Physical Review Letters* **100**, 123002 (2008).

[34] R. Fleury, and A. Alu, "Quantum cloaking based on scattering cancellation," *Physical Review B* **87**, 045423 (2013).
[35] J. S. Li, and J. B. Pendry, "Hiding under the carpet: A new strategy for cloaking," *Physical Review Letters* **101**, 203901 (2008).
[36] R. Liu, C. Ji, J. J. Mock, J. Y. Chin, T. J. Cui, and D. R. Smith, "Broadband ground-plane cloak," *Science* **323**, 5912 (2009).
[37] H. F. Ma and T. J. Cui, "Three-dimensional broadband ground-plane cloak made of metamaterials," *Nature Communications* **1**, 21 (2010).
[38] J. Valentine, J. S. Li, T. Zentgraf, G. Bartal, and X. Zhang, "An optical cloak made of dielectrics," *Nature Materials* **8**, 568 (2009).
[39] L. H. Gabrielli, J. Cardenas, C. B. Poitras, and M. Lipson, "Silicon nanostructure cloak operating at optical frequencies," *Nature Photonics* **3**, 461 (2009).
[40] T. Ergin, N. Stenger, P. Brenner, J. B. Pendry, and M. Wegener, "Three-Dimensional Invisibility Cloak at Optical Wavelengths," *Science* **328**, 337 (2010).
[41] J. Fischer, T. Ergin, and M. Wegener, "Three-dimensional polarization-independent visible-frequency carpet invisibility cloak," *Optics Letters* **36**, 2059 (2011).
[42] M. Gharghi, C. Gladden, T. Zentgraf, Y. Liu, X. Yin, J. Valentine, and X. Zhang, "A carpet cloak for visible light," *Nano Letters* **11**, 2825 (2011).
[43] X. Chen, Y. Luo, J. Zhang, K. Jiang, J. B. Pendry, and S. Zhang, "Macroscopic invisibility cloaking of visible light," *Nature Communications* **2**, 176 (2011).
[44] B. Zhang, Y. Luo, X. Liu, and G. Barbastathis, "Macroscopic invisibility cloak for visible light," *Physical Review Letters* **106**, 033901 (2011).
[45] B. Orazbayev, N. Mohammadi Estakhri, M. Beruete, A. Alù, "Terahertz carpet cloak based on a ring resonator metasurface," *Physical Review B* **91**, 195444 (2015).
[46] A. Pors, O. Albrektsen, I. P. Radko, S. I. Bozhevolnyi, "Gap plasmon-based metasurfaces for total control of reflected light," *Scientific Reports* **3**, 2155 (2013).
[47] S. Sun, K.-Y. Yang, C.-M. Wang, T.-K. Juan, W. T, Chen, C. Y. Liao, Q. He, S. Xiao, W.-T. Kung, G.-Y. Guo, L. Zhou, and D. P. Tsai, "High-Efficiency Broadband Anomalous Reflection by Gradient Meta-Surfaces," *Nano Letters* **12**, 6223 (2012).

Chapter 5

Conclusion and Outlook

For centuries, the design of standard optical elements is mostly limited to the engineering of the real part of refractive index above one. However, this boundary can be broken using artificially-engineered optical metamaterials. In this dissertation, I show that engineering of the real part and imaginary part of the refractive index, as well as the local subwavelength phase control can all lead to unique functionalities and extreme device performances.

Chapter 2 first shows how resonances can be engineered using multilayer stacked metal-dielectric nanostructures to attain bulk (real part of) refractive index from positive to negative values. Not only that a bulk NIM is experimentally demonstrated in the visible wavelength range, it has a relatively high transmission, making it one step closer to practical applications. This low-loss property is extremely crucial in single-photon quantum optics experiment and nonlinear optics study which typically involve rather weak signals. Here we investigated nonlinear propagation through a thick bulk NIM and ZIM for the very first time. More importantly, we proved that ZIM guarantees constructive interference and perfect phase-matching within the bulk medium, resulting in equal amount of nonlinear light generation in both the forward and backward directions. We believe the demonstrated negative phase advance of visible NIMs and the uniform phase distribution in ZIMs can open the door for new optical devices in both the linear and nonlinear optics regimes. As metamaterials are typically anisotropic, we can further engineer the components of the permittivity and permeability tensors to attain unique isofrequency contours in the Fourier space. Through rigorous measurement of the transmission and reflection, both amplitude and phase for a range of wavevectors, a novel magnetic hyperbolic dispersion bulk optical metamaterial is demonstrated, enabling a new path to enhance photon density of states and light-matter interaction.

Chapter 3 highlights the possibility of engineering the imaginary part of refractive index to realize novel optical devices. In particular, the interplay between loss and gain is carefully engineered to be parity-time (PT) symmetric for unique resonance mode control. We showed that by creating the loss and gain mediums in a ring configuration, thresholdless PT broken phase can be attained. Such a system will always have a paired resonant gain and loss modes. For a PT microring resonator with whispering-gallery-modes (WGMs), only the gain mode will survive and lase while the rest will be absorbed by the loss, thereby achieving single-mode lasing regardless of the material gain bandwidth. This allows the creation of single-mode lasers with precise cavity mode and radiation control. In addition, PT symmetry enables laser and anti-laser (CPA) to be built within a single device. We experimentally showed direct switching between the lasing and anti-lasing states by simply tuning the phase of the probe beams. This new modulation strategy gives rise to strong coherent amplification/absorption to the signals and potentially approaches the ultimate limit in terms of modulation depth.

Chapter 4 details a new dimension of subwavelength phase engineering to control the electromagnetic response. Spatially varying subwavelength nanoantennas, or so-called metasurface, is used to compensate the local phase at each point, making a curved surface appears flat. Importantly, this new approach of metasurface cloaking can obscure the scattering

(both wavefront and phase) from the object, rendering it undetectable even with a phase-sensitive instrument. An ultra-thin, conformal invisibility skin cloak that can cloak three-dimensional object of arbitrary shape is experimentally demonstrated. Owing to the two-dimensional nature of metasurface, it can be easily scaled up to hide even macroscopic objects. We believe this subwavelength phase engineering approach will lead to a new family of unique optical devices with extreme light bending and phase control capabilities.

While this dissertation establishes three new paths for controlling the light propagation and extending the boundaries of optical metamaterials, I believe the next phase of breakthrough will rely heavily on the materials development, novel physics discovery, and application-driven research.

The inherent Joule loss of plasmonic metals remains a huge roadblock in optical metamaterials research. Plenty of opportunities have thus arisen to replace the metals with transparent conductive oxides and other low-loss doped semiconductors. In addition, these materials are also more robust against the high temperature, making them more practical for many applications. Incorporation of a gain medium close to the metamaterial structure is certainly another useful approach to combat the loss. Therefore I expect to see more efforts in realizing subwavelength hybrid metal-semiconductor gain nanostructures for full loss compensation while preserving the extreme optical properties enabled by the metamaterials. An alternative route is to rely on high index dielectrics with a strong Mie resonance to tailor the electromagnetic response. The most beautiful synergy is when dielectric Mie structures also self-possess optical gain to achieve truly zero loss optical metamaterials. In recent years, the discovery of 2D transition metal dichalcogenide (TMDC) with direct bandgap has ignited a new wave of optoelectronic research owing to the enhanced emission quantum yield of the monolayer. Therefore multilayer stacking of plasmonic nanostructures with similar/different layers of 2D TMDC materials can in future allow the emitters to be fully embedded inside the metamaterials environment and enhance the light matter interaction to a whole new level.

The field of metamaterials initially began with the discovery of negative index physics and the invention of superlens. I believe novel physics will continue to drive the metamaterial research breakthrough. For instance, topological photonics relying on the interface state propagation is giving new hopes to build practical optical devices, as they are less sensitive to defects and fabrication imperfection. Spin and valley degrees of freedom, if combine with metamaterials, can lead to efficient control of the emission profile and helicity. Similarly, many solid state electronic and transport properties can be directly coupled to optical waves using metamaterial elements as the connecting bridge. Engineering the symmetry and coupling between different meta-atoms is another important route to significantly augment the performance of current optical metamaterials.

After more than a decade of research in optical metamaterials, it's time to aim for functional devices that can outperform standard optical products. The enormous market demand for efficient antennas and emitters will be a key driver for continuous optimization of the optical metamaterial design to further enhance the light matter interaction. The ability to engineer high Purcell factor optical metamaterials can actually shorten the photon decay time, thus paving the way for extremely fast emitters and modulators. I also see metasurface as a promising candidate to compete for the market of flexible electronics for its ultra-thin two-dimensional feature. At the

more exotic front, a fully transmitting three-dimensional visible cloak is still very much desired, and optical metamaterials remain the only viable solution to this centuries-old mystery. Therefore, the field of optical metamaterials will continue to thrive for the many more years to come!